ANALYSIS OF FLEXIBLE FIBER SUSPENSIONS USING THE LATTICE BOLTZMANN METHOD

A Dissertation
Presented to
The Academic Faculty

by

Sheila Rezak

In Partial Fulfillment
of the Requirements for the Degree
Doctor of Philosophy in the
School of Mechanical Engineering

Georgia Institute of Technology
August 2008

ANALYSIS OF FLEXIBLE FIBER SUSPENSIONS USING THE LATTICE BOLTZMANN METHOD

Approved by:

Dr. Cyrus Aidun, Co-Advisor
School of Mechanical Engineering
Georgia Institute of Technology

Dr. Mostafa Ghiaasiaan, Co-Advisor
School of Mechanical Engineering
Georgia Institute of Technology

Dr. Yulin Deng
School of Chemical and Biomolecular Engineering
Georgia Institute of Technology

Dr. Jeff Empie
School of Chemical and Biomolecular Engineering
Georgia Institute of Technology

Dr. Tim Patterson
Mechanical Engineering
Georgia Institute of Technology

Date Approved: 07/02/08

To my family,

Mama, Papa, Edison and Elijah

ACKNOWLEDGEMENTS

I would like to express my sincere thanks and gratitude to my advisor, Dr. Cyrus Aidun, for his support and guidance during my time at Georgia Tech. I have learned a lot from him regarding the fundamental ideas of this project. I wish to thank Dr. Mostafa Ghiaasiaan, Dr. Tim Patterson, Dr. Jeff Empie and Dr. Yulin Deng for their constant encouragement and guidance during my thesis work. I wish to thank Dr. Ejiang Ding for helping me learn and improve the programming language that is used on this project. I wish to thank my fellow colleagues, Jonathan Clausen and Robert MacMeccan for their magnificent ideas on the programming development presented in this project.

Finally, I could not have accomplished this without the support of my family: husband Edison Manurung, son Elijah Maximus Manurung, parents Mohamad Rezak and Erly Erawati, sibling Zoya Rezak. Your encouragement has been the backbone of all my accomplishments. Thank you Lord Jesus.

TABLE OF CONTENTS

LIST OF TABLES

Page

LIST OF FIGURES

Page

LIST OF SYMBOLS AND ABBREVIATIONS

Letter Symbols

A_σ	Equilibrium distribution coefficient
A_r	Aspect ratio
A_{reff}	Effective aspect ratio
α_0	Dimensionless factor for suspension viscosity
$\mathbf{B}$	Displacement matrix
$\mathbf{B}^T$	Transpose displacement matrix
B_σ	Equilibrium distribution coefficient
b	Ellipse major axis
β	Newmark constant
BEM	Boundary element method
C	Orbital consant
$\mathbf{C}$	Damping matrices
C_σ	Equilibrium distribution coefficient
c	Ellipse minor axis
CyrR	Radius cylinder of domain simulation
$\mathbf{D}$	Elasticity matrix
D_r	Link direction in raytracing method
d	Diameter particle
D_σ	Equilibrium distribution coefficient
det	Determinant

dp/dx	Pressure gradient
d/dt	Material time derivative
E	Young's modulus number
$\mathbf{e_j}$	Eigen vectors (e_x, e_y, e_z)
$\mathbf{e_{\sigma i}}$	Velocity vector
$\mathbf{\lvert e_{\sigma i} \rvert}$	Magnitude of velocity vector
F	External load vector
F'	Newmark external load vector
$\mathbf{F_g}$	Volumetric force
F_I	Inertia force
F_D	Damping force
F_E	Elastic force
$F_{\sigma i}^{(b)}$	Force exerted on a particle for any lattice link σi
F_{cI}	Contact force exerted on segment fiber-I
$f_{\sigma i}$	Distribution function
$f_{\sigma i}^{(0)}$	Equilibrium distribution function
FE	Finite element method
G	Shear rate
G_S	Shear modulus
γ	Newmark constant
H	Displacement interpolation matrix or shape function
$\mathbf{H^T}$	Transpose displacement interpolation matrix
h	Height parameter from domain center to top or bottom domain walls

h_{IJ}	Gap minimum between fiber-I and fiber-J
I	Segments of fiber-I
i	Direction of velocity vectors (four-diagonal or non-diagonal directions)
ii	Number of links
J	Segments of fiber-J
jj	Number of finite element surface nodes
[J]	Jacobian operator
$[J^{-1}]$	Inverse Jacobian operator
K	Stiffness matrices
K	Constant which is relative to aspect ratio of the actual particles
K'	Newmark stiffness matrix
$\mathbf{K^T}$	Transpose stiffness matrix
K_1, K_2	Dimensionless factors for relative viscosity
k	Node velocity
L	Particle length
lx	Simulation domain length
ly	Simulation domain height
lz	Simulation domain width
ℓ	Characteristic length
λ	Fraction of effective aspect ratio to aspect ratio
LB	Lattice Boltzmann method
M	Mass matrices
m	Mass

MD	Molecular dynamics method
N_c	Crowding factor
n	Number density
$\mathbf{n_{IJ}}$	Normal unit vector between particles/fibers segment
O_r	Origin of ray in raytracing method
φ	Angle of a particle on xy plane projection
θ	Polar angle of a particle with the z-axis
ϕ	Volume fraction
Ω	Particle orientation
P	Pressure
ρ	Density
R	Center of mass of a particle
R(t)	Ray in raytracing method
Re	Reynolds number
SLBE	Stokesian lattice Boltzmann method
ζ	Constant of particle contact force
T	Time period
t	Simulation time
t_r	Distance parameter in raytracing method
τ	Relaxation time
σ	Fluid node direction ($\sigma = 0$, correspond to the fluid particles at rest; $\sigma = 1$, correspond to the fluid particles moving to the near-neighbors along axial direction; $\sigma = 2$, correspond to the fluid particles moving to their second-near neighbors along diagonal direction)
σi	Lattice link direction

$\sigma i'$	Lattice link with direction opposite to that of link σi
$\mathbf{T}$	Particle torque
$\mathbf{U}$	Particle speed
$\mathbf{u}$	Local fluid velocity vector (u, v, w)
$\mathbf{u_b}$	Boundary velocity
u_r, v_r	Barycentric coordinate in raytracing method
μ	Dynamic viscosity or suspension viscosity
$[\mu]$	Intrinsic viscosity
μ_r	Relative viscosity
μ_0	Viscosity of suspending medium (pure liquid)
V	Volume
ν	Kinematic viscosity
ν_p	Poisson ratio
∇	Nabla operator (vector differential operator)
$w_{\sigma i}$	Weighing factor for the particle at equilibrium
ω_{MAX}	Maximum frequency in the structural system
X,Y,Z	Cartesian coordinates (global coordinates)
$\overline{X}, \overline{Y}, \overline{Z}$	Cartesian coordinates (local coordinates)
X_{IC}, Y_{IC}, Z_{IC}	Center of mass of arbitrary segment of fiber-I
X_{JC}, Y_{JC}, Z_{JC}	Center of mass of arbitrary segment of fiber-J
$\mathbf{x}$	Displacement vectors
$\dot{\mathbf{x}}$	Velocity vectors
$\ddot{\mathbf{x}}$	Acceleration vectors

y_{itop}	Top domain wall position (y direction)
$y_{ibottom}$	Bottom domain wall position (y directon)

SUMMARY

The characteristics of fibers suspensions depend on the properties of fibers, the suspending fluid, and fiber-fiber interactions. This thesis demonstrates the development and application of a novel coupled method (lattice Boltzmann and finite element methods) to investigate these relationships. Fibers are modeled as flexible rod particles which are simulated by the finite element method. The fluid flow that causes the fibers to deform is calculated by the lattice Boltzmann method. The method is extended from the two dimensional case to the three dimensional case.

Results from simulation show the rigid fiber in simple shear flow produces a good agreement for orientation of a fiber relative to the theoretical study by Jeffery (1922). The flexible fiber exhibits an increase on the rotational period from the rigid fiber due to more deformation shape is revealed during rotation.

The simulation technique demonstrates the ability to simulate fiber-fiber interactions to further study of relative viscosity of suspensions in shear flow. Simulation results show that fiber orientation and relative viscosity depend on the fiber characteristics (fiber aspect ratio, fiber flexibility, and volume fraction). The results are verified against known experimental measurements and theoretical results.

The broad aim of this research is to better understand the behavior of fibers in fluid flow. It is hoped that future researchers may benefit from the new technique and algorithms developed here.

CHAPTER 1

INTRODUCTION

Fiber suspensions are an important part of many different industrial processes, e.g., the papermaking process and manufacturing fiber-reinforced composites. The key parameters of concentration, fiber aspect ratio, and fiber flexibility are used to classify fiber suspensions. In addition, fiber orientation affects the rheological characteristics of the suspensions.

In papermaking, the fibers are slender particles that vary in length, width, and cell wall thickness, and these properties differ widely within and between wood species. Hardwood fibers are shorter than softwood, make lower strength pulps, and usually exhibit a narrower distribution for their important dimensions. Softwood and hardwood fibers are both papermaking fibers and the size differences are inherent features. Pulp fibers typically consist of 40 – 50% cellulose, 20 – 35% hemi-cellulose, 15 – 35% lignin, and the remaining fraction contains resins, ash, and a whole range of miscellaneous compounds.

One of the prime difficulties in papermaking is fiber flocculation. Fibers tend to entangle together and create small, concentrated areas called flocs. Mason & Manley (1957) find that mechanical entanglement is the principle reason for flocculation. Fibers entangle, bend, and remain networked from frictional forces transmitted by fibers that are locked into bent configurations. It is well established that fiber flocs are generated by mechanical entanglement. The result of fiber flocculation and a preferred fiber orientation

is non-uniformity in paper sheets. This non-uniformity can adversely affect final product properties such as strength and printing quality. Also, high non-uniformity causes increases in coating consumption. Thus, understanding the factors that control the suspension properties in papermaking process is crucial.

The goal of this work is to obtain insight into fiber suspensions by studying the behavior of flexible fibers in shear flow using a coupled lattice Boltzmann and finite element method. In Chapter 2, prior works by other researchers in the area of fiber suspensions are introduced and discussed. The comparisons among fiber simulation methods as applied in fiber suspension rheology are discussed. From chapter 2, it is desired to understand the fundamental or background and motivation following the subsequent work of next chapters.

Chapter 3 contains computational method and simulation results. The background of the lattice Boltzmann method and finite element method are discussed. A coupled simulation method (lattice Boltzmann and finite element methods) is presented for investigating the relationship between fiber characteristics and the properties of fiber suspensions. Fibers are modeled as rigid and flexible rod like particles. The particles are simulated using the finite element method. The fluid flow that causes particles to deform is determined by the lattice Boltzmann method. The fibers may interact through contact forces to study the fiber characteristics that affect the fiber orientation and flocculation. Fiber-fiber interactions are discussed thoroughly in this chapter.

The simulation results are presented for two dimensional and three dimensional cases. Each case is evaluated with the theoretical and experimental values. Furthermore,

the fiber characteristics, fiber aspect ratio and fiber flexibility, are considered to investigate fiber orientations and fiber end segment displacements.

Rheological property as relative viscosity of simulated fiber suspension in simple shear flow is presented in Chapter 4. The suspension viscosity is strongly influenced by fiber flexibility, fiber aspect ratio, and volume fraction. The model is extended to simulate a fiber suspension in a simple diverging channel for papermaking application. The preliminary result is presented.

Finally, the main conclusions from this research are summarized in Chapter 5. Also presented in this chapter are recommendations for future works.

CHAPTER 2

LITERATURE REVIEW

In general, the motion of Newtonian fluids is given by the Navier-Stokes equations and continuity equations. The Navier-Stokes equations are the fundamental partial differential equations that describe the flow of incompressible fluids (constant fluid density). The Navier-Stokes equations are represented as follows,

$$\frac{\partial \mathbf{u}}{\partial t} + \mathbf{u}.\nabla \mathbf{u} = -\frac{1}{\rho}\nabla P + \nu \nabla^2 \mathbf{u} + \frac{1}{\rho}\mathbf{F}_g \quad , \tag{2.1}$$

where: $\mathbf{u} = u\mathbf{e}_x + v\mathbf{e}_y + w\mathbf{e}_z$ is the velocity vector with its three components (u, v, w) and P is the pressure. The kinematic viscosity ($\nu = \mu/\rho$) is the dynamic viscosity (μ) divided by the density (ρ) for a Newtonian fluid. The term $\mathbf{F_g}$ represents a volumetric force (for example gravity), which can be neglected in some problems. The term on the left-hand side of the equation is due to the acceleration of the fluid, also referred to as inertia terms, whereas on the right-hand side of the equation the first term is the pressure gradient (force), and the second term represents viscous forces. A principal difficulty in solving the Navier-Stokes equation arises because of the nonlinearity in the convective acceleration terms. There are no general analytical schemes for solving nonlinear partial differential equations, and each problem must be considered individually. For most

practical problems, fluid particles do have accelerated motion as they move from one location to another in the flow field. Thus, the convective acceleration terms are usually important; however, there are a few special cases for which the convective acceleration vanishes because of the nature of the geometry of the flow system.

The Navier-Stokes equations apply to both laminar and turbulent flow, but for turbulent flow, each velocity component fluctuates randomly with respect to time and this added complication makes an analytical solution intractable.

The continuity equation is expressed as

$$\frac{\partial \rho}{\partial t} + \nabla . \rho \, \mathbf{u} = 0 \,, \tag{2.2}$$

To solve this system of equations, initial and boundary conditions are needed. A rigid, impermeable or solid wall is employed for a boundary condition. This condition implies that no fluid is able to pass through the wall, consequently, the wall normal velocity is zero. Additionally, the two other components (parallel to the wall) are also zero. This boundary condition is usually referred to as a no-slip condition.

In addition to these equations, the motion of a solid particle in a fluid is expressed as

$$m \frac{d\mathbf{U}}{dt} = \mathbf{F} \,, \tag{2.3}$$

where **U** is the velocity (or angular velocity) of the particle, *m* is its mass (or moment of inertia) and **F** is the total force (or torque) acting on the particle.

A useful non-dimensional parameter for determining the behavior of fluid flows is referred to the Reynolds number. This parameter could be used as a criterion to distinguish between laminar and turbulent flow. In most fluid flow problems there will be a characteristic length, ℓ, and a velocity, U, as well as the fluid properties of density, ρ, and dynamic viscosity, μ, which are relevant variables in the problem. Thus, with these variables the Reynolds number

$$\mathrm{Re} = \frac{\rho U L}{\mu}, \tag{2.4}$$

arises naturally from the dimensional analysis. The Reynolds number is a measure of the ratio of the inertia forces to viscous forces on the fluid. When these two types of forces are important in a given problem, the Reynolds number will play an important role. However, if the Reynolds number is very small (RE << 1), this is an indication that the viscous forces are dominant in the problem, and it may be possible to neglect the inertial effects; that is, the density of the fluid will not be an important variables. These flows are commonly referred to as creeping flows. Conversely, for large Reynolds number flows, viscous effects are small relative to inertial effects and for these cases it may be possible to neglect the effect of viscosity and consider the problem as one involving a non viscous fluid or inviscid flow.

These basic fluid mechanics equations can be used to theoretically model the motion of fibers in fluid in order to obtain the rheological characteristics of fiber suspensions, such as orientation diffusion coefficient, and bulk stress. There are several steps which have been summarized by Petri (1999), being: (1) modeling the motion of individual fiber, (2) modeling the evolution of the orientation distribution of many fibers, and (3) estimating the contribution fibers to the rheological characteristics.

Mackaplow & Shaqfeh (1998) study the fiber motion during sedimentation. They find that the motion of a fiber depends on its orientation in the flow field. The fiber orientation is an important physical quantity. This effect is seen in extrusion of fiber-reinforced composites and in papermaking, where the mechanical properties are strongly linked to the fiber orientation. Hence, the interaction between fibers, the effect of the fiber structure on the rheological properties of fiber suspensions, and the fiber orientation distribution in flow fields are important problems bearing on both scientific interest and industrial applications.

The volume fraction and fiber aspect ratio are two parameters influencing the structure and rheological properties of fiber suspensions. The volume fraction, ϕ, is defined as the total volume of particles in a unit volume of suspension. The number density, n, is the number of particles per unit volume of suspensions, which is a parameter equivalent to the volume fraction, i.e. $\phi = n \times$ (volume of one particle). The aspect ratio, A_r, is defined as the length of the particle, L, divided by the diameter of the particle, d. The rheological properties and fiber structures are the result of the interaction among fibers in the suspension flow. The fiber interactions depend not only on the number of fibers in a certain volume, but also on the length of fibers.

Krekes & Schell (1992, 1995) introduce the concept of Crowding Factor, N_c,

$$N_C = \frac{2}{3}\phi\left(\frac{L}{d}\right)^2, \tag{2.5}$$

Experimentally, Kerekes has derived a relationship between the *Crowding Factor* and type of fiber contacts at different concentrations (See table 1)

Table 1: Fiber contacts at different crowding factor levels

Crowding Factor	Concentration	Type of fiber contact
$N_c < 1$	Dilute	Rare Collision
$1 < N_c < 60$	Semi-Concentrated	Frequent Collision
$N_c > 60$	Concentrated	Continuous Contact

Different group parameters, such as nL^3 and nL^2d, are used to classify fiber suspensions. For suspensions with rod-like particles, the volume fraction is $\phi = n\pi d^2 L/4 \approx nd^2 L$. These two parameters are equivalent to ϕA_r^2 and ϕA_r, respectively. Fiber suspensions are divided into three regimes: dilute, semi-dilute, and (semi-) concentrated regimes (See table 2).

Table 2: Regimes in fiber suspensions

	Regime	Type of fiber contact
$nL^3 << 1$	Dilute	Rare Collision
$nL^3 > 1$ or $nL^2d > 1$	Semi-Dilute	Frequent Collision
$nL^2d > 1$	(Semi-)Concentrated	Continuous Contact

The suspension is called dilute if there is much less than one fiber, on average, in a volume of $V = L^3$. Each fiber can therefore freely rotate without any hindrance from surrounding fibers with three rotational degrees of freedom. Since there is at most only

one fiber in a volume V, this leads to $\phi << d^2 L / V$, i.e. $nL^3 << 1$ or $\phi A_r^2 << 1$. In the semi-dilute regime, the number density of fibers should be in the range of $1/V < \phi < 1/L^2 d$. This leads to . $nL^3 > 1$ or $nL^2 d > 1$ or $1 < \phi A_r^2 < A_r$. In semi-dilute suspensions, the average distance between two neighboring fibers is greater than a fiber diameter, but less than a fiber length. The hydrodynamic interactions among fibers become stronger but do not drive significant fiber-fiber contacts. Finally, the concentration regime $\phi A_r > 1$ or $nL^2 d > 1$ is called (semi-) concentrated, where the average distance between two neighboring fibers is less than its diameter. Therefore, a fiber cannot rotate independently except about its symmetry axis; any motion of the fibers must necessarily involve a cooperative effort of all surrounding fiber, and fiber-fiber contacts are dominant.

Single fiber in motion

For dilute suspensions, $nL^3 << 1$, there is much less than one fiber in a volume of L^3 on average and hydrodynamic interactions among particles are negligible. Each fiber moves as a single fiber and the inertia and Brownian motion of the fibers are usually negligible. The basic study of dilute particle dynamics is attributed to Jeffery (1922). He investigates the motion of a rigid ellipsoid particle in shear flow, neglecting inertia. His analytical solutions describe the orientation of the particle, and his calculations show that a particle rotates around the vorticity axis in a path known as Jeffery's orbit.

Experimentally, Forgac & Mason (1959) calculate the average rotation of fibers in linear shear flow, both in the dilute and semi-dilute regime. They conclude that Jeffery's

theory continues to provide a good approximation describing fiber rotation, even in the semi-dilute regime.

In a fiber suspension (no fiber-fiber collisions), the stress will vary periodically and never reach a steady-state condition. Jeffery's theory gives coupled differential equations for the fiber orientation in the spherical coordinates (φ, θ) and their solution as:

$$\tan \varphi = A_r \tan\left(\frac{Gt}{A_r + A_r^{-1}}\right), \tag{2.6}$$

$$\tan \theta = \frac{C \; A_r}{\sqrt{\left(A_r^{\,2} \cos^2 \varphi + \sin^2 \varphi\right)}}, \tag{2. 7}$$

where A_r is the fiber aspect ratio (A_r=L/d where L is the particle length and d is the particle diameter), G is the shear rate, and C is a constant of integration, called *the orbit constant*.

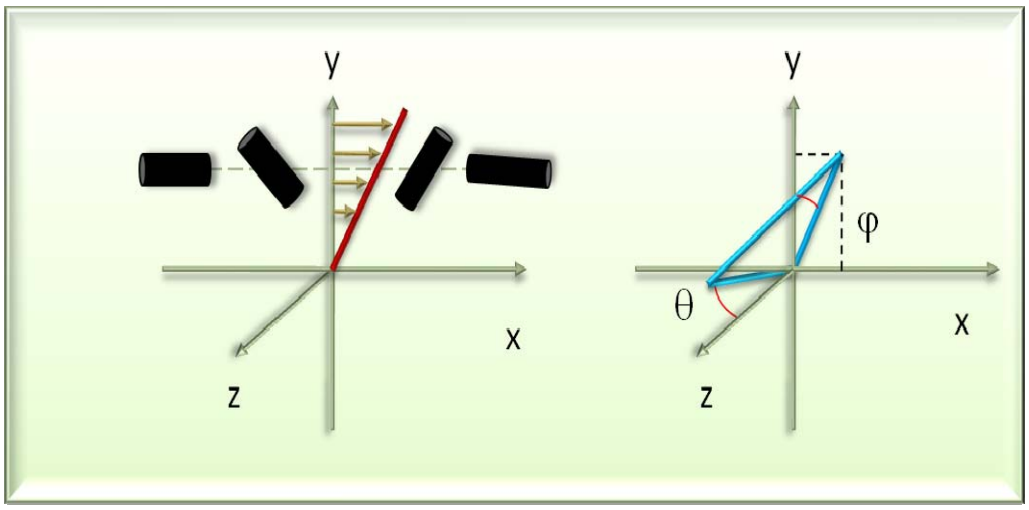

Figure 2.1: Schematic showing a single fiber in a simple shear flow

The time, t is the local time in the orbit and the constant C can take any positive values. With $C=0$, the fiber is aligned along the z-axis, and the orbit constant corresponds to a log rolling motion where the fiber spins in the vorticity direction. An orbit constant of $C \rightarrow \infty$ the fiber corresponds to rotating in the xy plane, in which the fiber tumbles in the plane of shear.

The time the fiber spends in the orbital period depends on the shear rate and the aspect ratio. In general, a single fiber with a large aspect ratio spends most of the time roughly aligned in the direction of flow and quickly flips every half period. For very slender particles with fiber aspect ratio $A_r >> 1$, the theory by Jeffery can be simplified, which is presented by Burger (1938). The results of the simplified coupled differential equations are

$$\frac{d\theta}{dt} = \frac{G}{4} \sin 2\theta \sin 2\varphi \,, \tag{2.8}$$

$$\frac{d\varphi}{dt} = G \cos^2 \varphi \tag{2.9}$$

Jeffery's theory provides a relation between the rate of rotation and the aspect ratio, and resulted in an introduction of an effective aspect ratio. Bretherton (1962) extends the work of Jeffery and shows that any fore-and-aft symmetric particle rotates with an orbital period

$$T = {2\pi (A_r + A_r^{-1})}/{G} \,, \tag{2.10}$$

if an effective aspect ratio A_{reff} is used. However, several studies have tried to determine a uniquely defined effective aspect ratio, and this has not been realized. The values depend on the aspect ratio and shape of the fiber ends.

Experimentally Mason & Manley (1957) estimate that $A_{reff} = \lambda A_r$ where $\lambda = 0.7$ for $A_r = 19.1$, and $\lambda = 0.64$ for $A_r = 66$. Additionally, Petrich & Koch (1998) determine $\lambda = 0.687$ for $A_r = 50$, and $\lambda = 0.623$ for $A_r = 70$. These results agree with the formula obtained by Cox (1971)

$$\frac{A_{reff}}{A_r} = \frac{K}{\sqrt{(\ln A_r)}}, \tag{2.11}$$

where K is a constant depending on the aspect ratio of the actual particles.

Fiber suspensions

When $nL^3 \geq 1$, the hydrodynamic interactions among fibers become stronger and cannot be neglected. This regime of the fiber suspensions can be considered as semi-dilute or semi-concentrated. Koch & Shaqfeh (1990) develop a semi-dilute theory and validate it with experiments (Petrich *et al.* 1998) and numerical simulations (Mackaplow & Shaqfeh, 1996; Sundararajakumar & Koch, 1997). Koch & Shaqfeh (1990) calculate the average rotation of fibers in a linear shear flow, both in the dilute and semi-dilute regime. They conclude that Jeffery's theory continues to provide a good approximation to the fiber rotation, even in the semi-dilute regime.

Mackaplow & Shaqfeh (1996) show that predicted viscosities based solely on hydrodynamic interactions deviate from experimental measurements in the concentrated regime. Such a deviation is explained by the leading role of mechanical contact between

fibers in the concentrated regime. The nature of fiber-fiber contact in the concentrated regime is also investigated experimentally by Petrich & Koch (1998). They show the viscosity increasing with concentration much more rapidly than predicted for purely hydrodynamic interactions. Again, the increased viscosity has been attributed to mechanical contacts between fibers.

Numerous studies for rigid fiber suspensions have been developed (Batchelor, 1970a; Claeys & Brady, 1993a, 1993b; Yammane *et al*., 1995; Sundarajakumar & Koch, 1997). Batchelor (1970a) derives an expression for the particle stress using slender body theory for rigid fiber suspensions in the dilute flow regime. In addition, he determines a bulk average stress for a suspension of fibers in a Newtonian fluid (Batchelor, 1970b, 1972).

Claeys & Brady (1993a, 1993b) model fibers as rigid prolate spheroids and develop a method for determining the short-range hydrodynamic interactions (lubrication forces) and the long-range, many-body hydrodynamic interactions. Yammane *et al*. (1995) simulate semi-dilute suspensions of rigid rodlike particles in shear flow. The short-range hydrodynamic interaction (lubrication approximation) is taken into account, whereas they ignore the long-range hydrodynamic interaction.

Sundarajakumar & Koch (1997) simulate semi-concentrated suspensions of rigid slender rods interacting through contact forces. In a suspension of smooth spherical particles, lubrication forces are indeed sufficiently strong to prevent solid-body contacts. In the case of slender fiber, they observe that lubrication is not so strong as to prevent actual physical contact between fibers. The lubrication force resisting normal relative motion is related to the instantaneous minimum gap-thickness h(t) (Sundararajakumar *et*

al. 1997). Since the gap-thickness is much smaller than the asperities on the fibers, they conclude that actual physical contact must occur.

In recent years, research has been extended to flexible fibers considering the actual material properties of many particles or fibers in fluid flow. Yamamoto & Matsuoka (1993, 1994) model flexible fibers as chains of rigid spheres connected through springs. The fiber model can stretch, bend and twist by changing bond distance, bond angle and torsion angle between spheres, respectively. They define flexibility parameters for this fiber model, including stretching, bending, and twisting constants for a pair of bonded spheres. Chain connectivity between spheres is maintained by constraints, producing equations that must be solved simultaneously with the equation of motion, which requires extensive computational time. Their model for flexible fibers agrees with the experimental work by Forgacs & Mason (1959).

Another flexible fiber is constructed by Ross & Klingenberg (1997). The fibers are modeled as chains of rigid prolate spheroids connected by ball and socket joints. The resistances in the joints are varied depending on the fiber's flexibility. This model reduces the iterative constraints for solving fiber connectivity and can model high aspect ratio fibers. These features help to simplify computations and facilitate simulation of concentrated suspensions. Following this work (Ross & Klingenberg, 1997), Schmid *et al.* (2000) model flexible fibers as chains of elongated bodies (rigid rods). They demonstrate that flocculation can be induced by purely mechanical means, i.e. interparticle friction, elastic fiber deformation and irregular equilibrium shapes. Switzer III & Klingenberg (2003) investigate the relationships between fiber properties and fiber-fiber interaction and the resulting rheological properties based on the suspension model

by Schmid *et al*. (2000). They show that the rheological properties depend on fiber and suspension characteristics such as the equilibrium shape, flexibility, aspect ratio, friction, concentration, and suspending fluid characteristics. The fibers are modeled as chains of interconnected rods under shear flow condition and fiber-fiber contact and hydrodynamic interactions are ignored. Lindstrom and Uesaka (2007, 2008) develop flexible fibers which are modeled as chains of fiber segments. This work is a further study from Schmid *et al*. with several additions into the new model includes the effects of particle inertia, non-creeping fiber fluid interactions, hydrodynamic interaction between fibers, self-interactions, and the introduction of artificial damping the fiber segment joints to reduce the numerical instability of the new model.

Fiber flocculation

In application such as papermaking and fiber-reinforced composites, a homogenous dispersion of fibers is desired in order to yield a uniform product. Wood pulp fibers in particular tend to aggregate in a process known as flocculation, which produces spatially heterogeneous structures. The term flocculation is defined as the state of non uniformity in a fiber suspension, or as the process by which fiber flocs form. According to Parker (1972), the minimum number of fibers required to form a floc with distinct mechanical properties is four. Therefore, a floc can be as small as four fibers and increase in numbers to quite large amounts.

Flocculation only occurs if fibers interact. Experiments have demonstrated that numerous factors affect flocculation including concentration, fiber shape, fiber aspect ratio, shear rate, and type of fluid flow. The mechanisms that produce the fiber

flocculation are related to fiber-fiber contact. For many fiber suspensions, mechanical and elastic effects are the dominant mechanisms that determine fiber structure and fibers networks (Forgas & Mason, 1958; Kerekes, *et al*, 1985; Mason, 1950). Phenomena of *mechanical surface linkages* form due to contacts involving irregularly shaped fibers. Fibers found in pulp suspensions are naturally deformed at equilibrium and may become entangled by hooking. In addition to that, fibers may be fibrillated, that is small fibrous entities of the fiber may extend out from the fiber surface. In this case, the fibrils of contacting fiber surfaces may become mechanically entangled. A phenomenon of elastic fiber interlocking occurs when flexible fibers form an elastic network. Flowing fiber suspensions may experience sufficient viscous forces to cause fibers to elastically deform. As the fibers attempt to relax, they can become locked in elastically strained configurations due to contacts with other fibers. The fiber surfaces experience friction forces which are proportional to the normal force between fibers, and the normal force is a function of the fiber flexibility.

Fiber suspension rheology

Relative viscosity

Hydrodynamic theories that predict the Newtonian viscosity for suspensions have been developed for different shapes of particles. These theories can be shown in general,

$$\mu_r = 1 + \alpha_0 \phi , \tag{2.12}$$

where μ_r is the relative viscosity ($\mu_r = \frac{\mu}{\mu_0}$), ϕ is the volume concentration, and α_0 is a dimensionless factor determined by the shape, dimensions, and orientations of the suspended particles.

Burger (1938) derives a dimensionless factor (α_0) for the case of cylindrical rods

$$\alpha_0 = \left[\frac{\left(L/d \right)^2}{6\left(\ln \frac{2L}{d} - 1.80 \right)} \right] \sin^4 \theta \sin^2 \varphi \,, \qquad (2.13)$$

where L/d is the length-to-diameter or aspect ratio of the rod and θ and φ are the spherical coordinate. He neglects wall effects, Brownian motion, slip, and particle interactions. In addition, he neglects effects due to the thickness and ends of the rods.

Experimental studies on the viscosity of suspensions of rigid rods have been made by Nawab and Mason (1958), and Myers (1962), where none of their results agreed with theory or among themselves. Nawab and Mason show their experimental data, and they suggest the data are about three times larger than predicted by Burgers due to curved fibers used in the viscosity determinations. Therefore, it is expected that fiber curvature has a significant effect on the viscosity. Kitano *et al.* (1981) present an empirical relationship between relative viscosity and volume fraction for various fillers such as glass and carbon fibers. Their results suggest different materials would produce different suspension viscosities. Goto *et al*. (1986a, b) determine experimentally the relationship between fiber flexibility and suspension viscosity. They find more flexible fibers produce higher viscosity than the stiffer fibers. In this work, a computational method is applied to

understand the relationship between fiber properties and relative viscosity in simple shear flow.

Fiber properties

Wood fibers vary in length, width, and cell wall thickness and these differ widely within and between wood species. Hardwood fibers are shorter than softwood, make lower strength pulps, and usually exhibit a narrower distribution for their important dimensions. Softwood tracheids or hardwood fibers are both papermaking fibers and the size differences are inherent features (see tables 3, 4, 5 for fiber properties).

Softwood fiber

Fibers from northern softwood species produce a different balance of product properties than those from Douglas fir and southern pines. Northern fibers exhibit better fiber bonding, higher tensile and burst strength, and lower tear strength than kraft pulps of Douglas fir or southern pine. Although studies show that the chemical composition does not vary significantly between these fiber types, the fiber dimensions are very different.

Species:

Norcan Softwoods: *White Spruce, Black Spruce, Jack Pine, Balsam Fir, Norway Spruce, Scotch Pine, White Pine, Silver Fir, Alpine Fir, Norway Pine, Eastern Hemlock.*

Southern Softwoods: *Loblolly Pine, Shortleaf Pine, Longleaf Pine, Slash Pine, Parana Pine, Maritime Pine.*

West Coast Softwoods: *Douglas fir, Western Hemlock, Redwood, Western Red Cedar, Ponderosa Pine, Western Larch, Sitka Spruce, Englemann Spruce, Lodgepole Pine.*

Hardwood fiber

Hardwood fibers also display differences associated with the region in which they are grown. Commercially, hardwood pulps are used in paper and board grades intended for printing where the highest quality surface properties and appearance are needed. The fine hardwood fibers promote good formation, bulk, smoothness, and opacity compared with longer and coarser softwood fibers.

Species:

Northern Hardwoods**:** *Bigtooth aspen, Quaking aspen, Balsam Poplar, Black Cottonwood, Yellow Birch, Paper Birch, Red Alder, Beech, European Oak, Sugar Maple, Red Maple, Ash.*

Southern Hardwood: *Black Willow, Southern Cottonwood, White Oak, Hickory, Yellow Poplar, Red Gum, Sycamore, Tupelo.*

Eucalyptus: *E. globulus, E. tereticornis, E. Calmaldulensis, E. Saligna.*

Table 3: Wood fiber properties A

Fibers	Fiber Diameter (mm)		Fiber Length (mm)		Aspect Ratio	Poisson ratio
	Range	Average	Range	Average		
Softwood Fibers:	0.025 - 0.035	0.03	3.0 - 4.0	3.2	100	0.280 - 0.392
Norcan Softwood	0.025 - 0.030	0.03	3.0 - 3.5	3	100	0.3
Southern Softwood	0.035 - 0.045	0.04	3.1 - 3.6	3.5	87	0.328 - 0.332
West Coast Softwood	0.035 - 0.045	0.04	3.5 - 4.0	3.5	87	0.318 - 0.392
Hardwood Fibers	0.016 - 0.025	0.022	0.8 - 1.5	0.9	40	0.318 - 0.430

Table 4: Wood fiber properties B

Fibers	Basic Specific gravity	Density (g/cm3)	Wall thickness (mm)		Coarseness (dg)	
			range	average	range	average
Softwood Fibers:	0.32 - 0.56	0.3 - 0.56	0.002 - 0.007	0.004	18 - 32	22
Norcan Softwood		0.37 - 0.49	0.002 - 0.01	0.0044		19.8
Southern Softwood		0.31 - 0.48	0.0017 - 0.007	0.0036	25 - 32	26
West Coast Softwood		0.46 - 0.56		0.0038	22 - 32	26
Hardwood Fibers	0.32 - 0.64	0.37 - 0.64	0.0016 - 0.006	0.003	8.6 - 20	14

Table 5: Wood fiber properties C

Fibers	Compression parallel to fiber direction (GPa)	Compression perpendicular to fiber direction (GPa)	Shear Parallel to fiber direction	Tensile strength (Gpa)	Young's Modulus (Gpa)
Softwood Fibers:	31.4 - 58.4	2.8 - 7.8	6.1 - 11.6	45.5 - 111.7	7.7 - 13.7
Norcan Softwood	37.3 - 44.2	3.1 - 4.5	7.3 - 8.5		8.3 - 12.1
Southern Softwood	49.2 - 58.4	5.4 - 6.6	9.6 - 11.6	80	12.1 - 13.7
West Coast Softwood	31.4 - 49.0	2.8 - 7.8	6.1 - 8.6	45.5 - 111.7	7.7 - 12.9
Hardwood Fibers	51.1 - 70.2	2.6 - 19.6	5.4 - 18.3	51-120.7	7.0 - 15.7

Fiber simulation methods

In early studies, the boundary element method (BEM) is used to study suspensions (Pan-Thien & Kim, 1994). BEM is a useful and accurate technique to solve Stokes flow past particles with arbitrary shape; however, BEM generates a boundary integral equation of the first kind, which does not converge well in numerical iterative solution. Pan-Thien & Kim (1994) simulate periodic suspensions of prolate spheroids accounting for the hydrodynamic interaction among particles. The computation demand of BEM limited their applications in suspension simulation. Clays & Brady (1993) employ a different numerical method called Stokesian dynamics to simulate the suspension of prolate spheroids, accurately evaluating both long-range and short-range

hydrodynamic interactions. Though accurate, Stokesian dynamics simulations are still too computationally demanding to simulate the microstructure evolution of fiber suspensions.

More efficient methods are developed in terms of approximately calculating the fiber interactions. Mackaplow and Shaqfeh (1996) use slender body theory to simplify the boundary integral equations for fibers and account for the hydrodynamic interactions among fibers. This method underestimates the short-range hydrodynamic interactions, because the slender body theory works only for remote particles. Fan *et al.* (1998) use the slender body approximation to calculate the long-range hydrodynamic interaction among fibers and the lubrication approximation to calculate the short-range hydrodynamic interactions between close neighboring fibers.

Particle-level simulations are another common method used for investigating particle suspensions (Fan *et al*., 1998; Joung *et al*., 2001, 2002; Sundararajakumar & Koch, 1997; Switzer & Klingenberg, 2003; Yammane *et al*., 1995; Yamamoto & Matsuoka, 1993, 1994; Ross & Klingenberg, 1997; Schmid *et al*., 2000; Switzer III & Klingenberg, 2003; Lindstrom & Uesaka, 2007). Yamamoto and Matsuoka *et al.* (1993) develop the Particle Simulation Method (PSM), which is based on the Stokesian Dynamics framework with a few important differences. First, the rigid spheres in Stokesian Dynamics method are no longer independent entities, but linked by internal bonds to construct fiber-like bead-chain structures. Linkages between spheres exhibit linear extension, bending and torsional stiffness, allowing the bead-chain structures deform elastically. Ross and Klingenberg (1997) utilize a similar method to produce their Particle-level Dynamic Simulation. Unlike Yamamoto and Matsuoka who construct structures from linked spheres in direct contact with each other, Ross & Klingenberg

attempt linking prolate spheroids and widely spaced ball-and socket subunits in order to reduce the number of simulated bodies. In particle-level simulation methods, each particle is solved numerically using the equation of motion to obtain the particle position and orientation over time, therefore predicting the suspension microstructure. However, since this is a microscopic method, solving the equation of motion for fibers in a suspension at each instant of time is a computationally demanding process.

Dewei Qi (2006) has constructed a new method for direct simulation of flexible fibers using lattice Boltzmann method. For the fluid phase, simulations are based on a lattice Boltzmann equation, and for the solid domain, a slender solid body is discretized into a chain of consecutive spherical segments contacting each other. The method is verified using a rigid particle method, and the results demonstrate a reasonable accuracy and are consistent with existing experimental results for inertial flows.

This current project uses the similar method to Dewei Qi, which is based on lattice Boltzmann method; however, the slender body is modeled using a finite element method.

CHAPTER 3

COMPUTATIONAL METHOD AND SIMULATIONS

Lattice Boltzmann method (LB)

To understand the motivation for using the LB method, general modeling methods for particle suspensions are explained. Basically, there are three main method catgories used to model particle suspensions. Wolffe *et al*. (2002) review their relative advantages and disadvantages.

The first category is called the macroscopic method. The method models the particle suspension as a continuum media using the Navier-Stokes equations for incompressible fluid flow and then the particle suspension is discretized by mesh generation. Mesh generation is a discretization of a geometric domain into elements such as triangles for two-dimensional meshes and tetrahedrons for three-dimensional domains. The outcome of the model is a system of nonlinear equations, which can be solved using finite element (FE) or finite-difference numerical methods. This macroscopic method has been used successfully to model particle suspensions such colloidal particles and sedimentation (Brady & Bossis, 1988, Hu *et al*., 1992). However, it is computationally expensive in systems with fine resolution meshes, particularly for three-dimensional cases.

The second category is the so-called microscopic approach. The method models the molecular world and is known as molecular dynamics (MD) simulations. Each particle is solved using equation of motion to determine the particle position and velocity

over time. Since each particle follows the exact same rules of motion, the method is easy to implement and parallel, however, solving the equations of motion for a large number of particles at each instant of time is a computationally intensive process.

The third category is the mesoscopic method, which includes the LB method. The method uses cellular automata organized into a restricted lattice structure. Instead of discretizing the continuum Navier-Stokes equations, fluid particles are situated at each discrete point of the lattice. Through statistical averaging, the collective behavior of the fluid particles approximates the dynamics of the continuum equations. The LB method is a powerful technique for simulating fluid flow and modeling fluid physics (Ladd, 1994a,b; Ladd & Verberg, 2001; Aidun & Lu, 1995; Aidun, Lu & Ding, 1998; Aidun & Qi, 1998). Some advantages of this method include a straightforward implementation of physical rules, easy incorporation of complex geometries and the ease of parallelization. The core concept behind the LB method is the solution of the Boltzmann equation on a regular lattice using discrete velocities. At every time step, fluid particles propagate to neighboring lattice nodes and undergo a collision operation, which redistributes the momentum. Local mass and momentum for given nodes are obtained by summing the particle mass and momentum on the links coming from the nodes. The LB equation is written as (McNamara & Zanetti, 1988; Chen *et al*., 1992; Hou *et al*., 1995),

$$f_{\sigma i}(\mathbf{x}+\mathbf{e}_{\sigma i},t+1) = f_{\sigma i}(\mathbf{x},t) - \frac{1}{\tau}[f_{\sigma i}(\mathbf{x},t) - f_{\sigma i}^{(0)}(\mathbf{x},t)] \quad , \tag{3.1}$$

where $f_{\sigma i}^{(0)}(\mathbf{x}, t)$ is the equilibrium distribution at position $\mathbf{x}$, and time t, $f_{\sigma i}(\mathbf{x}, t)$ is the single-particle distribution function, ρ is the node density, $\mathbf{e}_{\sigma i}$ is the velocity vector in the

σi direction, and τ is the relaxation time. Figure 3.1 shows a diagram of velocity model for simulating two dimensional flows.

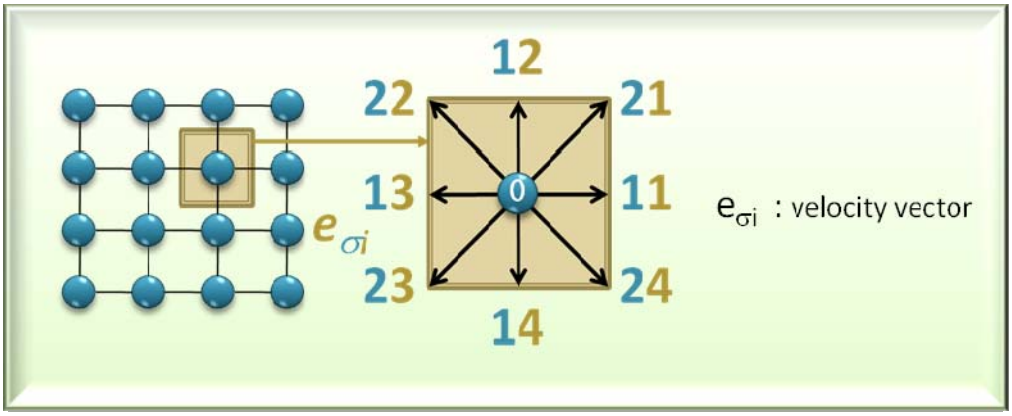

Figure 3.1: Two-dimensional lattice spacings

In three-dimensional cases, there are several possible lattice arrangements fifteen-velocity (D3Q15), nineteen-velocity (D3Q19), and twenty-seven-velocity (D3Q27). Mei *et al.* (2000) investigate the three-dimensional cases lattice Boltzmann velocity models and analyze the efficiency, accuracy and robustness of each. The velocity models with the boundary treatment are determined for several different problems including fully developed flows in a square duct, flow in a 3-D lid-driven cavity, fully developed flows in a circular pipe, and a uniform flow over a sphere. They find that the D3Q15 model is prone to numerical instability, the D3Q27 model is computationally intensive and the D3Q19 model provides a balance of computational reliability and efficiency (increase computational speed and stability). Hence, for this research, the nineteen-velocity (D3Q19) velocity models is chosen for $\mathbf{e}_{\sigma i}$. Figure 3.2 shows schematic of lattice

spacings for the D2Q9 and D3Q19 models. Tables 6 and 7 provide the velocity vector for two-dimensional case (D2Q9) and three-dimensional case (D3Q19).

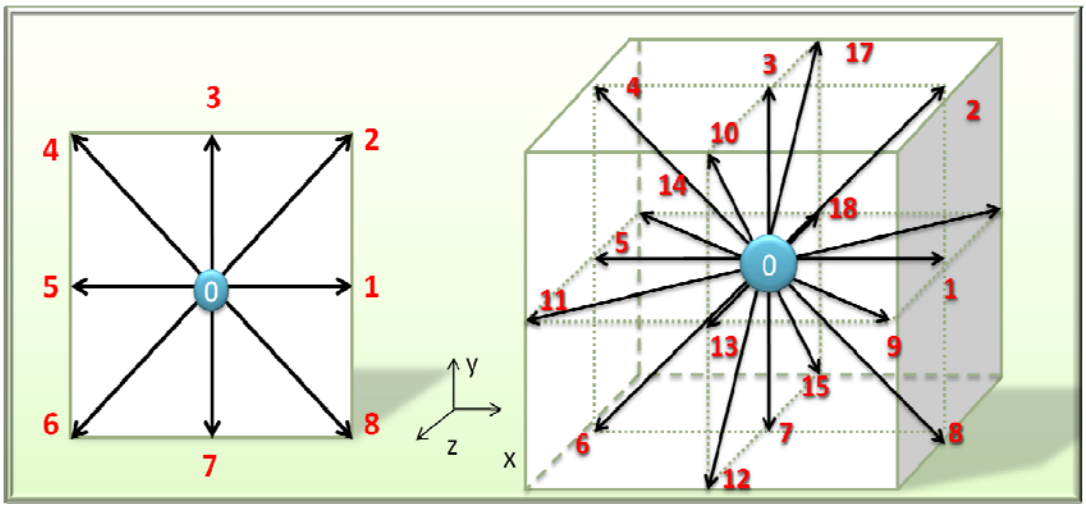

Figure 3.2: Schemactic lattice spacings two-dimensional nine-velocities (D2Q9) and three-dimensional eighteen-velocities (D3Q18)

Table 6: Velocity vector for two-dimensional nine-velocities (D2Q9)

k	σ	i	$e_{\sigma ix}$	$e_{\sigma iy}$	$\lvert e_{\sigma i} \rvert$
0	0	1	0	0	0
1	1	1	1	0	1
2	1	2	0	1	1
3	1	3	-1	1	1
4	1	4	0	-1	1
5	2	1	1	1	√2
6	2	2	-1	1	√2
7	2	3	-1	-1	√2
8	2	4	1	-1	√2

Table 7: Velocity vector for three-dimensional eighteen-velocities (D3Q19)

k	σ	i	$e_{\sigma ix}$	$e_{\sigma iy}$	$\lvert e_{\sigma i} \rvert$
0	**0**	**1**	**0**	**0**	**0**
1	**1**	**1**	**1**	**0**	**1**
2	**2**	**1**	**1**	**1**	**√2**
3	**0**	**2**	**0**	**1**	**1**
4	**1**	**2**	**-1**	**1**	**√2**
5	**2**	**3**	**-1**	**0**	**1**
6	**0**	**3**	**-1**	**-1**	**√2**
7	**1**	**4**	**0**	**-1**	**1**
8	**2**	**4**	**1**	**-1**	**√2**
9	**2**	**5**	**1**	**0**	**√2**
10	**2**	**6**	**0**	**1**	**√2**
11	**2**	**7**	**-1**	**0**	**√2**
12	**2**	**8**	**0**	**-1**	**√2**
13	**1**	**5**	**0**	**0**	**1**
14	**2**	**9**	**-1**	**0**	**√2**
15	**2**	**10**	**0**	**-1**	**√2**
16	**2**	**11**	**1**	**0**	**√2**
17	**2**	**12**	**0**	**1**	**√2**
18	**1**	**6**	**0**	**0**	**√2**

The relaxation time is related to the viscosity by $\upsilon = {}^{1}\!/_{6}\,(2\tau - 1)$, where ν is the kinematics viscosity measured in lattice units. For τ = 1, the distribution functions are exactly set to the equilibrium distribution. The coefficients for the equilibrium distribution function are determined by conservation laws for mass, momentum and kinetic energy, and they are specified in two-dimensional and three-dimensional cases (Ding & Aidun, 2003). There are three types of particles on each node of a square lattice: a particle at rest $(\sigma = 0)$, a particle moving in a perpendicular direction $(\sigma = 1)$, and a moving particle in a diagonal direction $(\sigma = 2)$.

The equilibrium distribution function, $f_{\sigma i}^{(0)}(\mathbf{x},t)$ is defined as

$$f_{\sigma i}^{(0)} = \rho[A_\sigma + B_\sigma(\mathbf{e}_{\sigma i}\cdot\mathbf{u}) + C_\sigma(\mathbf{e}_{\sigma i}\cdot\mathbf{u})^2 + D_\sigma \mathrm{u}^2], \qquad (3.2)$$

where ρ is the density and $\mathbf{u}$ is the continuum velocity vector of the fluid. Tables 8 and 9 show the distribution coefficients for two dimensional and three dimensional cases.

Table 8: Equilibrium distribution coefficient for two-dimensional case

σ	A_σ	B_σ	C_σ	D_σ
0	4/9	0	0	-2/3
1	1/9	1/3	1/2	-1/6
2	1/36	1/12	1/8	-1/24

Table 9: Equilibrium distribution coefficient for three-dimensional case

σ	A_σ	B_σ	C_σ	D_σ
0	1/3	0	0	-1/2
1	1/18	1/3	1/4	-1/12
2	1/36	1/12	1/8	-1/24

A collision occurs when the particle distribution is relaxed toward equilibrium. Then, the particle distributions are streamed to their neighboring nodes along the direction of motion according to their velocities. At this point, boundary treatments and particle dynamics are applied. The no-slip wall bounce-back scheme is generally applied for boundary conditions, where the momentum from the incoming particle is bounced back in the opposite direction after the particle hits the wall. The scheme assumes that the wall is located halfway between nodes (Ladd & Verberg, 2001). For a stationary no-slip wall, it assumes that the fluid node is adjacent to the stationary no-slip wall. For a moving no-slip wall, the no-slip condition at the solid-fluid boundary assumes that the fluid adjacent to the solid surfaces moves at the same velocity as the solid surface. The bounce-back equation for a stationary and a moving no-slip wall can be found in Aidun *et al.* (1998). At the end of the LB time step, new macroscopic properties can be determined. The macroscopic properties of the fluid flow, density and velocity are given by

$$\rho(\mathbf{x},t) = \sum_{\sigma,i} f_{\sigma i}(\mathbf{x},t),$$
$$\rho(\mathbf{x},t)\ \ \mathbf{u}(\mathbf{x},t) = \sum_{\sigma,i} f_{\sigma i}(\mathbf{x},t) \bullet \mathbf{e}_{\sigma i} \tag{3.3}$$

Finite element method (FE)

Several computational methods for simulating flexible particles, mainly fibers, have been mentioned previously. The fiber model in these methods assumes a single flexible fiber composed as a chain of spheres. In this project, a single fiber is modeled as a rod-like particle using the FE method. The fiber is constructed as a continuum fiber

structure which makes the model more realistic to the actual fiber. In addition to that the fiber can be deformed using the finite element method. The FE method is employed because it is a well-developed method that has been applied to numerous problems. Commercial finite element modeling software (ANSYS) is used to model and mesh the fibers, as well as the calculation of global mass, damping, and stiffness matrices. The method can model irregularly shaped bodies and vary the size of the elements to make it possible to use small elements where necessary. Example time steps can be seen in figure 3.3, where a solid particle behaves like rigid at initial time to determine its translation and rotation, and then the deformation of a solid particle is calculated.

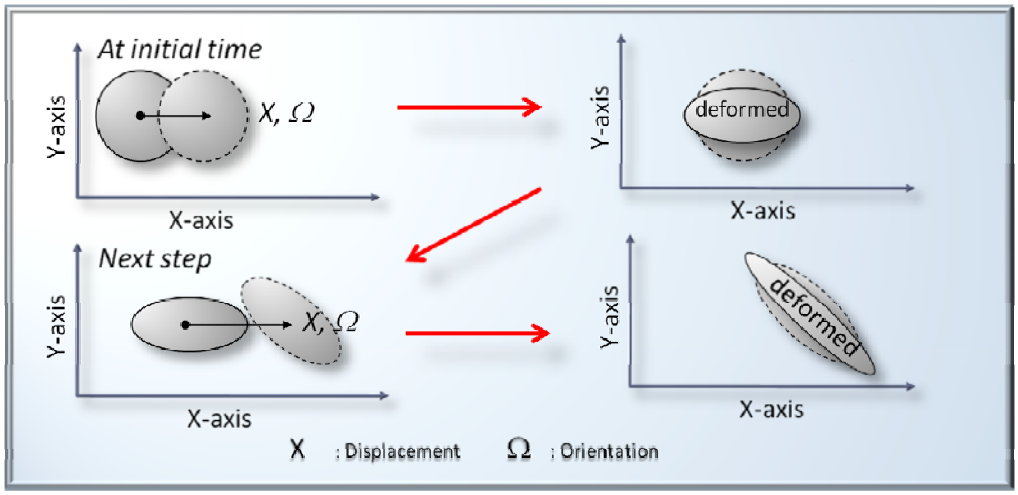

Figure 3.3: Step Simulation of a solid particle

The FE method uses small-interconnected elements to model a structure. A displacement function (for a two-dimensional case or a tetrahedron for a three-dimensional case) is associated with each element. Every interconnected element is linked, directly or indirectly, to every other element through common interfaces, including nodes, boundary lines, and surfaces. The total set of equations describing the

behavior of each node results in a series of algebraic equations best expressed in matrix notation.

Discretizing a FE model involves dividing the body into an equivalent system of finite elements with associated nodes and choosing the most appropriate element type. The total number of elements used and their variation in size and type within a given body are primarily engineering judgments. The elements must be made small enough to give usable results yet large enough to reduce computational effort.

Dynamic analysis

The equations of governing the linear dynamic response of system of finite elements are shown as:

$$\mathbf{M}\ddot{\mathbf{x}} + \mathbf{C}\dot{\mathbf{x}} + \mathbf{K}\mathbf{x} = \mathbf{F}\,, \tag{3.4}$$

where **M, C,**and **K** are the mass, damping and stiffness matrices calculated in ANSYS; **F** is the external load vector; $\mathbf{x}$, $\dot{\mathbf{x}}$ and $\ddot{\mathbf{x}}$ are the displacement, velocity, and acceleration vectors of the finite element assemblage. The external load consists of

$$\mathbf{F}_I(t) + \mathbf{F}_D(t) + \mathbf{F}_E(t) = \mathbf{F}\,, \tag{3.5}$$

where $\mathbf{F}_I(t)$ are the inertia forces, $\mathbf{F}_I(t) = \mathbf{M}\ddot{\mathbf{x}}$, $\mathbf{F}_D(t)$ are the damping forces, $\mathbf{F}_D(t) = \mathbf{C}\dot{\mathbf{x}}$, and $\mathbf{F}_E(t)$ are the elastic forces, $\mathbf{F}_E(t) = \mathbf{K}\mathbf{x}$, all of them being time-dependent. Therefore, in dynamic analysis, in principle, static equilibrium at time *t*,

which includes the effect of acceleration-dependent inertia forces and velocity-dependent damping forces, is considered. In static analysis, the equation of motions of finite element method (equation 3.4) is considered, with inertia and damping effects neglected.

The Newmark method

The dynamic finite element analysis is solved using Newmark method which is a direct integration method. The Newmark method expresses the deformation and velocity at time $t+1$ from t as in the following equation:

$$\dot{x}_{t+1} = \dot{x}_t + (\Delta t)\left[(1-\gamma)\ddot{x}_t + \gamma\,\ddot{x}_{t+1}\right], \tag{3.6}$$

$$x_{t+1} = x_t + (\Delta t)\,\dot{x}_t + (\Delta t)^2\left[\left(\tfrac{1}{2}-\beta\right)\ddot{x}_t + \beta\,\ddot{x}_{t+1}\right] \tag{3.7}$$

Equations 3.6 and 3.7 can be written as acceleration and velocity in the following form

$$\ddot{x}_{t+1} = \frac{1}{\beta(\Delta t)^2}\left(x_{t+1} - x_t\right) - \frac{1}{\beta(\Delta t)}\,x_t - \left(\frac{1}{2\beta} - 1\right)\ddot{x}_t, \tag{3.8}$$

$$\dot{x}_{t+1} = \frac{\gamma}{\beta(\Delta t)}\left(x_{t+1} - x_t\right) + \left(1 - \frac{\gamma}{2\beta}\right)\dot{x}_t + \Delta t\left(1 - \frac{\gamma}{2\beta}\right)\ddot{x}_t \tag{3.9}$$

Substituting $\mathbf{x}$, $\dot{\mathbf{x}}$ and $\ddot{\mathbf{x}}$ into the dynamic finite element equation gives

$$\left(\frac{1}{\beta(\Delta t)^2}\mathbf{M}+\frac{\gamma}{\beta(\Delta t)}\mathbf{C}+\mathbf{K}\right)x_{t+1}= \mathbf{F}_{t+1}+\mathbf{M}\left[\frac{1}{\beta(\Delta t)^2}x_t+\frac{1}{\beta(\Delta t)}\dot{x}_t+\left(\frac{1}{2\beta}-1\right)\ddot{x}_t\right]+ \mathbf{C}\left[\frac{\gamma}{\beta(\Delta t)}\dot{x}_t+\left(\frac{\gamma}{\beta}-1\right)\dot{x}_t+\left(\frac{\gamma}{2\beta}-1\right)\Delta t\,\ddot{x}_t\right], \tag{3.10}$$

where

$$a_0=\frac{1}{\beta(\Delta t)^2},\quad a_1=\frac{\gamma}{\beta(\Delta t)},\quad a_2=\frac{1}{\beta(\Delta t)},\quad a_3=\frac{1}{2\beta}-1,$$
$$a_4=\frac{\gamma}{\beta}-1,\quad a_5=\left(\frac{\gamma}{2\beta}-1\right)(\Delta t),\quad a_6=(1-\gamma)(\Delta t),\quad a_7=\gamma\Delta t,$$

Therefore the equation is simplified as

$$\underbrace{(a_0\mathbf{M}+a_1\mathbf{C}+\mathbf{K})}_{\mathbf{K}'}x_{t+1}=\underbrace{\mathbf{F}_{t+1}+\mathbf{M}[a_0x_t+a_2\dot{x}_t+a_3\ddot{x}_t]+\mathbf{C}[a_1\dot{x}_t+a_4\dot{x}_t+a_5\ddot{x}_t]}_{\mathbf{F}'_{t+1}}$$

Finally, the direct integration method can be expressed as

$$\mathbf{K}'x_{t+1}=\mathbf{F}'_{t+1} \tag{3.11}$$

Two-dimensional case

At preliminary phase, this project involves two-dimensional work. In the two-dimensional case, the method is simplified such that the total force and total torque are assumed to be zero (Stokes flow), therefore the Navier-Stokes reduce to

$$-\nabla P + \nabla^2 \mathbf{u} = 0, \tag{3.12}$$

$$\nabla \bullet \mathbf{u} = 0, \ \mathbf{F} = 0 \tag{3.13}$$

Ding & Aidun (2004) investigate a new LB technique by conditioning the relaxation time (τ=1 in this case) in the lattice Boltzmann equation for Stokes flow. The method is so-called Stokesian Lattice Boltzmann Method (SLBE). The lattice equation is simplified to

$$f_{\sigma i}(\mathbf{x} + \mathbf{e}_{\sigma i}, t+1) = f_{\sigma i}^{(0)}(\mathbf{x}, t), \tag{3.14}$$

$$f_{\sigma i}^{(0)} = \rho[A_\sigma + B_\sigma(\mathbf{e}_{\sigma i} \cdot \mathbf{u})] \tag{3.15}$$

The method is accurate and computationally efficient. The forces along a link σi where connecting a boundary node of the solid particles and one of its adjacent fluid nodes is calculated as

$$F_{\sigma i} = -2 f_{\sigma i} + 6\rho w_{\sigma i} \mathbf{u}_{\sigma i} \bullet \mathbf{e}_{\sigma i}, \tag{3. 16}$$

where $w_{\sigma i}$ is the weighing factor for the particle at equilibrium, and

$$\mathbf{u}_{\sigma i} = \mathbf{U} + \Omega \times (\mathbf{R} - \tfrac{1}{2}\mathbf{e}_{\sigma i}) \tag{3.17}$$

The total force and torque on a solid particle is calculated by taking the summation over all links:

$$\mathbf{F} = \sum_{\sigma i} F_{\sigma i}\mathbf{e}_{\sigma i}\ , \quad \mathbf{T} = \sum_{\sigma i} F_{\sigma i}(\mathbf{R}\times\mathbf{e}_{\sigma i}) \tag{3.18}$$

Particle velocity and orientation are calculated from the conditions of force-free and torque-free, therefore the calculation force becomes (Ding & Aidun, 2004)

$$\mathbf{G} = \mathbf{P} + \mathbf{W}\bullet\mathbf{V} + \mathbf{G_0}\ , \tag{3.19}$$

$$\tau_{\sigma i} = \begin{pmatrix}\mathbf{e}_{\sigma i}\\ w_{\sigma i}\end{pmatrix},\ w_{\sigma i} = R\times e_{\sigma i},\ \mathbf{V} = \begin{pmatrix}\mathbf{U}\\ \Omega\end{pmatrix},\ \mathbf{G} = \begin{pmatrix}\mathbf{F}\\ \mathbf{T}\end{pmatrix}, \tag{3.20}$$

$$\mathbf{P} = \sum(-2f_{\sigma i})\tau_{\sigma i},\quad \mathbf{W} = \sum\ 6\ \rho\ w_{\sigma i}\ \tau_{\sigma i}\ \tau_{\sigma i}\ , \tag{3.21}$$

where **P** is the force when the particle at rest, **W.V** is the force by motion of particle, $\mathbf{G_0}$ is the external force, **G** is the total force and total torque such that equal to zero, **U** is the particle velocity vector, Ω is the particle orientation, **R** is the radius of solid particle and **W** is a 3 x 3 matrix in two-dimensional case and 6 x 6 matrix in three-dimensional case respectively.

Translation and rotation of the solid particle are calculated based on the particle velocity and orientation

$$\begin{bmatrix} x_0\\ y_0\\ a_{z0}\end{bmatrix} = \begin{bmatrix} x_{0i}\\ y_{0i}\\ a_{z0i}\end{bmatrix} + \begin{bmatrix} U_x\ \Delta t\\ U_y\ \Delta t\\ \Omega\ \ \Delta t\end{bmatrix}, \tag{3.22}$$

where x_0, y_0 and a_{z0} are the position and orientation of the particle center; x_{0i}, y_{0i} and a_{z0i} are the prior position and orientation of the particle center.

Two-dimensional case fluid-solid coupling

In the deformation phase, the finite element (FE) and lattice Boltzmann (LB) methods are coupled. The deformation of a solid particle is calculated by using the FE method. The fluid flow that causes a solid particle to deform is determined by the LB method.

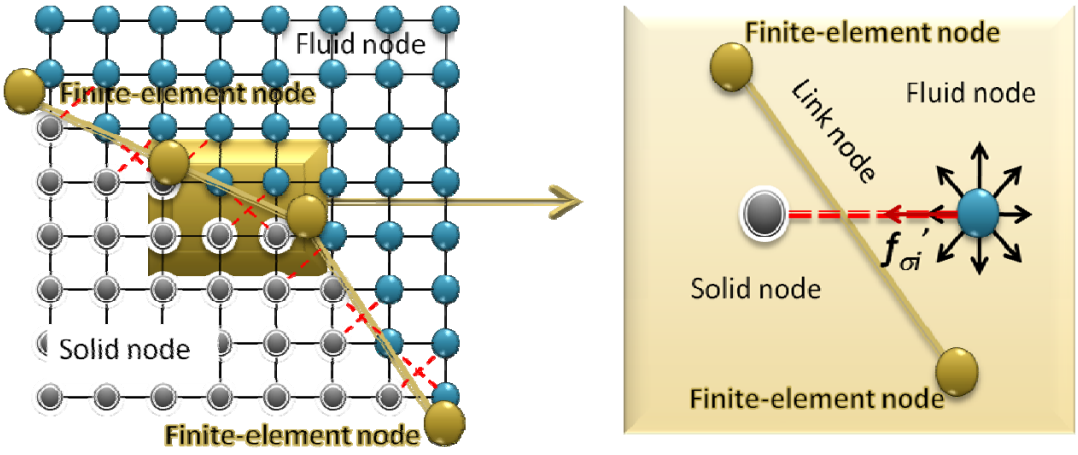

Figure 3.4: Intersection and interpolation of the coupling method.

As seen in figure 3.4, the coupling process occurs through intersection and interpolation. Lattice nodes on the side and right side of a solid surface line are depicted as solid lattice nodes ( ) and fluid nodes ( ). The boundary surface divides some of the LB links such that they cross from solid to fluid lattice nodes. The fluid causes a

force via bounce-back boundary condition at a discrete location on the finite element mesh and this force is linearly interpolated to the finite element nodes.

Force on each FE surface node is

$$F_{x\_jj} = \sum_{ii} (1 - k_d)\, F_{x\_ii}\ ,\ F_{x\_jj+1} = \sum_{ii} k_d\ F_{x\_ii}\ , \tag{3.23}$$

$$F_{y\_jj} = \sum_{ii} (1 - k_d)\, F_{y\_ii}\ ,\ F_{y\_jj+1} = \sum_{ii} k_d\ F_{y\_ii}\ , \tag{3.24}$$

where *ii* is the number of links, *jj* is the number of FE surface nodes, F_{x_ii} and F_{y_ii} are the force link estimations.

The last step for calculating the deformation for solid particles is to perform a matrix calculation of the global stiffness matrix as a matrix inversion and forces. In this case, the static finite element is used to simplify the preliminary study.

$$\mathbf{K}_{(3+n)n}\ \mathbf{x}_n = \mathbf{F}_{(3+n)n}\ , \tag{3.25}$$

where **F** is the FE surface forces (F_{x_jj}, F_{y_jj}), **K** is the global stiffness matrix, *n* is the matrix dimension and $\mathbf{x}$ is the displacement for each FE surface node. Previously, the constraints had been added to the global stiffness matrix, and the equations became overdetermined. To avoid this condition, the global stiffness matrix is converted into a transposed global stiffness matrix and equation is given by

$$\underbrace{\mathbf{K}^{T}{}_{(3+n)n}\ \ \mathbf{K}_{(3+n)n}\ \mathbf{x}_n}_{\mathbf{K}'} = \underbrace{\mathbf{K}^{T}{}_{(3+n)n}\ \mathbf{F}_{(3+n)n}}_{\mathbf{F}'}\ ,$$

$$\mathbf{K}'\mathbf{x}_n = \mathbf{F}' \tag{3.26}$$

Direct methods (matrix inversion and gauss elimination) are used to solve these linear simultaneous equations. Matrix inversion is preferred because the global stiffness is not updated every time step in simulation (it is determined only once in a simulation). Conversely, Gauss elimination on the global stiffness matrix should be renewed for every lattice Boltzmann time steps.

Reference coordinates for two-dimensional case

In the finite element method, both local and global (or reference) coordinates are applied. Local coordinates are always chosen to conveniently represent the individual element, and global coordinates are chosen to be convenient for the whole structure. Example coordinates are shown in figure 3.5 for global coordinate (X, Y) and local coordinate (x, y).

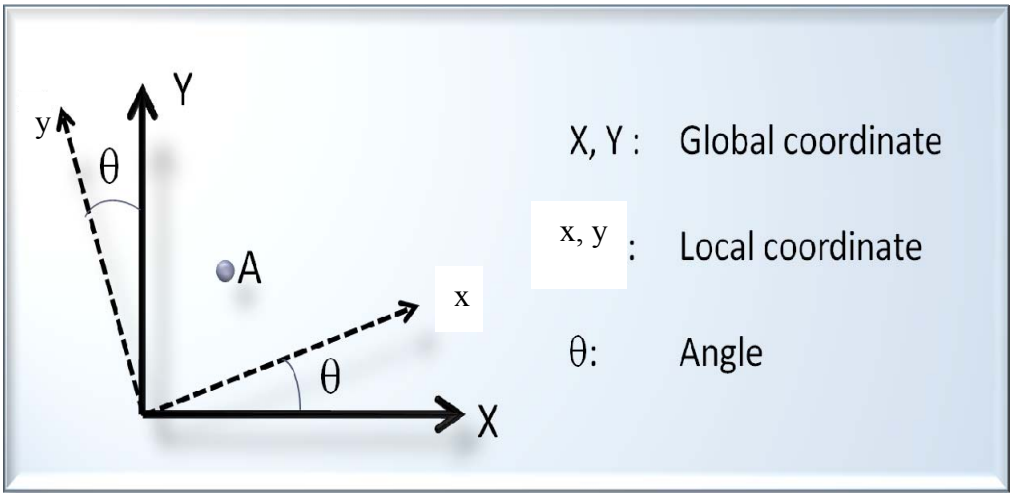

Figure 3.5: Transformation coordinates for two-dimensional case

Hence, rotation of coordinate system from local to global is expressed as

$$\begin{pmatrix} X \\ Y \end{pmatrix} = \begin{pmatrix} \cos\theta & -\sin\theta \\ \sin\theta & \cos\theta \end{pmatrix} \begin{pmatrix} x \\ y \end{pmatrix}, \tag{3.27}$$

and rotation of coordinate system from global to local is expressed as

$$\begin{pmatrix} x \\ y \end{pmatrix} = \begin{pmatrix} \cos\theta & \sin\theta \\ -\sin\theta & \cos\theta \end{pmatrix} \begin{pmatrix} X \\ Y \end{pmatrix} \tag{3.28}$$

Application in two-dimensional case: an elliptical cylinder in a simple shear flow

In order to evaluate the coupling method, two elliptical cylinders with aspect ratio 2:1 and 5:1 are presented and compared to the theoretical result (Jeffery's theory). The theoretical assumption is given by Jeffery (1922) to determine the particle orientation is shown as

$$\varphi = \tan^{-1}\left(\frac{b}{c}\tan\left(\frac{dcGt}{b^2 + c^2}\right)\right), \tag{3.29}$$

where φ is the particle orientation, G is the shear rate, t is the lattice Boltzmann time, b is the major axis, c is the minor axis, ly is the domain height, and lx is the simulation domain length.

The first example shows two elliptical cylinders of varying elasticity in simple shear flow with aspect ratio 2:1. The simulation conditions are the following

- Each particle is set at the center of domain which is similar to Jeffery's model;
- the ratio of computational domain to each particle diameter is set much larger than 1 in order to neglect the wall effect, ly/d = 12, lx/d = 12;

- the particle behaves like rigid or near rigid (Young's modulus number, E is 100) and flexible fiber (Young's modulus number is about 3).

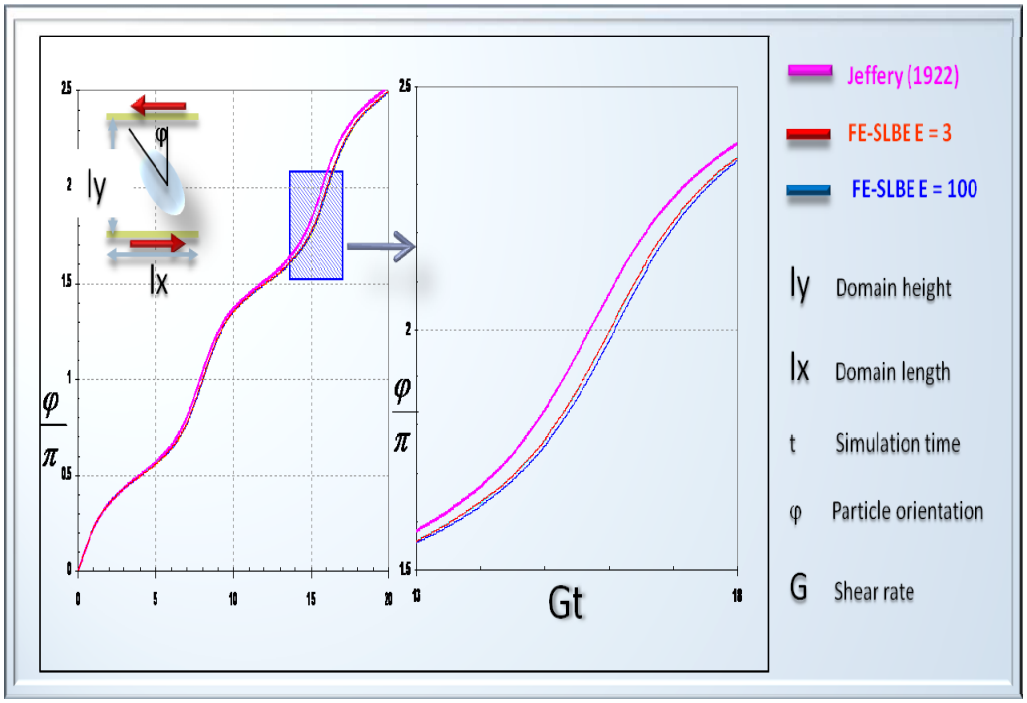

Figure 3.6: An elliptical cylinder with a 2:1 aspect ratio in a simple shear flow (Rezak, 2005)

Figure 3.6 shows the results of the simulation where the y-axis represents particle orientation, and the x-axis represents non-dimensional time. The near rigid particle is denoted by blue solid line, the flexible particle is denoted by red solid line, and the theoretical result is denoted by the pink solid line. The results show that the near rigid particle (FE-SLBE with high Young's modulus number, E is100) is close to the analytical result. Hence, the method gives an accurate result for this condition. As the flexibility increases (FE-SLBE with low Young's modulus number, E is 3), the particle is rotating faster than the near rigid one. However, there is fluctuation of the particle surface when

the flexibility of a particle increases, which can cause an oscillation of its aspect ratio as shown in figure 3.7. If this fluctuation grew, the system can become unstable. This is one limitation of the current method that should be solved.

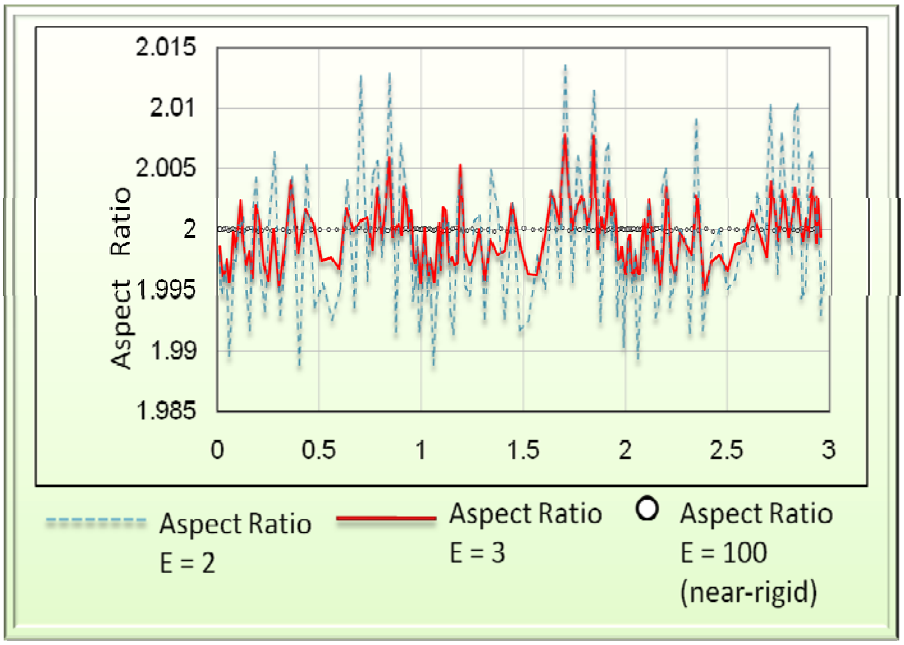

Figure 3.7: Fluctuation due to different Young's modulus for aspect ratio 2:1

The Second example is an elliptical cylinder in a simple shear flow with a 5:1 aspect ratio.

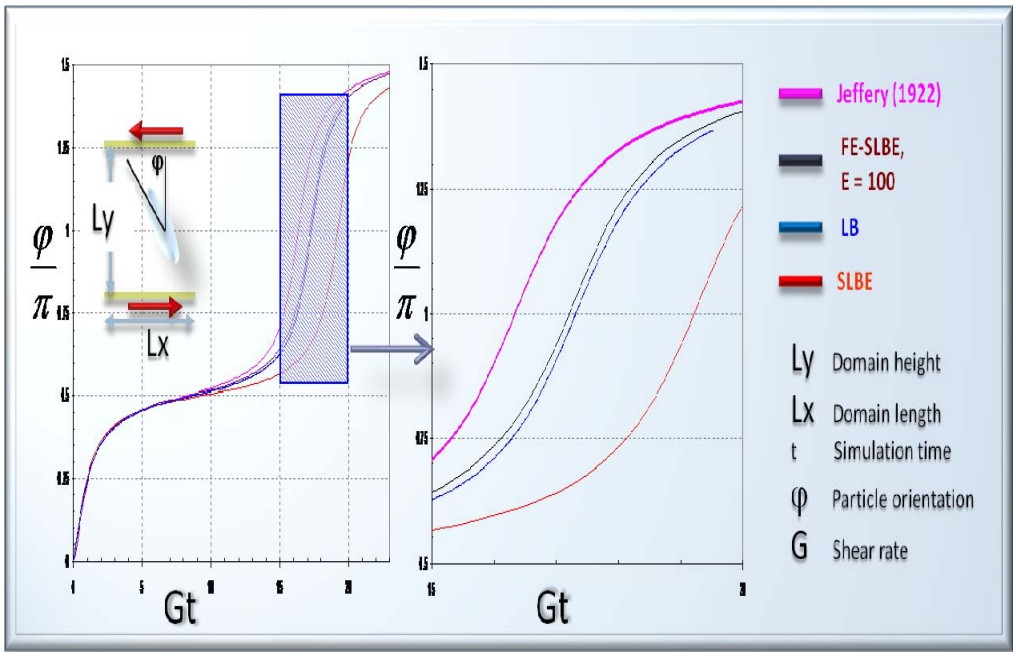

Figure 3.8: An ellipse cylinder aspect ratio 5:1 in simple shear flow

For the second example, the simulation conditions are similar to the particle aspect ratio 2:1. The finite element-Stokesian lattice Boltzmann method (FE-SLBE) for near rigid particle is compared to rigid particle using the LB method (general lattice Boltzmann method). Figure 3.8 depicts the results of simulation with the near rigid particle (FE-SLBE) with an aspect ratio of 5:1 is denoted by the brown solid line, the flexible particle (FE-SLBE) with an aspect ratio of 5:1 is denoted by the red solid line, the theoretical result (Jeffery's theory) is denoted by the pink solid line, and the rigid particle (LB) is denoted by the blue solid line.

Figure 3.8 shows the orientation of the particle versus the non-dimensional time. The near rigid and flexible particles using lattice Boltzmann technique with Stokes flow

modification (FE-SLBE) has shown a numerical inaccuracy for aspect ratio 5:1. This inaccuracy is caused by a long residence time at the horizontal orientation, which causes sensitivity in the period of rotation.

Therefore, to reduce the fluctuation found in higher aspect ratio particles, the coupling method needs to be modified by integrating the damping and mass factors into the finite element equation and applying the general lattice Boltzmann method. These modifications have been developed for three dimensional case.

Three-dimensional case

Finite element three-dimensional case: tetrahedral solid element

Tetrahedral linear-elastic solid elements are used to model a solid flexible fiber in this study. The three-dimensional solid fiber is discretized into many tetrahedrons, which can be seen in figure 3.9.

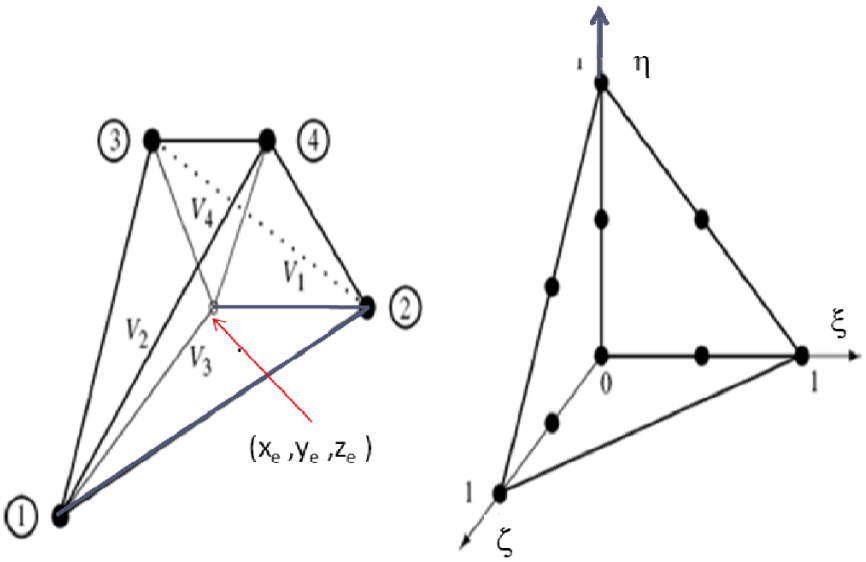

Figure 3.9a: Volume and natural coordinates for a tetrahedron

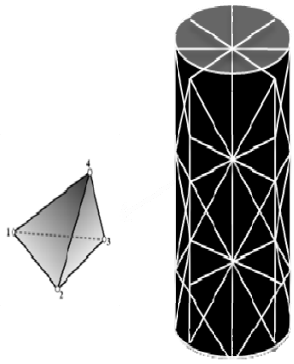

Figure 3.10b: a fiber model consists of tetrahedrons.

One of these tetrahedrons divided into four volumes where the common point is at (x_e, y_e, z_e) as shown in figure 3.9. The shape function equation of a tetrahedron or the position of the point (x_e, y_e, z_e) in the tetrahedron can be written as (Zienkiewicz, *et al.* 2000; Logan, 1986)

$$\begin{Bmatrix} 1 \\ x_e \\ y_e \\ z_e \end{Bmatrix} = \begin{bmatrix} 1 & 1 & 1 & 1 \\ x_1 & x_2 & x_3 & x_4 \\ y_1 & y_2 & y_3 & y_4 \\ z_1 & z_2 & z_3 & z_4 \end{bmatrix} \begin{Bmatrix} h_1 \\ h_2 \\ h_3 \\ h_4 \end{Bmatrix}, \tag{3.30}$$

where V is the tetrahedron volume and h_1, h_2, h_3, h_4 are

$$h_1 = V_1/V,\ h_2 = V_2/V,\ h_1 = V_3/V,\ h_4 = V_4/V,\quad h_i = h_i(x_e, y_e, z_e), \tag{3.31}$$

$$h_1 + h_2 + h_3 + h_4 = 1 \tag{3.32}$$

In order for the four coordinate $\{h_1,\ h_2,\ h_3,\ h_4\}$ to describe the three coordinates (x_e, y_e, z_e), it must be supplemented by a constraint (equation 3.33) and using natural coordinates in figure 3.9, this constraint can be given as

$$h_1 = \xi,\ \ h_2 = \eta,\ \ h_3 = \zeta, \qquad h_4 = 1 - \xi - \eta - \zeta\ , \tag{3.33}$$

These are volumes in (ξ, η, ζ) space. A typical function is given by

$$x\ (x_e, y_e, z_e) = \sum_i^4 h_i(\xi, \eta, \zeta)\ x_i\ , \tag{3.34}$$

where u_i are the nodal values of the function and x, y, z coordinate become

$$\begin{aligned} x_e &= x_1 h_1 + x_2 h_2 + x_3 h_3 + x_4 h_4 = x_4 + x_{14}\xi + x_{24}\eta + x_{34}\zeta, \\ y_e &= y_1 h_1 + y_2 h_2 + y_3 h_3 + y_4 h_4 = y_4 + y_{14}\xi + y_{24}\eta + y_{34}\zeta, \\ z_e &= z_1 h_1 + z_2 h_2 + z_3 h_3 + z_4 h_4 = z_4 + z_{14}\xi + z_{24}\eta + z_{34}\zeta, \end{aligned} \tag{3.35}$$

where $x_{14} = x_1 - x_4$, and so on. The strains are obtained in terms of derivatives of elemental displacements. Using the natural coordinate system, the derivatives are given as

$$\begin{aligned} \frac{\partial}{\partial x_e} &= \frac{\partial}{\partial \xi}\frac{\partial \xi}{\partial x_e} + \frac{\partial}{\partial \eta}\frac{\partial \eta}{\partial x_e} + \frac{\partial}{\partial \zeta}\frac{\partial \zeta}{\partial x_e} \\ \frac{\partial}{\partial y_e} &= \frac{\partial}{\partial \xi}\frac{\partial \xi}{\partial y_e} + \frac{\partial}{\partial \eta}\frac{\partial \eta}{\partial y_e} + \frac{\partial}{\partial \zeta}\frac{\partial \zeta}{\partial y_e} \\ \frac{\partial}{\partial z_e} &= \frac{\partial}{\partial \xi}\frac{\partial \xi}{\partial z_e} + \frac{\partial}{\partial \eta}\frac{\partial \eta}{\partial z_e} + \frac{\partial}{\partial \zeta}\frac{\partial \zeta}{\partial z_e} \end{aligned} \rightarrow \begin{Bmatrix} \frac{\partial}{\partial \xi} \\ \frac{\partial}{\partial \eta} \\ \frac{\partial}{\partial \zeta} \end{Bmatrix} = \begin{bmatrix} \frac{\partial x_e}{\partial \xi} & \frac{\partial y_e}{\partial \xi} & \frac{\partial z_e}{\partial \xi} \\ \frac{\partial x_e}{\partial \eta} & \frac{\partial y_e}{\partial \eta} & \frac{\partial z_e}{\partial \eta} \\ \frac{\partial x_e}{\partial \zeta} & \frac{\partial y_e}{\partial \zeta} & \frac{\partial z_e}{\partial \zeta} \end{bmatrix} \begin{Bmatrix} \frac{\partial}{\partial x_e} \\ \frac{\partial}{\partial y_e} \\ \frac{\partial}{\partial z_e} \end{Bmatrix} \quad \textbf{or} \quad \left\{\frac{\partial}{\partial \xi}\right\} = [J]\left\{\frac{\partial}{\partial x_e}\right\}, \tag{3.36}$$

where $[J]$ is called the Jacobian operator relating the natural coordinates to the local coordinates and having the explicit form

$$[J] = \begin{bmatrix} x_{14} & y_{14} & z_{14} \\ x_{24} & y_{24} & z_{24} \\ x_{34} & y_{34} & z_{34} \end{bmatrix}, \tag{3.37}$$

The inverse is given by

$$[J^{-1}] = \frac{1}{\det[J]} \begin{bmatrix} y_{24}z_{34} - y_{34}z_{24} & y_{34}z_{14} - y_{14}z_{34} & y_{14}z_{24} - y_{24}z_{14} \\ z_{24}x_{34} - z_{34}x_{24} & z_{34}x_{14} - z_{14}x_{34} & z_{14}x_{24} - z_{24}x_{14} \\ x_{24}y_{34} - x_{34}y_{24} & x_{34}y_{14} - x_{14}y_{34} & x_{14}y_{24} - x_{24}y_{14} \end{bmatrix} = [A], \tag{3.38}$$

where

$$\det[J] = x_{14}[y_{24}z_{34} - y_{34}z_{24}] + y_{14}[z_{24}x_{34} - z_{34}x_{24}] + z_{14}[x_{24}y_{34} - x_{34}y_{24}]$$

The determinant of Jacobian is related to the volume of the tetrahedron. Note that $[J]$ and its inverse are constants related to the coordinate of the tetrahedron. Therefore, for Stiffness matrix is given as (Bath, 1982)

$$\mathbf{K} = \int \mathbf{B}^T \, \mathbf{D} \, \mathbf{B} \, d\mathbf{V}, \tag{3.39}$$

where **B** is the displacement matrix,

$$\mathbf{D} = \begin{bmatrix} E^{-1} & -\upsilon E^{-1} & -\upsilon E^{-1} & 0 & 0 & 0 \\ -\upsilon E^{-1} & E^{-1} & -\upsilon E^{-1} & 0 & 0 & 0 \\ -\upsilon E^{-1} & -\upsilon E^{-1} & E^{-1} & 0 & 0 & 0 \\ 0 & 0 & 0 & G_s^{-1} & 0 & 0 \\ 0 & 0 & 0 & 0 & G_s^{-1} & 0 \\ 0 & 0 & 0 & 0 & 0 & G_s^{-1} \end{bmatrix} = \text{elasticity matrix}$$

$$G_s = \frac{E}{2(1+\upsilon_p)} = \text{shear modulus}$$

υ_p is the Poisson ratio, E is the Young's Modulus.

The matrix **M** is the mass matrix of the structure, which is given as

$$\mathbf{M} = \int \rho \ \mathbf{H}^{\mathbf{T}} \ \mathbf{H} \ d\mathbf{V}, \tag{3.40}$$

$$x(x_e, y_e, z_e) = \mathbf{H}(x_e, y_e, z_e) \ X,$$

where **H** is the displacement interpolation matrix or the shape function, $x(x_e, y_e, z_e)$ is the displacements measured in a local coordinate system within each element and X is a vector of the three global displacements at all nodal points.

The Rayleigh damping matrix **C** is proportional to the mass matrix on an element level, therefore

$$\mathbf{C} = \gamma \mathbf{M} + \beta \mathbf{K}, \tag{3.41}$$

where γ and β are constants chosen to dampen the high frequency modes. Since this study is using Newmark method for solving dynamic-finite element, there are several

conditions to choose the damping constants. For damping analysis, Newmark model is conditionally stable (linear acceleration method) if

$$\gamma \geq \frac{1}{2}, \quad \beta \leq \frac{1}{2} \text{ and } \quad \Delta t \leq \frac{1}{\omega_{MAX}\sqrt{\gamma/2 - \beta}} \quad , \tag{3.42}$$

where ω_{MAX} is the maximum frequency in the structural system (i.e., $\gamma = 1/2$, $\beta = 1/6$). Newmark's method is unconditionally stable (average acceleration method) if

$$2\beta \geq \gamma \geq \frac{1}{2} \quad , \tag{3.43}$$

(i.e., $\gamma = 1/2$, $\beta = 1/4$). However if γ is less than $\frac{1}{2}$, errors are introduced because of the negative damping result and the analysis becomes unstable.

Particle rotation for three-dimensional case

All finite element calculations are done in a body fixed coordinate system, which combined with the assumption of small deformations, results in the finite element matrices being invariant. Therefore, the local on body fixed coordinate is fixed on the particle center of mass and oriented using the average angular displacement of the finite element nodes. By integrating the Eularian angular velocity, the Eularian angle is then determined.

Reference coordinate (three-dimensional case)

In three-dimensional case, the eulerian angle transformation is used to transform fibers coordinate. The euler angles (φ,θ,ψ) and corresponding rotation matrices are given as

A rotation about z-axis (φ)

$$R_Z(\varphi) = \begin{bmatrix} \cos\varphi & \sin\varphi & 0 \\ -\sin\varphi & \cos\varphi & 0 \\ 0 & 0 & 1 \end{bmatrix}, \tag{3.44}$$

A rotation about x'-axis (θ)

$$R_X'(\theta) = \begin{bmatrix} 1 & 0 & 0 \\ 0 & \cos\theta & \sin\theta \\ 0 & -\sin\theta & \cos\theta \end{bmatrix}, \tag{3.45}$$

A rotation about z"-axis (ψ)

$$R_Z''(\psi) = \begin{bmatrix} \cos\psi & \sin\psi & 0 \\ -\sin\psi & \cos\psi & 0 \\ 0 & 0 & 1 \end{bmatrix}, \tag{3.46}$$

Therefore, the the sequence of rotations is concatenated as follows

$$R_{ZX'Z''}(\varphi,\theta,\psi) = R_z(\varphi)R_x'(\theta)R_z''(\psi), \tag{3.47}$$

$$R_{ZX'Z''}(\varphi,\theta,\psi) = \begin{bmatrix} \cos\varphi & \sin\varphi & 0 \\ -\sin\varphi & \cos\varphi & 0 \\ 0 & 0 & 1 \end{bmatrix}\begin{bmatrix} 1 & 0 & 0 \\ 0 & \cos\theta & \sin\theta \\ 0 & -\sin\theta & \cos\theta \end{bmatrix}\begin{bmatrix} \cos\psi & \sin\psi & 0 \\ -\sin\psi & \cos\psi & 0 \\ 0 & 0 & 1 \end{bmatrix}$$

Hence the coordinate transformation from local to global

$$\begin{bmatrix} X \\ Y \\ Z \end{bmatrix} = R^{T}_{ZX\,'Z''}(\varphi, \theta, \psi) \begin{bmatrix} x \\ y \\ z \end{bmatrix}, \tag{3.48}$$

The coordinate transformation from global to local

$$\begin{bmatrix} x \\ y \\ z \end{bmatrix} = R_{ZX\,'Z''}(\varphi, \theta, \psi) \begin{bmatrix} X \\ Y \\ Z \end{bmatrix}, \tag{3.49}$$

where X, Y, Z are the global coordinates, x, y, z are the local coordinates, and the inverse of a rotation matrix is equal to its transpose, consequently $R^{-1} = R^{T}$.

Three-dimensional case fluid-solid coupling

The coupling process occurs through intersection and interpolation similar to the two dimensional case. A deformation of a solid particle is calculated by using the FE method. The fluid flow that causes a solid particle to deform is determined by the LB method. For 3-Dimensional case, lattice links on each finite element surface are obtained using a Raytracing method which is a common method for rendering three-dimensional computer graphics.

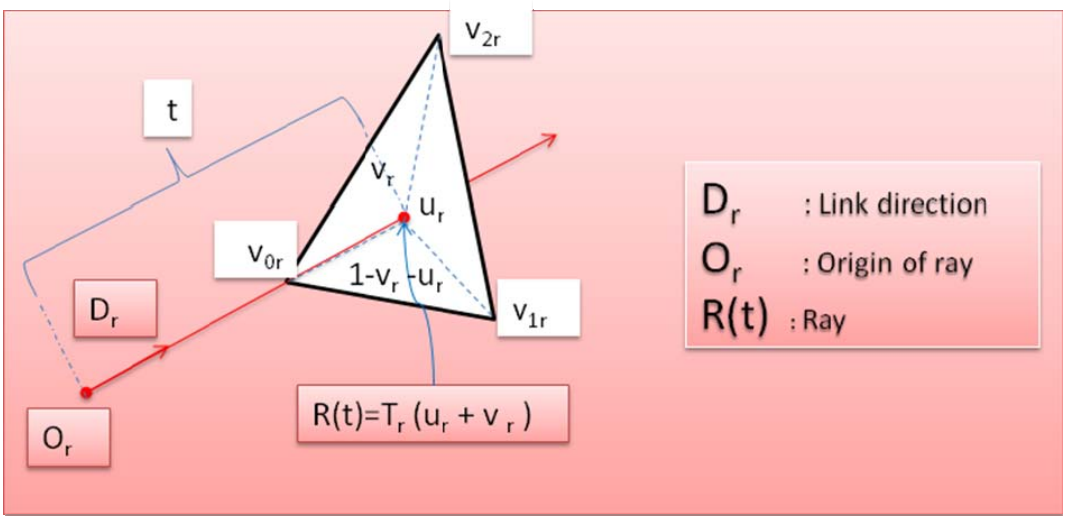

Figure 3.11: Ray-Triangle Intersection method

In this method, lattice links are represented as rays which are projected along the lattice directions and intersections with the triangle finite element solid surfaces are determined using a fast, minimum storage ray-triangle intersection method (Moller & Trumbore, 1997). The intersection algorithm explains the origin of the ray (O_r) with link direction (D_r), and then changes the base of that vector which yields a vector $(t_r\ u_r\ v_r)^T$, where t_r is the distance to the plane in which the triangle lies and (u_r, v_r) represents the barycentric coordinates inside the triangle. A point $T_r(u_r, v_r)$ on a triangle is given by

$$\mathsf{T}_r(u_r, v_r) = (1 - u_r - v_r)\mathsf{V}_{0r} + u_r\mathsf{V}_{1r} + v_r\mathsf{V}_{2r}, \qquad (3.50)$$

where (u_r, v_r) are the barycentric coordinate or intersection on triangle in barycentric coordinate, which are constraint such that $u_r, v_r \geq 0$ and $u_r + v_r \leq 1$. Computing the

intersection between the ray, R(t) and the triangle, $T_r(u_r, v_r)$, is equivalent to $R(t) = T_r(u_r, v_r)$, which yields

$$O_r + t_r D_r = (1 - u_r - v_r)V_{0r} + u_r V_{1r} + v_r V_{2r} \quad \rightarrow$$

$$\begin{bmatrix} -D_r & V_{1r} - V_{0r} & V_{2r} - V_{0r} \end{bmatrix} \begin{bmatrix} t_r \\ u_r \\ v_r \end{bmatrix} = O_r - V_{0r}, \tag{3.51}$$

Denoting $E_{1r} = V_{1r} - V_{0r}$, $E_{2r} = V_{2r} - V_{0r}$ and $T_r = O_r - V_{0r}$, the solution is obtained

$$\begin{bmatrix} t_r \\ u_r \\ v_r \end{bmatrix} = \frac{1}{(D_r \times E_{2r}) \cdot E_{1r}} \begin{bmatrix} (T_r \times E_{1r}) \cdot E_{2r} \\ (D_r \times E_{2r}) \cdot T_r \\ (T \times E_{1r}) \cdot D_r \end{bmatrix} \tag{3.52}$$

The no-slip bounce-back scheme is generally applied for boundary conditions, where the momentum from the incoming particle is bounced back in the opposite direction after the particle hits the wall. The boundary condition assumes the wall is located halfway between nodes (Ladd & Verberg, 2001). For a moving boundary is described as (Aidun *et al.*, 1998)

$$F_{\sigma i}^{(b)}(\mathbf{x} + \tfrac{1}{2}\mathbf{e}_{\sigma i}, t + \tfrac{1}{2}) = 2\mathbf{e}_{\sigma i'}\left[f_{\sigma i}(\mathbf{x}, t+1) - \rho(\mathbf{x}, t+1)\mathbf{B}_{\sigma}\mathbf{u}_b \bullet \mathbf{e}_{\sigma i'}\right] \tag{3.53}$$

where $F_{\sigma i}^{(b)}$ is the force exerted on the particle for any lattice link, σi is the lattice link direction, σi' is the lattice link with direction opposite to that of link σi. The boundary

velocity, $\mathbf{u}_{b,}$ is determined by linear interpolation from the finite element nodal velocity on the surface intersected by the link. The particle-distribution function ($f_{\sigma i}$) can be seen in equation 3.1.

Resolving the solid boundary requires overlying the unstructured finite element mesh on the structured LB lattice. As seen in figure 3.4, the intersections of the lattice direction vectors with the solid mesh define the boundary location. Lattice nodes on the interior of the solid are depicted as solid lattice nodes, lattice nodes on the exterior of the solid depicted as fluid nodes. Fluid particles traveling from fluid lattice nodes to solid lattice nodes are bounced using equation (3.53), and the boundary force is linearly interpolated to the nearest finite element nodes.

Fiber-fiber in contact

In order to prevent fibers from penetrating each other, contact must be detected and an appropriate contact force applied. The contact force exerted on segment fiber-I can be found as

$$F_{cI} = -\varsigma \exp[-h_{IJ}.^{d}\!/_{2}]\,\mathbf{n}_{IJ}\ , \tag{3.54}$$

where ς is the magnitude of contact force constant, h_{IJ} is the minimum gap between fiber-I and fiber-J, d is the fiber diameter, and $\mathbf{n}_{IJ}$ is the normal unit vector between segment at the point of minimum separation directed from I to J. To calculate the minimum gap, a fiber is divided into several segments as shown in figure 3.11.

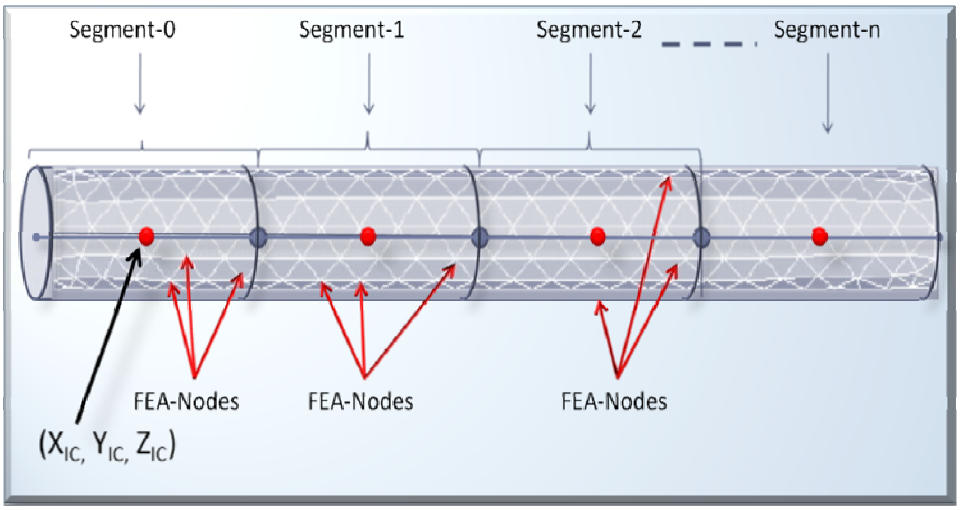

Figure 3.12: Segmentation of a fiber for solving fiber-fiber contact

After that, a minimum separation distance between fibers, g_{IJ} is obtained by calculating the closest distance between segments of fiber-I and fiber fiber-J (figure 3.12). Gap minimum, h_{IJ} is found by subtracting the minimum separation distance (g_{IJ}) by fiber diameter (d).

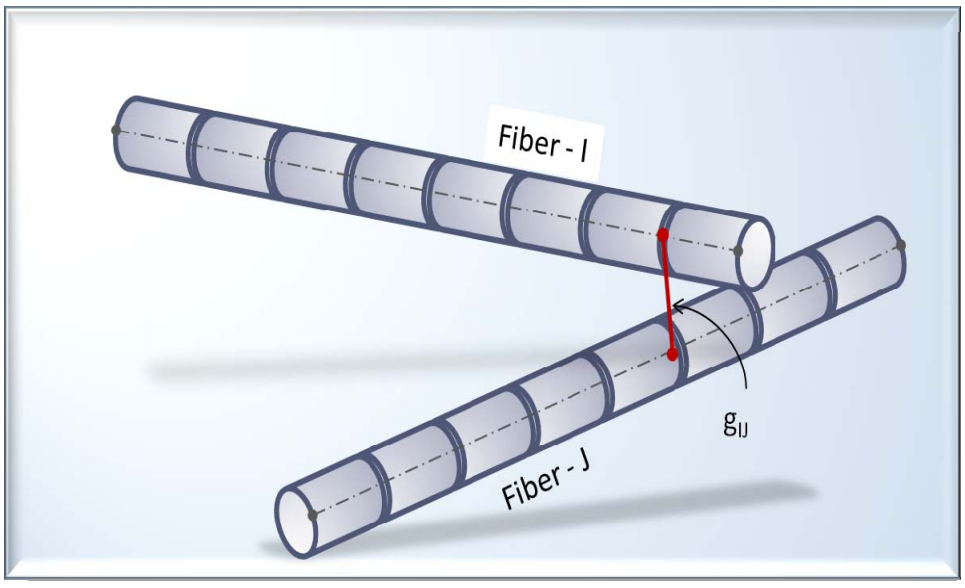

Figure 3.13: Interaction between fiber segments I and J

Once contact point and contact force are known, the contact force is distributed to finite element nodes by finding the closest nodes from the contact point and its adjacent surfaces.

Algorithm for fiber-fiber contact can be explained; first a fiber is constructed as a rod cylinder and divided into segments. Each segment has its center of mass, which is calculated by averaging the finite element nodes of a segment.

$$X_{IC} = \frac{\sum_{nI} X_I}{nI}, \quad Y_{IC} = \frac{\sum_{nI} Y_I}{nI}, \quad Z_{IC} = \frac{\sum_{nI} Z_I}{nI}, \tag{3.55}$$

where X_{Ic}, Y_{Ic}, Z_{Ic} are the center of mass each segment of fiber-I, X_I, Y_I, Z_I are the finite element node position of fiber-I, nI denotes the total number of finite element nodes per segment.

Second, the minimum separation distance between particle-particle and particle-wall is determined for different boundary conditions (no-slip and periodic boundary conditions), and the schematic is illustrated in figure 3.13. To obtain a minimum separation distance between particles or fibers, the position of a fiber (Fiber-I or Fiber-J) in simulation domain is calculated. It is necessary to account for periodic boundary conditions (Table 10, table 11, table 12, table 13).

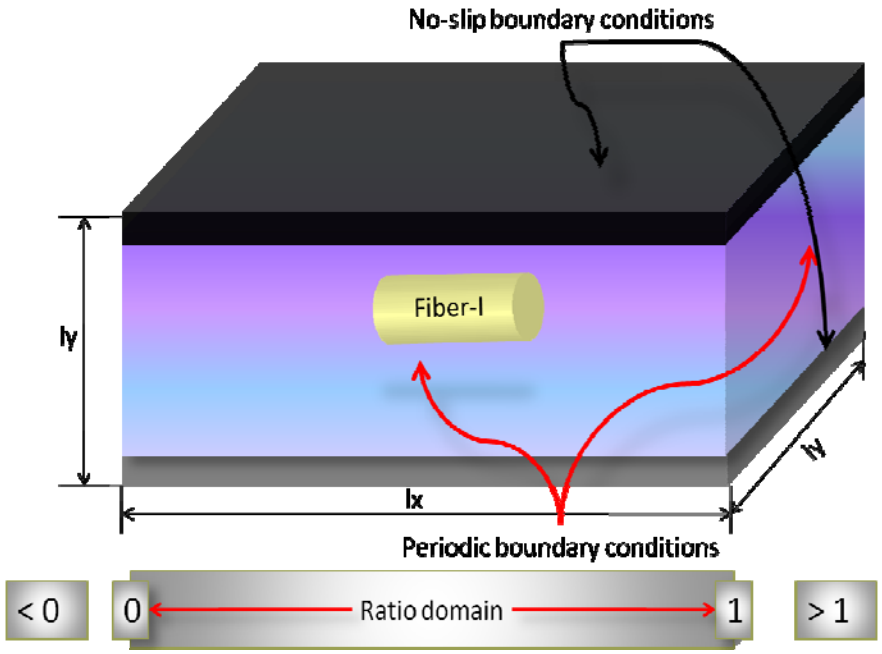

Figure 3.14: Schematic of a fiber in a rectangular channel with periodic boundary conditions in x and z directions, and no-slip boundary conditions on top and bottom domain walls.

Table 10: Case for fiber-I (x direction)

Case	Ratio Domain	In-domain	Range Ratio Domain
Case I: X_{IC} > lx	$\frac{X_{IC}}{lx}$	$X_{IC} = X_{IC} - Ratio\ domain*lx$	**> 1.0**
Case II: X_{IC} < lx	$-\frac{X_{IC}}{lx}$	$X_{IC} = X_{IC} + (Ratio\ domain+1)*lx$	**< 0.0**
Case III: 0≤ X_{IC} ≤ lx	**0**	$X_{IC} = X_{IC}$	**0.0 – 1.0**

Table 11: Case for fiber-J (x direction)

Case	Ratio Domain	In-domain	Range Ratio Domain
Case I: X_{JC} > lx	$\frac{X_{JC}}{lx}$	$X_{JC} = X_{JC} - Ratio\ domain*lx$	**> 1.0**
Case II: X_{JC} < 0	$-\frac{X_{JC}}{lx}$	$X_{JC} = X_{JC} + (Ratio\ domain+1)*lx$	**< 0.0**
Case III: 0 ≤X_{JC} ≤ lx	**0**	$X_{JC} = X_{JC}$	**0.0 – 1.0**

Table 12: Case for fiber-I (z direction)

Case	Ratio Domain	In-domain	Range Ratio Domain
Case I: Z_{IC} > lz	$\frac{Z_{IC}}{lz}$	$Z_{IC} = Z_{IC} - Ratio\ domain*lz$	**> 1.0**
Case II: Z_{IC} < 0	$-\frac{Z_{IC}}{lz}$	$Z_{IC} = Z_{IC} + (Ratio\ domain+1)*lz$	**< 0.0**
Case III: 0≤ Z_{IC} ≤ lz	**0**	$Z_{IC} = Z_{IC}$	**0.0 – 1.0**

Table 13: Case for fiber-J (z direction)

Case	Ratio Domain	In-domain	Range Ratio Domain
Case I: Z_{JC} > lz	$\frac{Z_{JC}}{lz}$	$Z_{JC} - Ratio\ domain*lz$	**> 1.0**
Case II: Z_{JC} < 0	$-\frac{Z_{JC}}{lz}$	$Z_{JC} = Z_{JC} + (Ratio\ domain+1)*lz$	**< 0.0**
Case III: 0≤ Z_{JC} ≤ lz	**0**	$Z_{JC} = Z_{JC}$	**0.0 – 1.0**

Figure 3.14 illustrates the calculation of minimum distance between fiber-I and fiber-J and highlights the need to account for domain periodicity. Fiber-I is located at x_1 from the origin, and since the periodic boundary condition is applied, it is also located at $lx + x_1$ from the origin point. Then the minimum distance is determined from both locations (x_1 and $lx + x_1$) of fiber-I to fiber-J.

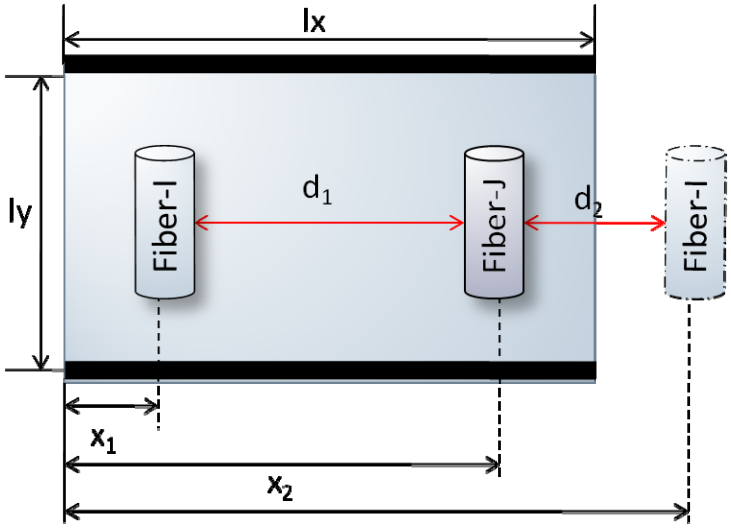

Figure 3.15: Schematic of a minimum separation distance calculation between fibers in xy-plane

Finally, the contact forces are distributed into finite element nodes by finding the closest finite element triangle surfaces from finite element contact points. The contact points are defined as the points on the surface intersected by fiber segments (fiber-I and fiber-J).

Example: sphere in a shear flow

The motion of a sphere in a simple shear flow is compared with Jeffery's work (1922). In this work the orientation of a single, neutrally buoyant, non-Brownian, sphere is shown to move in a cyclic and unchanging orbit (figure 3.15). The simulated sphere radius (r) is 10.4 lattice units, the fluid particle domain is 70 x 70 x 70, the Reynolds number is 0.93 ($Re = Gd^2/\nu$), and the relaxation time is 1.0.

Figure 3.15 compares unwrapped orientation $\left(\varphi/\pi\right)$ of a sphere with dimensionless shear rate (Gt). The LB results agree with the analytical result for a near rigid deformable at both fine and moderate discretizations.

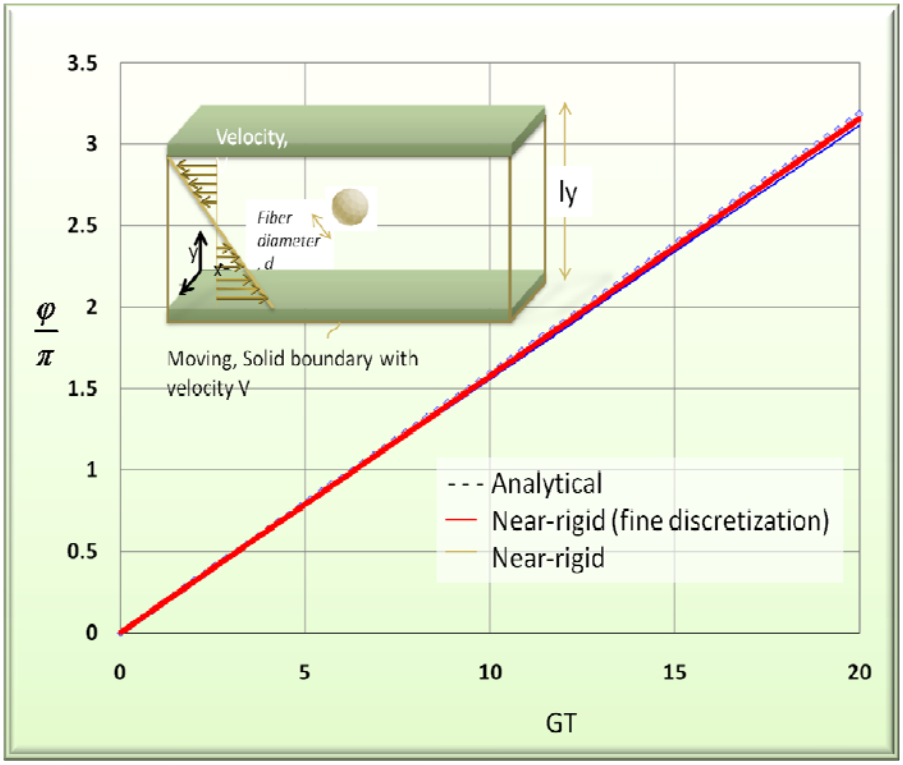

Figure 3.16: Orientation of a three-dimensional sphere

Example: fiber with low aspect ratio

A fiber (aspect ratio, A_r, is 3:1) with near rigid elasticity (E=100) is considered. The fiber contains 95 finite element nodes with 186 triangular surfaces. Fiber diameter is 9.2 lattice units with 27.6 lattice units length. The particle is placed centered in shear flow with a fluid domain of 60 x 70 x 60, and the top and bottom wall are moving with velocity 0.05. The time relaxation is 1, and the Reynolds number is 0.73. Figure 3.16 shows a three-dimensional picture of the fiber. The fluid domain describes as velocity magnitude in the x, y, and z directions. The fiber is oriented in the shear (z) direction and rotates in the xy plane.

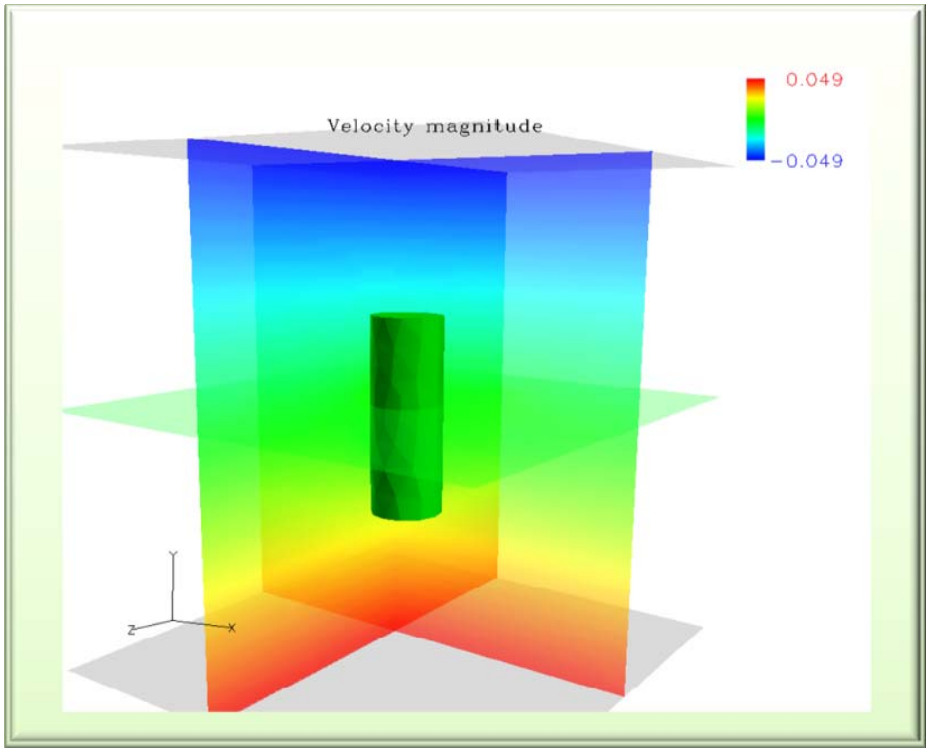

Figure 3.17: A fiber with an aspect ratio of 3:1 in simple shear flow (velocity magnitude is illustrated in three-dimensional view)

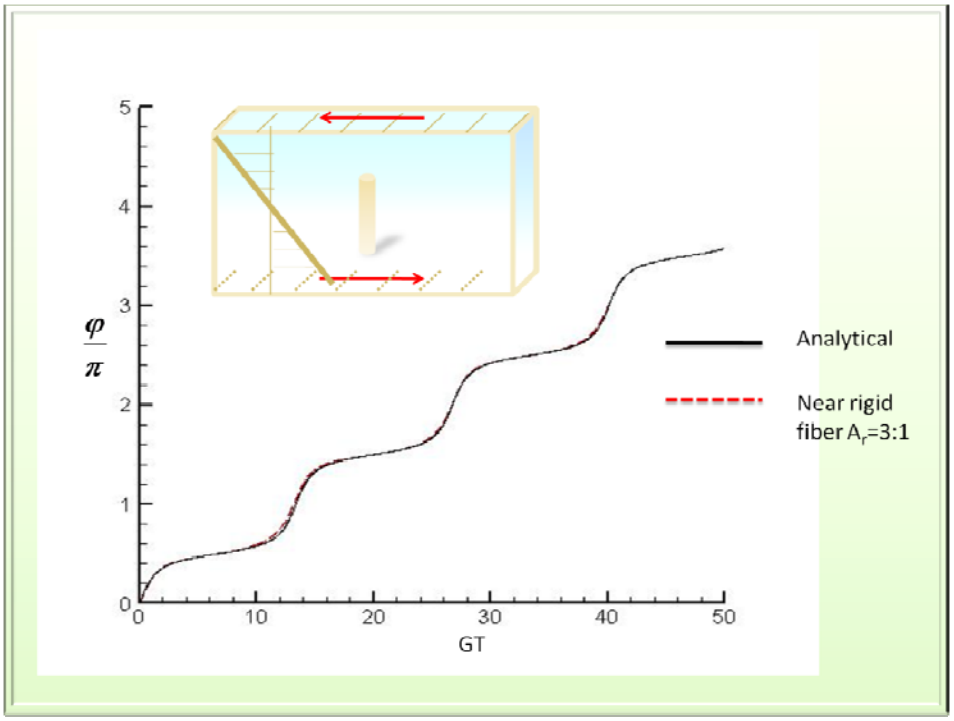

Figure 3.18: Orientation of fiber with an aspect ratio of 3:1 compared with the analytical result.

The simulation result is compared to the analytical solution for fiber orientation. In figure 3.17, the particle orientation is plotted against non-dimensional shear rate (*Gt*) and the near rigid fiber (---, red dash line) agrees well with the theoretical results (—, black solid line) with an error less than 1%.

Figures 3.18a and 3.18b show the end segment displacement of near rigid, aspect ratio 3:1 in the xy plane perpendicular to the vorticity or z direction. The displacements in the z direction do not change much and need not be shown. The displacements are calculated from the end point of the fiber relative to the center of mass of the fiber. The displacements are plotted against the non-dimensional shear rate (*Gt*).

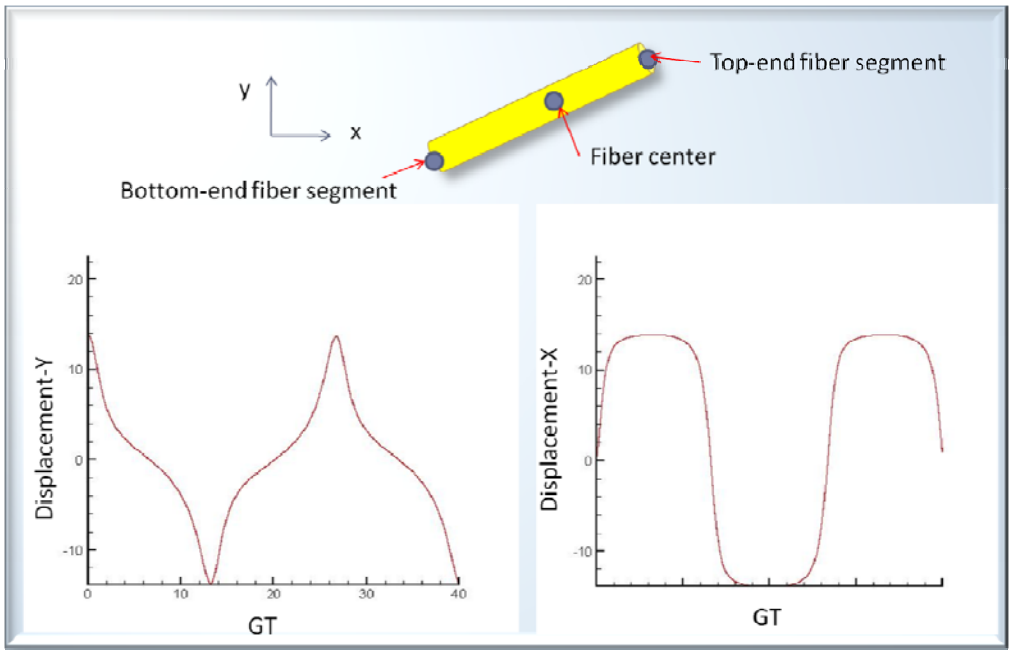

Figure 3.19: XY-displacements of a near rigid fiber (aspect ratio = 3:1) are plotted against non-dimensional rate (Gt)

The simulations for different stiffnesses are carried out at the same particle Reynolds number. The motion of a single flexible fiber with a Young's modulus is 0.025 is presented in shear flow. The resulting end displacements are expressed as function of time which is illustrated in figures 3.19a and 3.19b. The figures show that initially, the rotational behavior of the flexible fiber looks like that of a near rigid fiber. After a short of period time, the flexible fiber has a tendency to rotate more rapidly than a rigid fiber. The lower stiffness fiber exhibits more shape deformation during rotation, therefore, for a flexible fiber the period tends to decrease causing faster rotation than a rigid fiber.

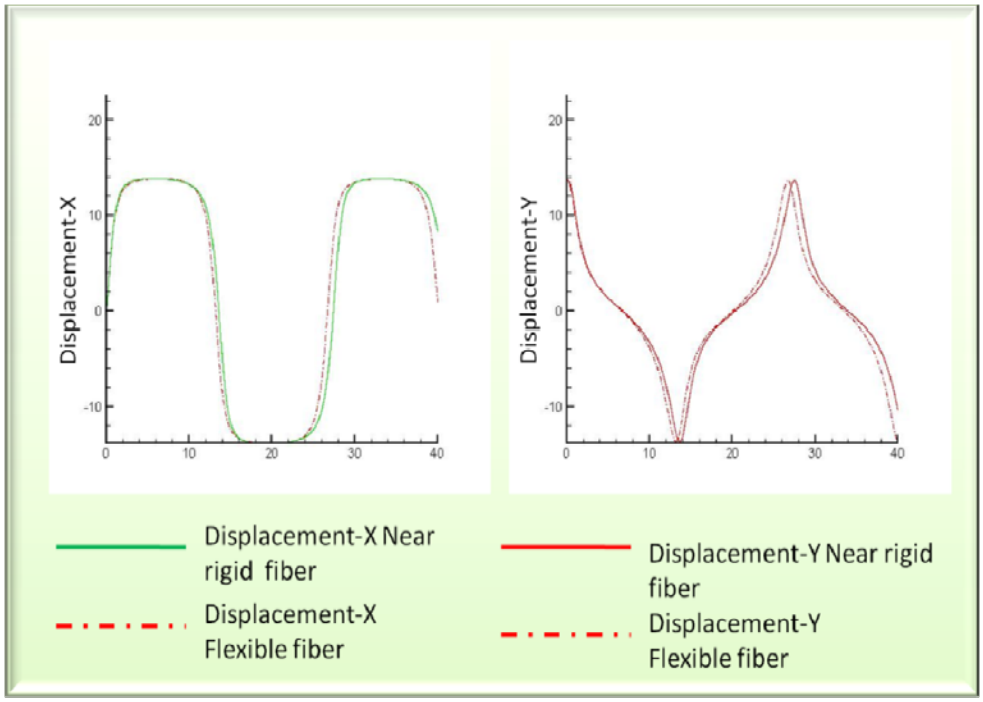

Figure 3.20: X and Y displacements of a near rigid fiber (aspect ratio is 3:1) compared with a flexible fiber (aspect ratio is 3:1)

Snapshots from the simulation of a flexible fiber are shown in figure 3.20. The aspect ratio of the fiber is 3.0, and the effective aspect ratio ($A_{re} = 1.24 \frac{A_r}{\sqrt{\ln A_r}}$) is 3.549.

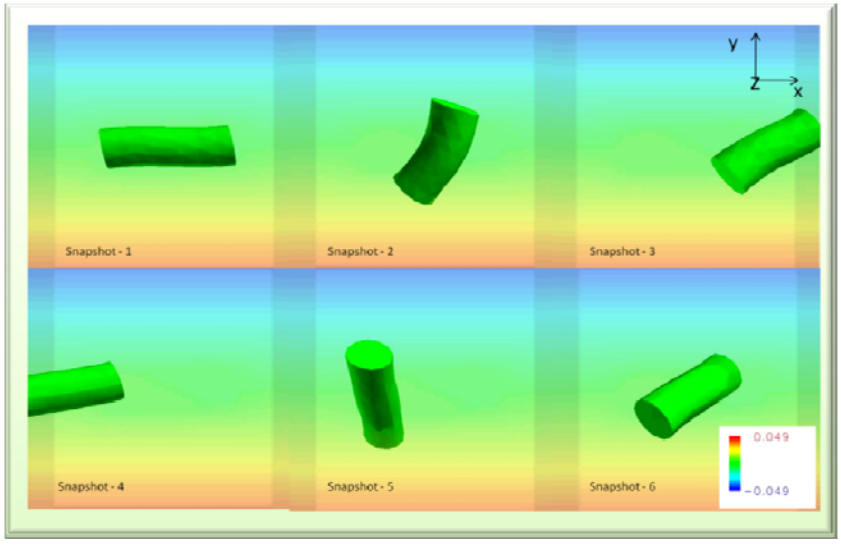

Figure 3.21: Snapshots of a flexible fiber with an aspect ratio of 3:1 with moving top and bottom domain walls (velocity magnitude is shown)

Example: fiber in a shear flow

For an ellipsoidal solid particle in simple shear flow at low Reynolds number, the rotation follows

$$\tan \varphi = A_r \tan\left(\frac{Gt}{A_r + A_r^{-1}}\right), \qquad \tan \theta = \frac{C \; A_r}{\sqrt{\left(A_r^{\,2} \cos^{\,2} \varphi + \sin^{\,2} \varphi\right)}}, \tag{3.56}$$

where A_r is the fiber aspect ratio ($A_r=L/d$ where L is the particle length and d is the particle diameter), G is the shear rate and C is a constant of integration, called the orbit constant, given by the initial orientation,

For a cylindrical particle, an equivalent aspect ratio is used (Cox, 1971)

$$A_{re} = 1.24 \frac{A_r}{\sqrt{\ln A_r}}, \tag{3.57}$$

where A_{re} is the effective aspect ratio.

In this simulation, a near rigid fiber is examined to validate with Jeffery's theory. The particle domain is set to 75 x 90 x 75 lattice units, fiber diameter (d) is 4.8 lattice units, Reynolds numbers is 0.05 ($Re = Gd^2/\nu$), and fiber length is 43.2 lattice units. Length units are in lattice spacings, and time units are in simulation time steps. A unit conversion of LB units to the metric system is explained:

- Actual domain height simulation is 0.1 m and simulation domain height is 90 lattice units. Therefore, 1 length lattice unit is 0.00111 m.

- Kinematic viscosity of water is 0.01 cm^2/seconds. Relaxation parameter value (τ) is 1. Therefore, lattice Boltzmann kinematic viscosity is $(2\tau-1)/6 = 0.167$ length lattice $unit^2$/time lattice unit.
- Density of water is 1g/cm^3. Density of water in lattice Boltzmann units is 1 mass lattice unit/length lattice $unit^3$. Therefore, 1 mass lattice unit is 1.37 x 10^{-6} kg.

The orientation of simulated fibers and a rigid fiber form Jeffery's theory are plotted against the dimensionless shear rate in figure 3.21. The results from the simulation show that the orientations of a near rigid fiber a rigid fiber from Jeffery's theory are relatively close to each other. This is presenting that the simulation results in good agreement with theory.

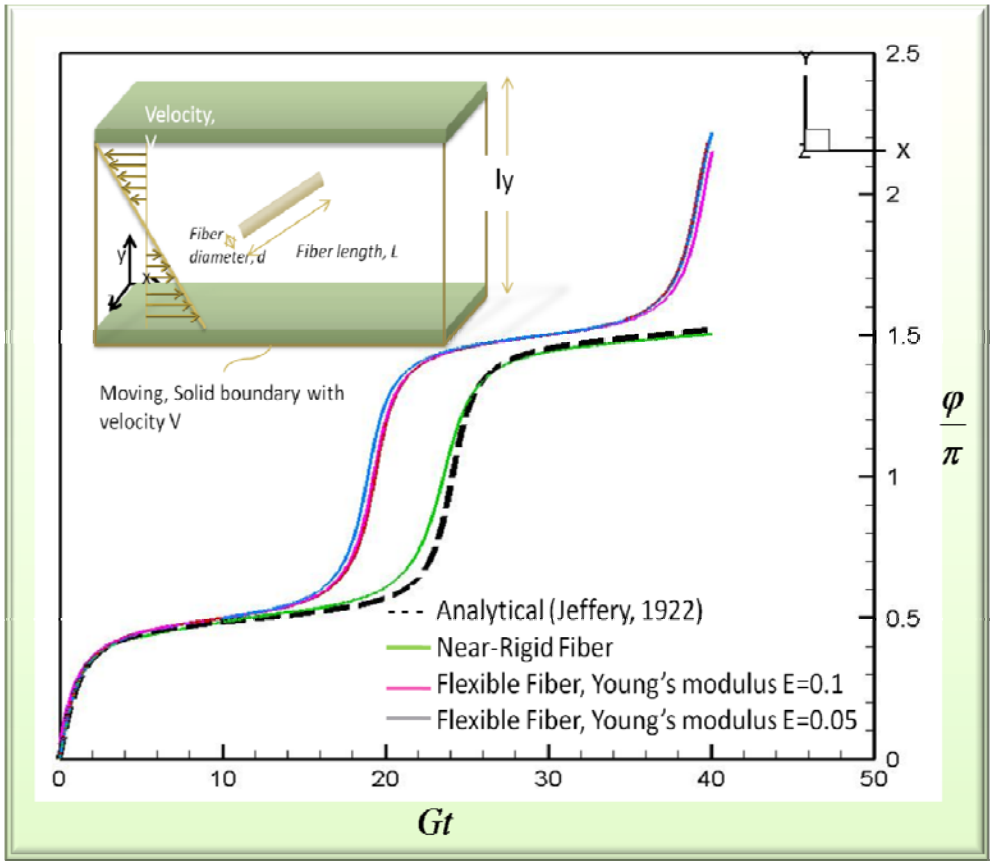

Figure 3.22: Simulation results of flexible fibers and a near rigid fiber compared with Jeffery's theory

Figure 3.22 plots the displacements of a near rigid fiber as a function of non-dimensional time, Gt. The displacements are from the end of the fiber segment relative to the fiber center. The top y-displacement is marked by a red solid line (——), the bottom y-displacement is marked by red dashed line (-------). The top x-displacement is marked by blue dashed line (-------), and the bottom x-displacement is marked by blue solid line (——). The period measured from figure 3.22 is 49.303 nondimensional shear units for the near rigid fiber. The period is 2% different from Jeffery and Cox' theoretical value, which are predicted by $Gt = 2\pi (A_{re} + 1/A_{re})$ is 48.11.

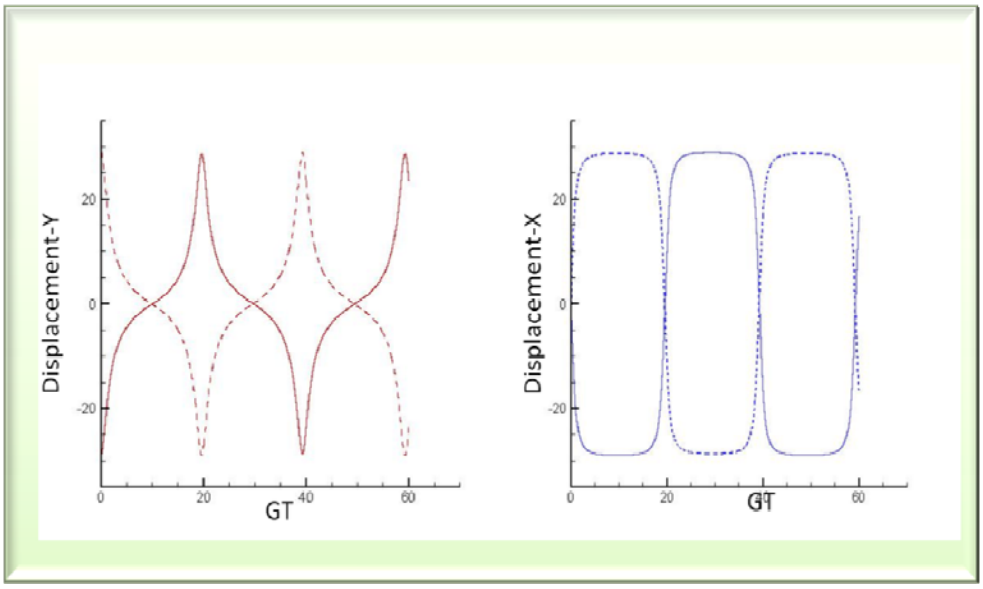

Figure 3.23: X and Y displacements of near rigid fiber aspect ratio = 9:1 plotted against non-dimensional rate, Gt

Forgacs and Mason (1959) observe in experiments involving very dilute suspensions with concentrations much less than 0.01% where fibers are essentially isolated. When subjected to laminar shear, fibers tend to orient themselves in the

direction of the flow, and when in motion they rotate, and for flexible fibers, they also bend.

Dewei Qi (2006) investigates the effect of stiffness for a flexible fiber in shear flow, and he shows results consistent with experiments and theory (Forgacs & Mason, 1959; Ross & Klingenberg, 1997; Skjetne, *et al*. 1997). He shows that the fiber with lower stiffness exhibits more shape deformation during rotating. In this study, flexible fibers are built with Young's moduli of 0.1 and 0.05. It is noted that the Young's modulus fiber in water is 6×10^6 Pa (Jafari *et al.*). It is equivalent to 2.8 (mass lattice units/ (length lattice units)*(time lattice units ^{2}), therefore the Young's modulus for this simulation result is 0.35 higher than the actual Young's modulus fiber. Recall, a fiber with lower Young's modulus will increase its flexibility. Figure 3.23 shows that fibers with lower Young's moduli are rotating faster than the near rigid one. Fibers with low Young's modulus numbers experience deformation during rotating in a shear flow.

In figure 3.23, end y-displacements are plotted as a function of time for different fiber flexibilities. It is determined from end arbitrarily fibers segments (top and bottom end segment) relative to the fiber center. It has been mentioned previously in near rigid fiber of aspect ratio is 9:1 where the period of the measured result is 48.303, which is about 2% different from theoretical values. As flexibility increases (a decrease in Young's modulus), the orbital period is reduced. The trend follows Dewei Qi's results and the experimental findings of Forgacs and Mason (1959), which demonstrates that the present model produces qualitatively accurate deformation results.

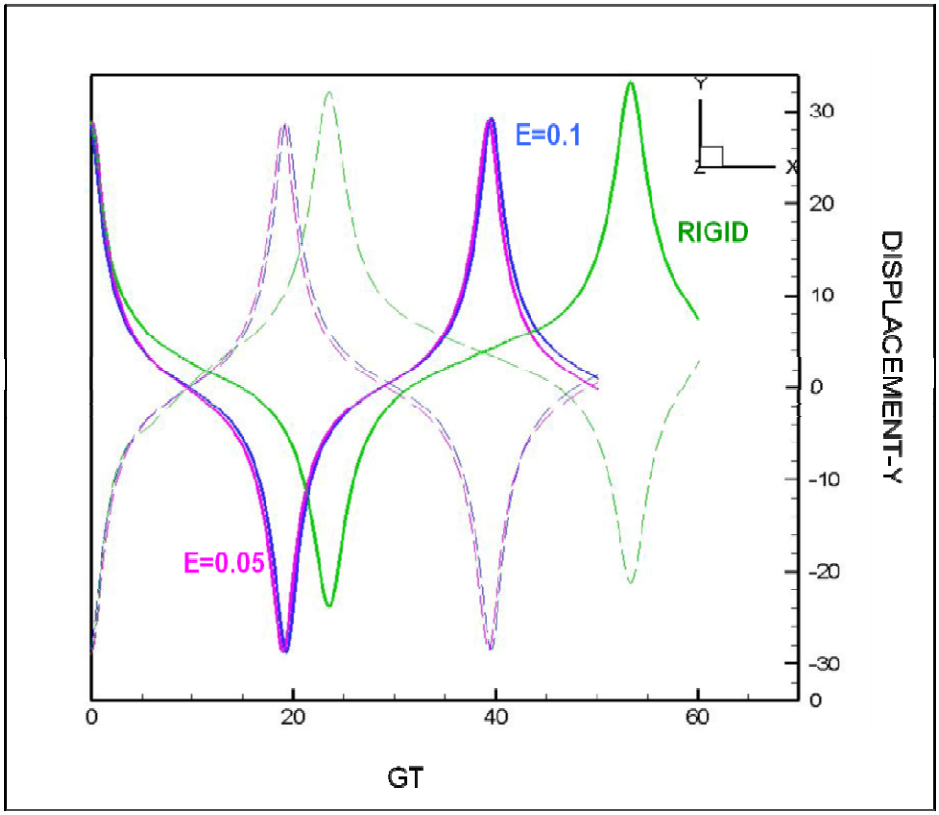

Figure 3.24: Simulation results of flexible fibers and near rigid fiber: The displacement for end arbitrarily segments of fibers (top and bottom segment) relative to the fiber center.

Figure 3.24 illustrates the motion of a fiber with deformation in three-dimension. The aspect ratio of the fiber is 9:1, Young's modulus is 0.01, and the effective aspect ratio is 7.5288. The fiber is rotating and deformating into an S shape or curved intermediate shape, after which it straightens out again. This deformed shape can be seen in higher aspect ratio, Forgacs and Mason (1959) observed this shape in the motion of the rayon filament in simple shear flow.

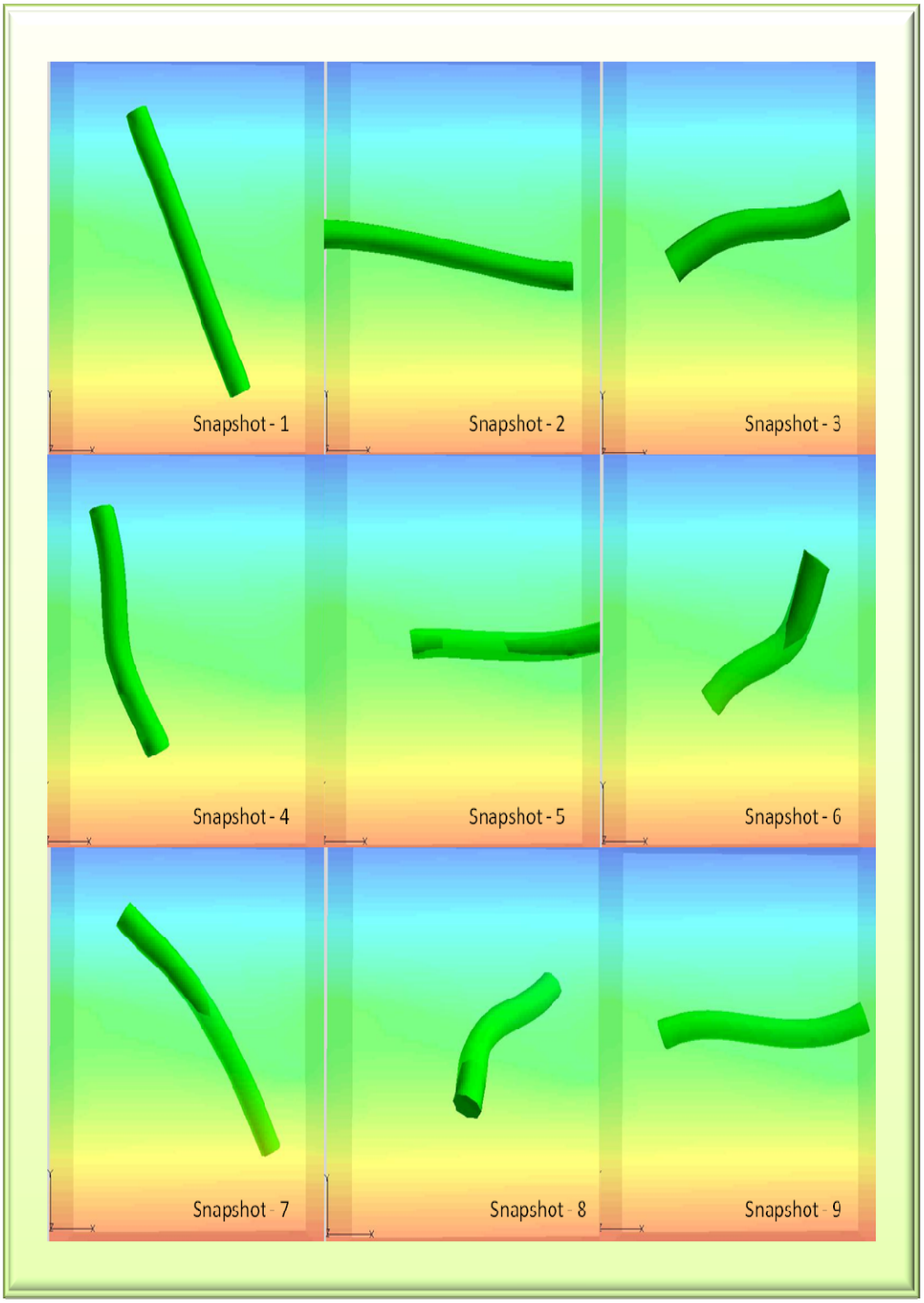

Figure 3.25: Snapshot of a flexible fiber with an aspect ratio of 9:1 in shear flow (top and bottom domain walls are moving)

Example: interaction of two fibers

It is known from experimental data that flexible fibers tend to aggregate to form flocs. These flocs are undesirable as they lead to problems in the resulting products. Figure 3.25 shows examples of solid body interactions between fibers in the absence of repulsive forces resulting in aggregation.

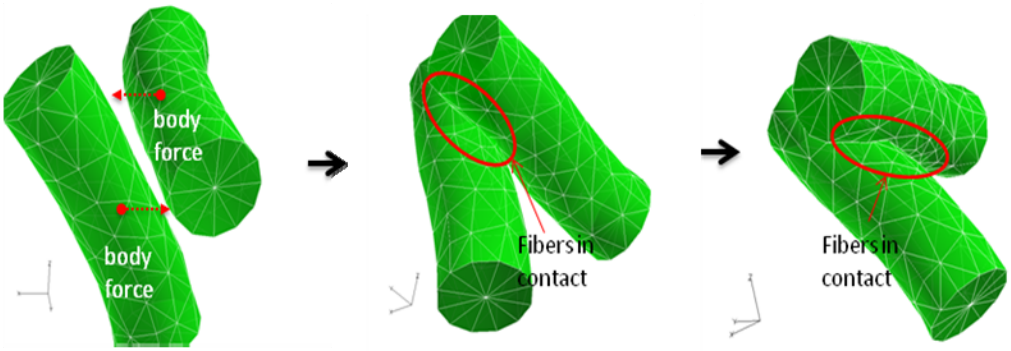

Figure 3.26: Fibers in contact (no repulsive or contact forces are taken account)

It is commonly required in the papermaking process to keep the concentration of fiber as low as 1%. One way to enhance the uniformity of the fiber suspension is to dissolve or to disperse the aggregates by adding dispersant agent. In this project, adding the contact forces among the fibers in the simulation is primary key to disperse the aggregate in fluid. The procedure to find contact forces has been explained in previous section for fiber-fiber in contact.

As shown in figure 3.26, initial body forces are given to the fibers to investigate the solid mechanics interactions between the two approaching fibers in a channel. As illustrated in this figure, the fibers gradually approach each other due to the body forces, and a collision is expected to occur when the surfaces come into contact.

To prevent penetration when two surfaces of fibers are approaching each other, the repulsive forces (equation 3.54) are applied to the two surfaces. Thus, the forces lead to separation of fibers after a short amount of time. The fibers appear to bend slightly due to the body and contact forces.

Figure 3.27 illustrates a similar setup to figure 3.26, except in this case attractive forces are added to the repulsive forces for a certain minimum approaching distance (h_{IJ}) between fibers. The purpose to add repulsive and attractive forces is to model surface charges of fibers. As illustrated in figure 3.27, it appears that there is a slight contact between fibers occurring for a short time. The repulsive forces are taking place, following this stage and leading the separation between two fibers. Furthermore, the attractive and repulsive forces (equation 3.58) are retained for the reminder of the many fiber simulations in this project.

$$F_{cI} = \underbrace{\left(-\varsigma_0 \exp[-h_{IJ}.{}^{d}\!/_{2}]\right.}_{\text{repulsive forces}} + \underbrace{\left.\left(\varsigma_1 h_{IJ}\right)^2 - \left(\varsigma_2 h_{IJ}\right) + \varsigma_3\right)}_{\text{attractive forces}} \mathbf{n}_{IJ} \qquad (3.58)$$

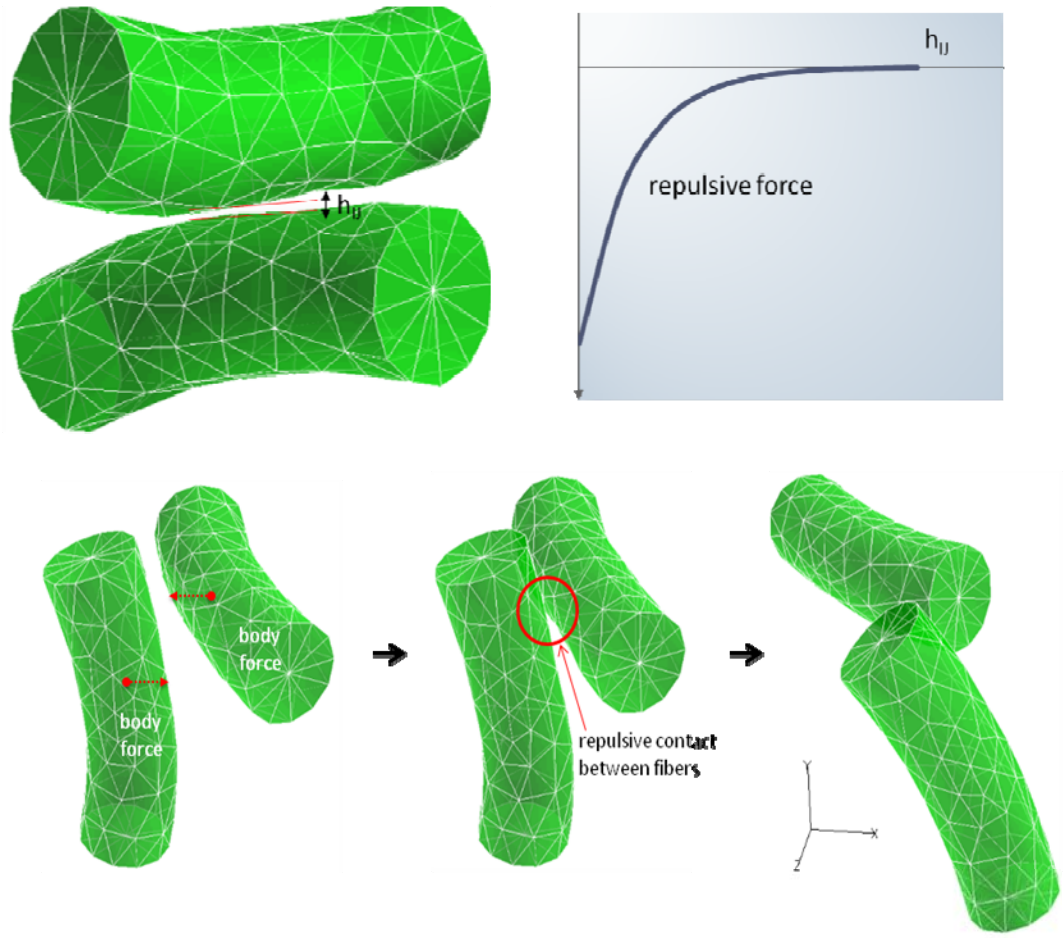

Figure 3.27: Fiber-fiber interactions with repulsive forces (contact force)

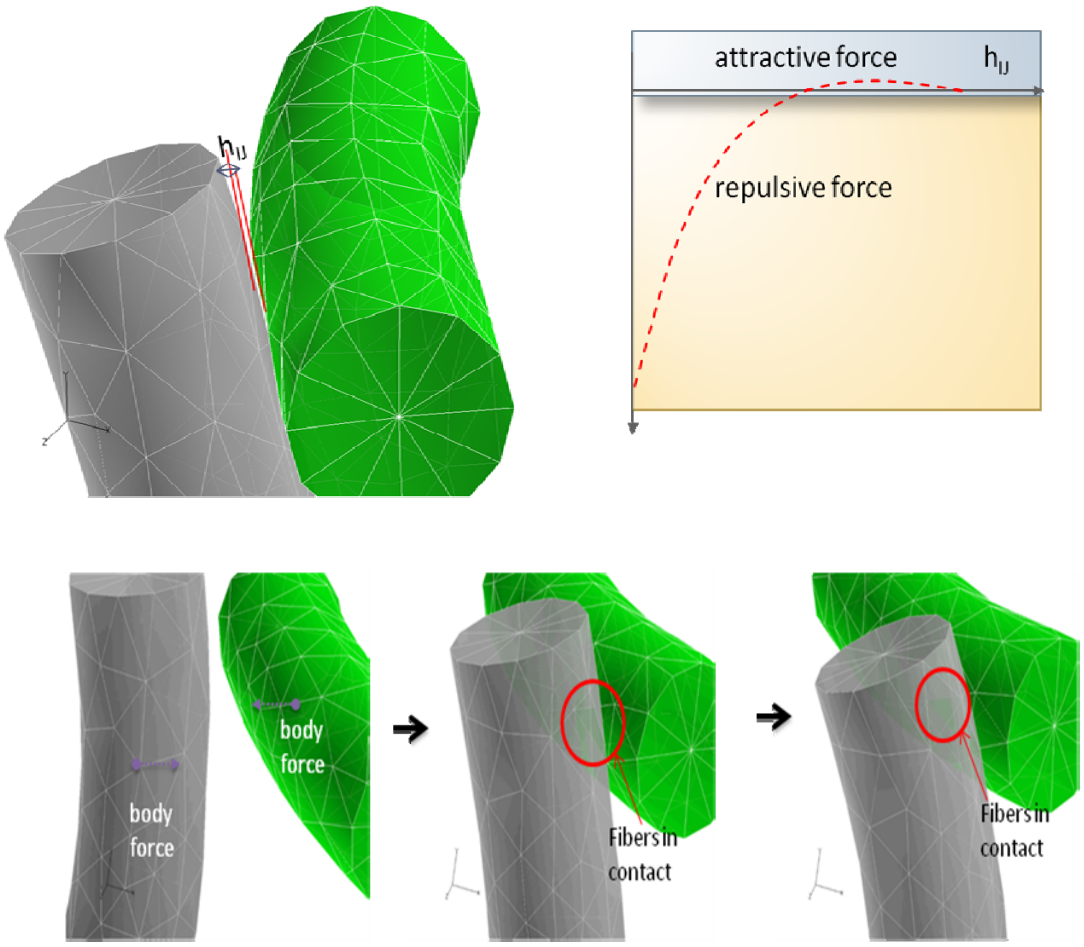

Figure 3.28: Fiber-fiber interactions with repulsive forces and attractive forces

Example: interaction of fibers

The fiber-fiber interactions for a 3:1 aspect ratio can be seen in figure 3.28. The simulation domain is 100 x 100 x 90 (lattice unit spacings), volume fraction is 0.04, fiber length is 27.6 lattice units, fiber diameter is 9.2 lattice units, Reynolds number is 0.25 and relative viscosity is 1.12. At initial time (snapshot-1), no fiber interactions occur. As the top and bottom walls move, creating shear, the interaction among fibers occurs (snaphot-2 to -6).

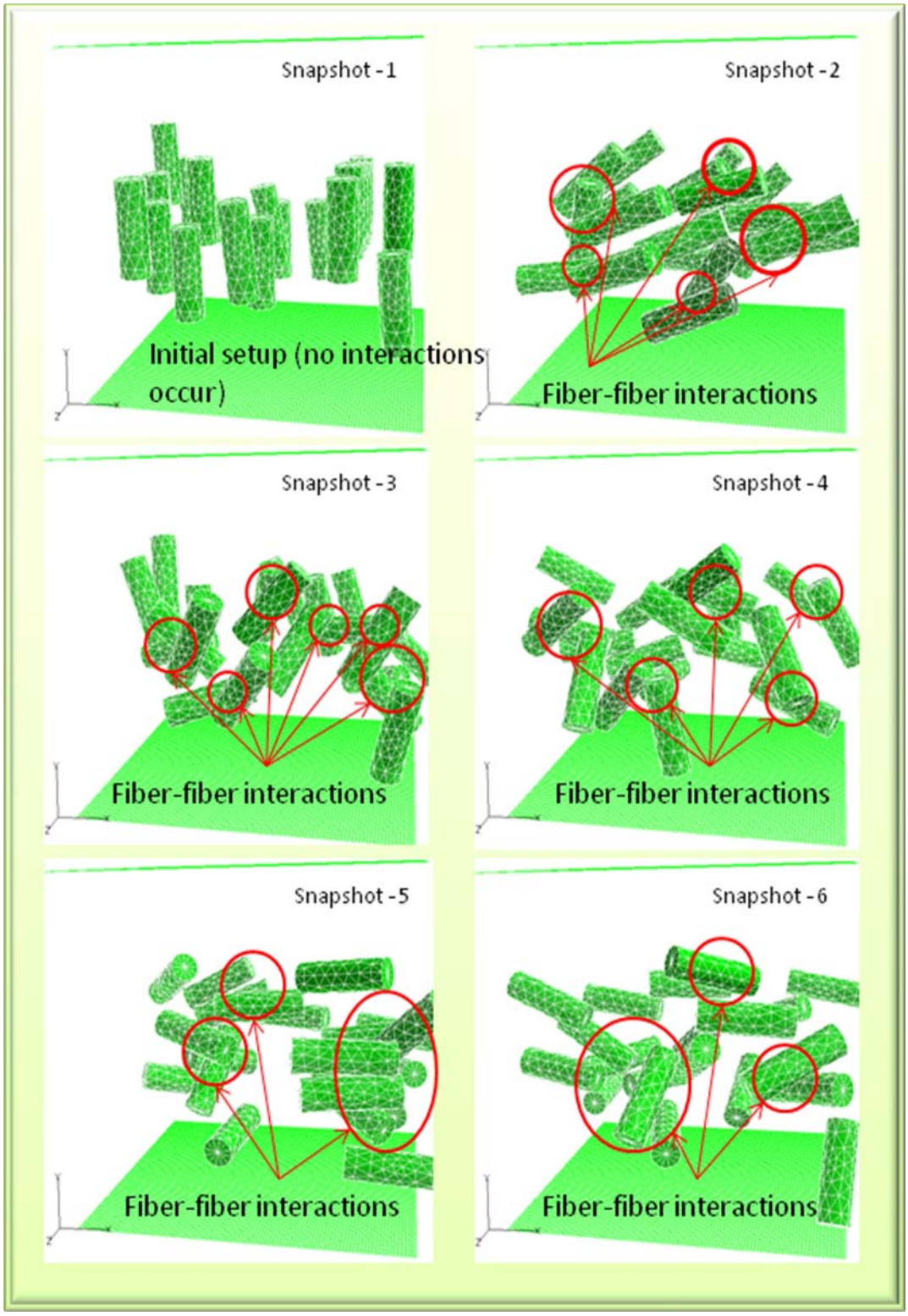

Figure 3.29: Snapshots of fibers with an aspect ratio of 3:1 with volume fraction of 0.004

CHAPTER 4

RHEOLOGY OF SUSPENSION

Effective properties are the macroscopic, properties of multiphase materials. In general, they depend on the constituent (phase) properties and the microstructure of the materials. For two-phase solid-liquid mixtures or suspensions, an effective shear viscosity, μ is simply called effective viscosity. It is defined and assumed to be a function of the solids volume fraction, ϕ.

In the dilute limit, i.e., volume fraction $\phi \rightarrow 0$, the effective viscosity, μ, of suspensions with rigid, spherical particles is obeys the Einstein relation (1906)

$$\mu_r = 1 + \alpha_0 \phi, \qquad \alpha_0 = 2.5, \qquad \phi_0 \rightarrow 0.0 \tag{4.1}$$

where μ_r is the relative viscosity ($\mu_r = \frac{\mu}{\mu_0}$), ϕ is the volume concentration, μ denotes the effective suspension viscosity, and μ_0 denotes the viscosity of the suspending fluid.

The intrinsic viscosity $[\mu]$ is

$$[\mu] \equiv \lim_{\phi \rightarrow 0} \frac{\mu_r - 1}{\phi} \tag{4.2}$$

Using the intrinsic viscosity, the Einstein relation can be formally generalized to

$$\mu_r = 1 + [\mu]\phi \tag{4.3}$$

Jeffery (1922), in rigorous treatment of the motion of a rigid ellipsoids and spheroids with a certain aspect ratio, is the first to calculate values for [μ] as a function of the particle aspect ratio. Therefore, equation (4.3) is called the Jeffery-Einstein relation.

Jeffery (1922) tries to determine the viscosity increase of a suspension over its solvent due to the presence of hydrodynamically isolated ellipsoid particles. However, the rotations of particles render his energy dissipation calculation indeterminate, owing to the effect of instantaneous particle orientation and the need to know the initial particle orientation.

Burgers (1938) derives a dimensional factor (α_0) for the case of cylindrical rods. It can be expressed as follows:

$$\alpha_0 = \left[\frac{A_r^{\ 2}}{6\left(\ln 2A_r - 1.80 \right)} \right] \sin^4 \theta \sin^2 \varphi \ , \tag{4.4}$$

where $A_r = L/d$ is the length-to-diameter or aspect ratio of the rod, θ and φ are the spherical coordinates, and α_0 is a dimensionless factor determined by the shape, dimensions, and orientations of the suspended particles.

This theory is based on the assumption that rigid cylindrical particles suspended in shear flow are without inertial effects and Brownian motion. In addition to these conditions, wall effects are neglected, and there are no interactions between particles.

Nawab and Mason (1958) suggest using an equivalent ellipsoid aspect ratio, A_{re}, in the results obtained from Jeffrey's equations by Burgers. Using this modification the expression for the relative viscosity becomes

$$\alpha_0 = \left[\frac{2 A_r^{\ 2}}{3\pi A_{re} \left(\ln 2 A_r - 1.80 \right)} \right] \tag{4.5}$$

Several experimental studies (Eirich, 1936; Nawab & Mason, 1958; Myers, 1962) have been done to predict viscosity for rigid rods suspensions, however, none of the results obtained in these studies agree with theory or among themselves. This disagreement is because of a lack of understanding of the effects of fiber properties on viscosity.

Blakeney (1966) experimentally studies the effect of concentration on the relative viscosity at concentrations where fiber-fiber interactions are negligible. He uses fibers with aspect ratios of 19.2:1 and 20.3:1 at concentrations up to 0.009 in a concentric cylinder viscometer. At concentrations 0.0042 to 0.0050, there is a sudden increase in the relative viscosity followed by a slight decrease and a second increase. This behavior correlates to a corresponding increase and decrease in the orientation factor over the same concentration range. A general experimental viscosity-concentration relation for suspension is given by Blakeney as follows

$$\mu_r = 1 + K_1 \phi + K_2 (\alpha_0 \phi)^2 , \tag{4.6}$$

where K_1 is a dimensionless factor determined by the shape, dimension, and orientation of the suspended particles, $K_1 = \alpha_0$, K_2 is determined to give the best fit of the experimental data, and ϕ is volume concentration.

Figure 4.1 depicts the results of the viscosity measurements which it is redrawn from Blakeney's experimental result. He applies two sets of fibers in this study:

1. Straight fiber aspect ratio 19.2:1 fiber diameter 16.9 microns (denoted by blue solid circle, ●), Straight fiber aspect ratio 20.3:1 fiber diameter 20.3 microns (denoted by blue hallow circle, ○)
2. Nylon fiber aspect ratio 19.2:1 fiber diameter 16.9 microns (denoted by blue solid triangle, ▲),

   Nylon fiber aspect ratio 20.3:1 fiber diameter 20.3 microns (denoted by black hollow triangle, △).

In this simulation, relative viscosity is calculated from the ratio of top or bottom wall pressure to suspension pressure which is given as follow

$$\mu_r = \frac{P_{wall}}{G\mu}, \tag{4.7a}$$

where P_{wall} is the wall pressure (= top or bottom wall force / top or bottom wall area), G is the shear rate (= top wall velocity, u1 – bottom wall velocity, u2/ height simulation domain, ly), μ is the dynamic viscosity (= fluid density,ρ x kinematic viscosity,ν)

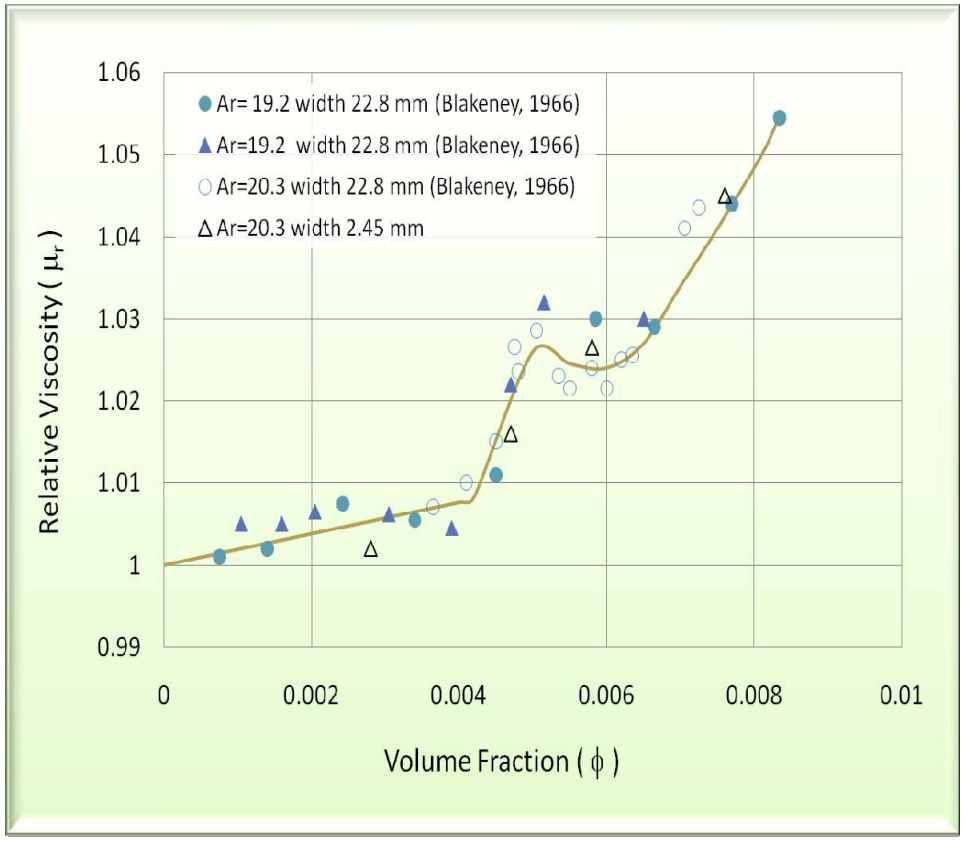

Figure 4.1: Effect of concentration on relative viscosity (Redrawn from Blakeney's experimental results)

Fiber suspensions with an aspect ratio of 18:1

Low concentration suspensions

To compare with Blakeney's results, a simulation is performed with near rigid and flexible fibers having an aspect ratio of 18:1 (fiber length and diameter are 86.4 lattice units and 4.8 lattice units). Initially the fibers are placed in random positions in the simulation domain. To create shear flow, the top and bottom walls move. Relative viscosities are calculated for volume concentration less than 0.006 to verify with experimental measurements. Table 14 shows relative viscosity results for different

volume concentrations of near rigid, aspect ratio 18:1 fibers. These values are also compared with the experimental and theoretical measurements.

Table 14: Values of relative viscosities as a function of volume concentration with near rigid fiber aspect ratio 18:1 and fiber diameter 4.8 lattice spacing units.

Volume concentration	Relative viscosity
0	1
0.00117	1.01
0.00374	1.007
0.004	1.02
0.0053	1.0125

In figure 4.2, relative viscosity is plotted against near rigid fibers suspensions from simulation, experimental and theoretical results for varying suspension concentrations. Near rigid fiber simulations are shown as solid Square (■) in concentration up to 0.006 and the results are compared with experimental results by Blakeney (1966). Blakeney's (1966) data shown as solid circle (●) and solid triangle (▲) for different type of fibers with aspect ratio of 19.2:1, and hollow circle (○) and hollow triangle (△) for different type of fibers with aspect ratio of 20.3:1. Simulation results compare well with both theory and experimental observations.

Figure 4.3 depicts eight near-rigid or straight fibers in shear flow from the simulations. The simulation parameters are as follows: simulation domain is 140 x 155 x 140 lattice spacing units, relaxation time is 1.0, Reynolds numbers is 0.09, and volume concentration, ϕ is 0.004.

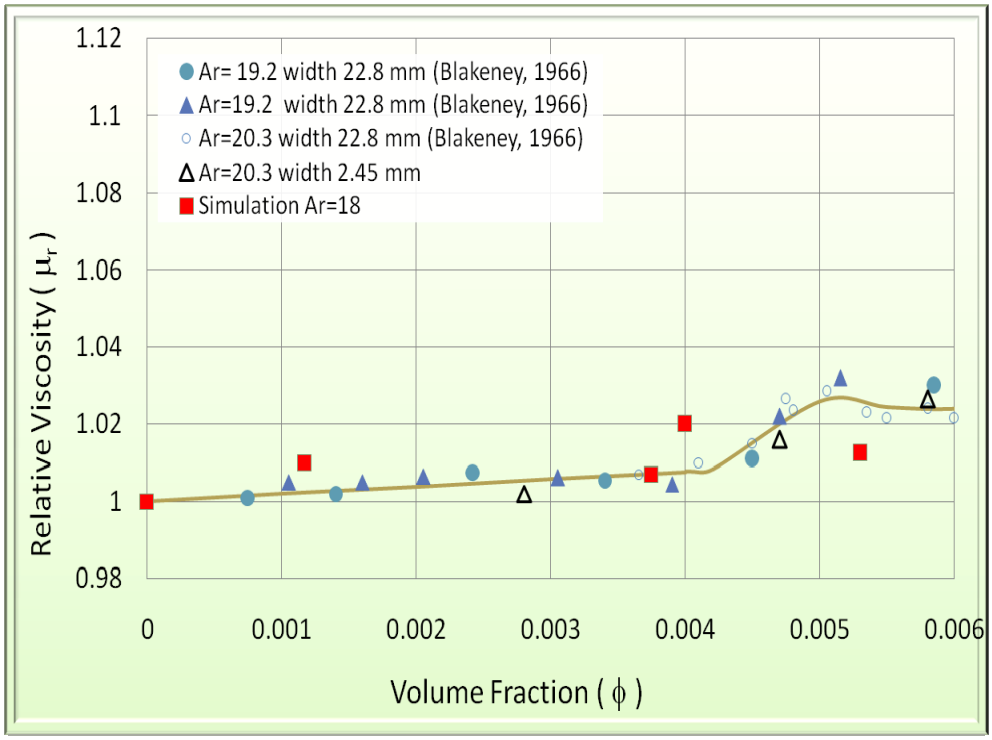

Figure 4.2: Relative viscosity for near rigid fiber suspension simulation with aspect ratio 18:1 for dilute and semi-dilute fiber suspension. The results are compared to experiments by Blakeney (1966).

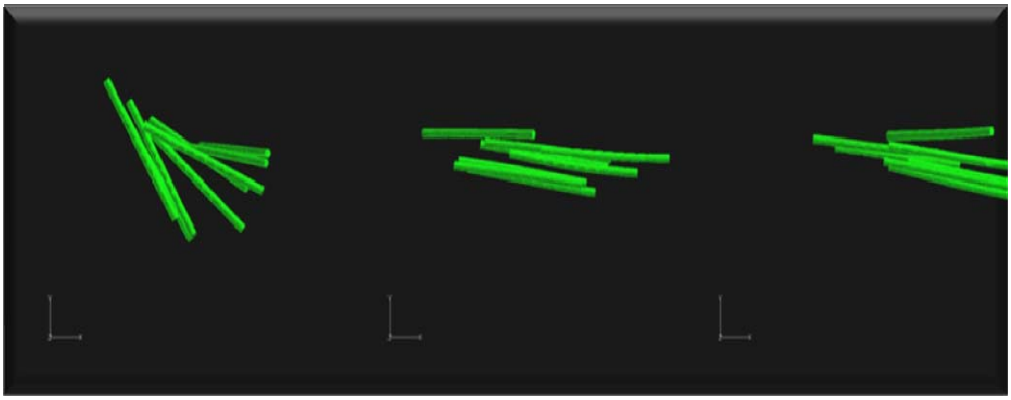

Figure 4.3: Near rigid fibers with an aspect ratio of 18:1 in shear fluid flow

With increasing fiber flexibility, i.e., decreasing Young's modulus, the relative viscosity of the suspension is higher than the near rigid case. Table 15 shows simulation

results from flexible fibers with volume concentration up to 0.006. This effect can be seen in figure 4.4, where the relative viscosities are plotted against suspension concentration for flexible fibers. Flexible fibers from the simulation are denoted by solid diamonds (◆), near rigid fibers from the simulation results are denoted by solid squares (■), and Blakeney's experiment data are shown as solid triangles (▲) for rigid fiber aspect ratio 19.2:1 and hollow circles (○) for rigid fiber aspect ratio 20.3:1. Fibers deformation tends to increase the orientation of the fibers and fiber-fiber interactions, raising the value of relative viscosity.

Flexible fiber simulation pictures can be seen in figure 4.5 for a volume fraction of 0.006. The simulation parameters are as follows: domain is 140 x 155 x 140 lattice spacing units, fiber diameter is 4.8 lattice spacings, fiber length is 86.4 lattice spacings, and relaxation time is 1.0. Fiber-fiber interactions are shown infrequently because of the dilute concentration of suspension, however, as is visible in figure 5.4 the fibers quickly create networks among them in a short time period (interactions among the fibers are denoted by the red circle).

Table 15: Values of relative viscosities as a function of volume concentration with flexible fiber aspect ratio 18:1 and fiber diameter 4.8 lattice spacing units.

Volume concentration	Relative viscosity
0	1
0.0056	1.095
0.006	1.09

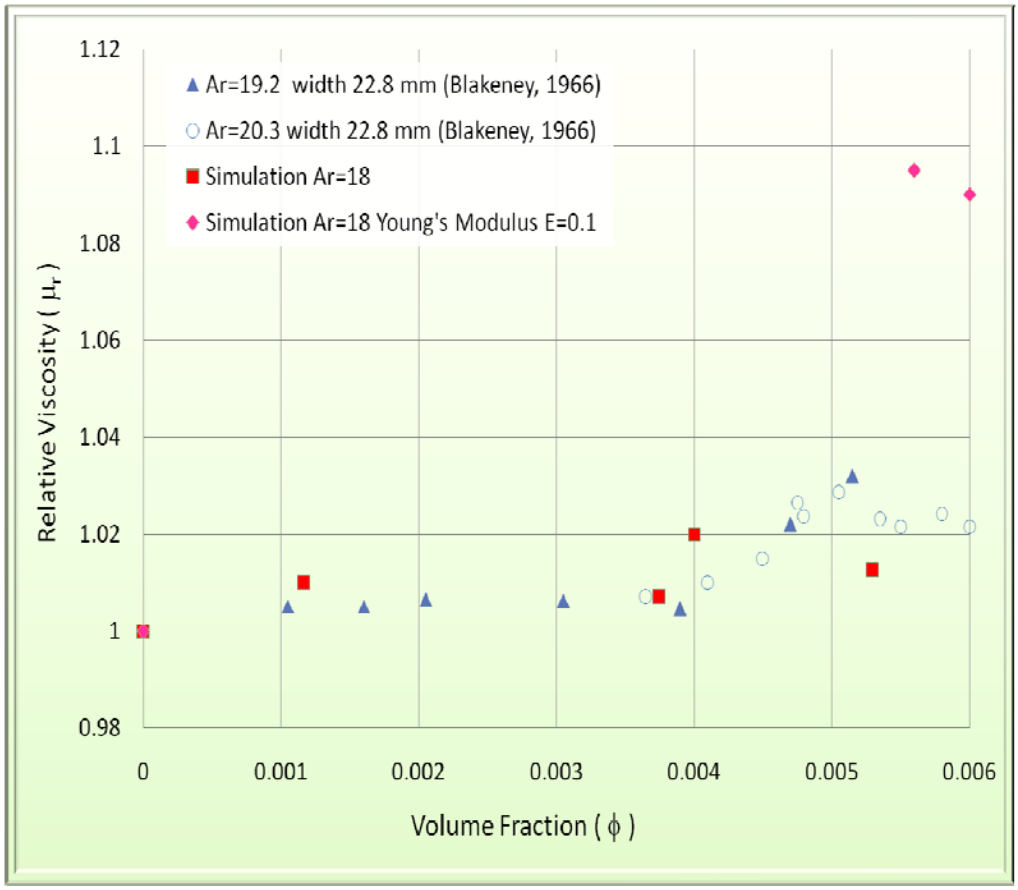

Figure 4.4: Relative viscosity for flexible fiber suspension simulations with fiber aspect ratio of 18:1 for dilute and semi-dilute fiber suspension. The results are compared to experimental results (Blakeney, 1966) and simulation results for near rigid fiber suspensions.

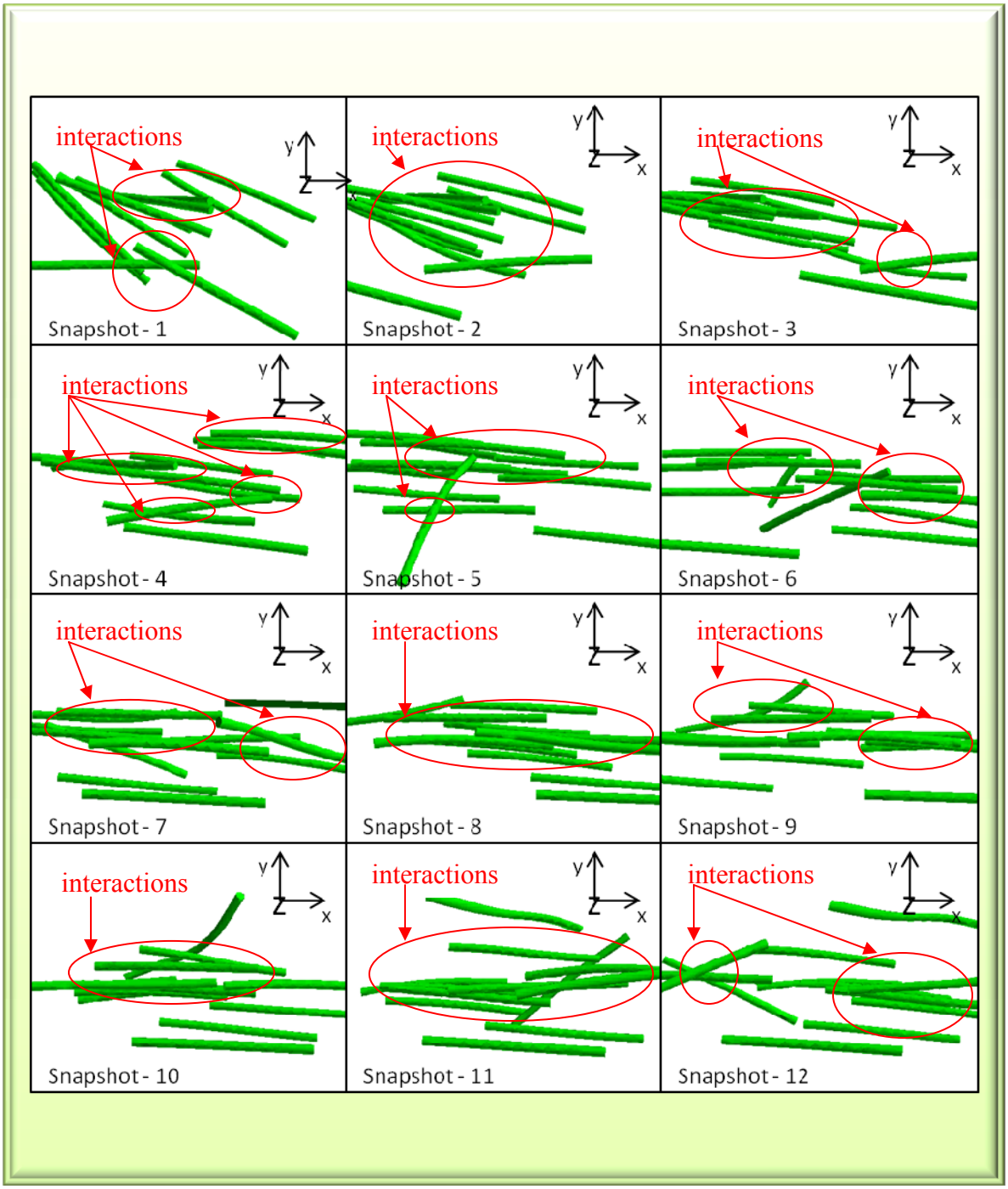

Figure 4. 5: Snapshots of aspect ratio 18:1 flexible fibers with a volume fraction of 0.006 in simple shear flow for varying simulation times

High concentration of suspensions

Higher volume concentrations for fiber suspensions with an aspect ratio of 18:1 are analyzed. Figure 4.6 shows the relative viscosities for near rigid fiber suspensions (hollow diamonds, ◇) and for flexible fiber suspensions (red solid triangles, ▲). The relative viscosities have a tendency to increase with the volume fraction of suspensions. Moreover, increasing flexibility causes the suspension to produce higher relative viscosities values.

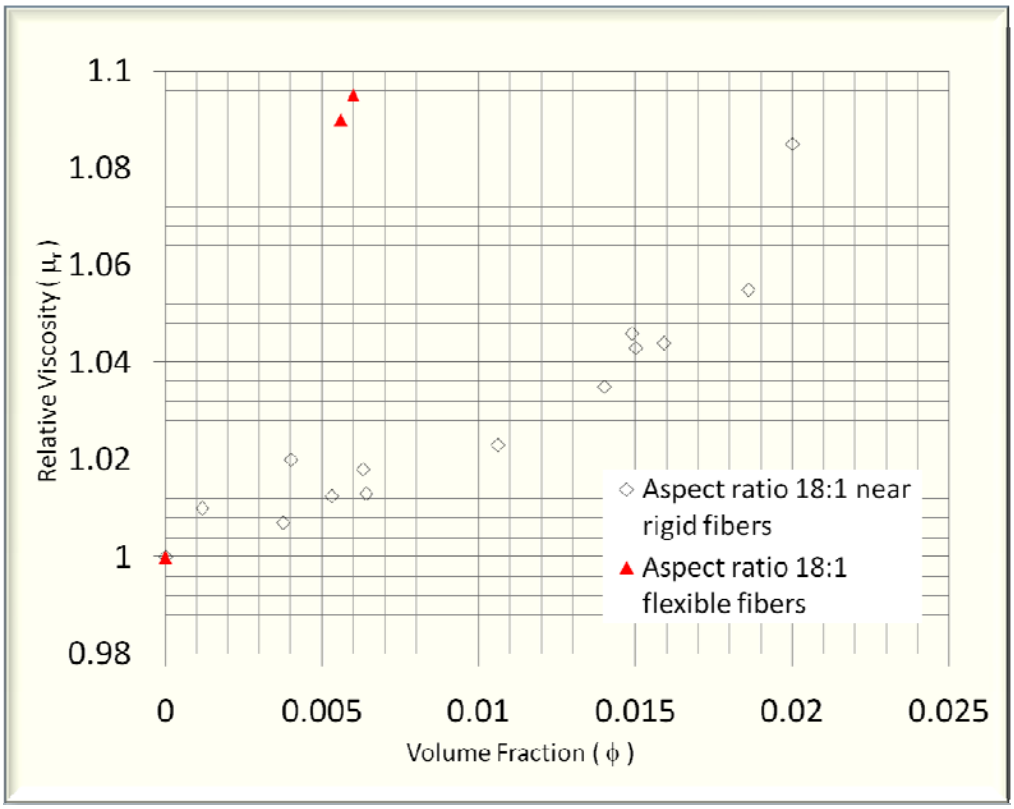

Figure 4.6: Dilute and semi-dilute relative viscosity results for near rigid fiber suspension simulations with aspect ratio of 9:1.

Figure 4.7 depicts an example of a flexible fiber suspension with a volume fraction of 0.008. Simulation domain is 140 x 155 x 140 lattice units, fiber length is 86.4 lattice unit spacing, fiber diameter is 4.8, and Reynolds number is 0.1.

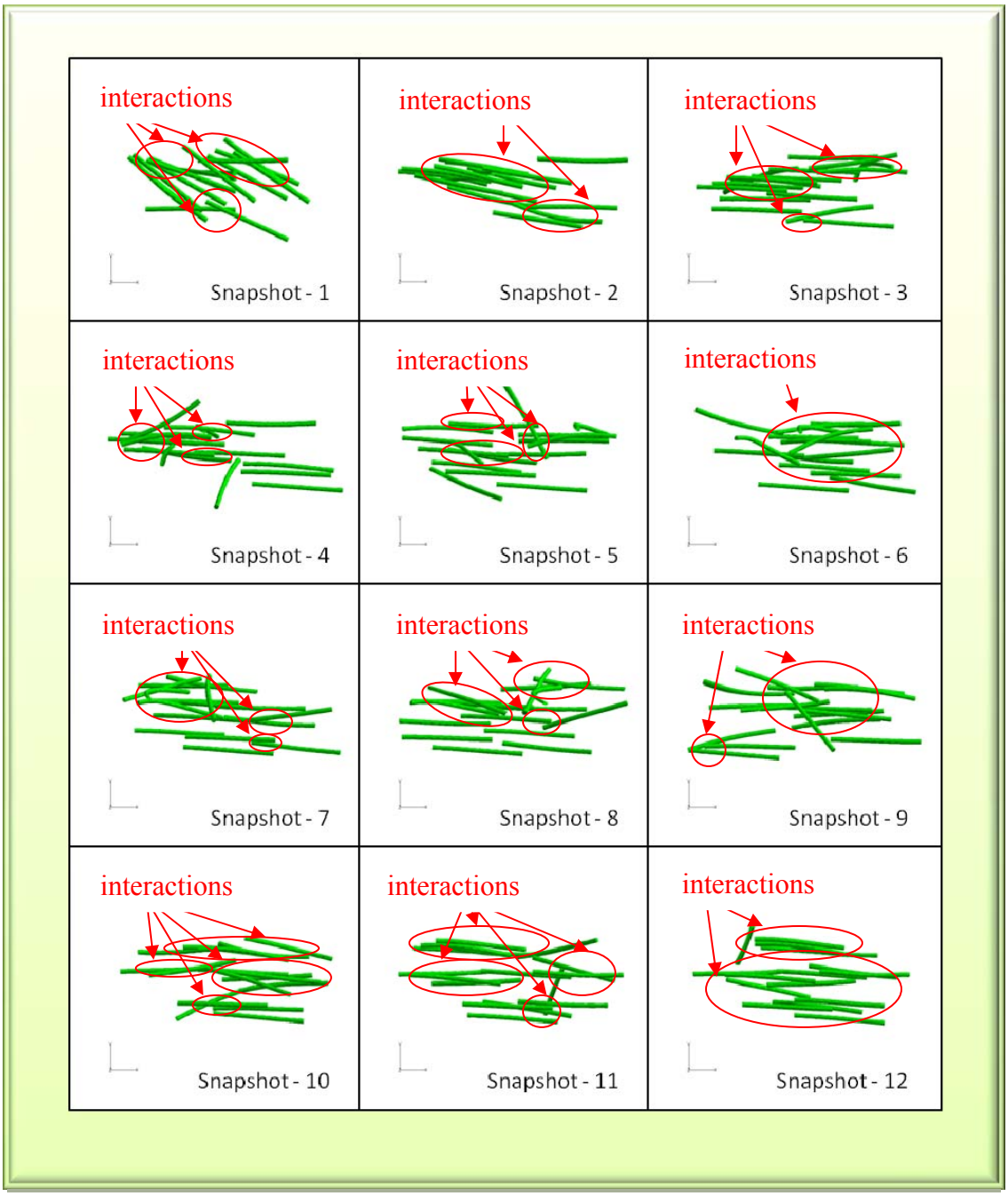

Figure 4.7: Snapshots of flexible fibers aspect ratio 18:1 for volume fraction 0.008

Fiber suspensions with aspect ratio of 9:1

Low concentration suspensions

Following this work, fiber suspension aspect ratio 9:1 is constructed to verify the numerical method of the simulation. Based on the experimental measurements from Blakeney (1966) and the theoretical values from Mason & Manley (1959), near rigid fibers are simulated up to volume concentration of 0.006. Table 16 shows the volume concentrations of near rigid fibers and the simulated relative viscosities. The comparison between simulation results and theoretical can be seen in figure 4.8, where the predicted values have 0.2% average error. Flexible fibers from simulation results are shown as solid circles (●), and the theoretical values are shown as solid line (—).

Table 16: Values of relative viscosities as a function of volume concentration with flexible fiber aspect ratio 9:1 and fiber diameter 6.4 lattice spacing units.

Volume concentration	Relative viscosity
0	1
0.00154	1.0003
0.00346	1.002

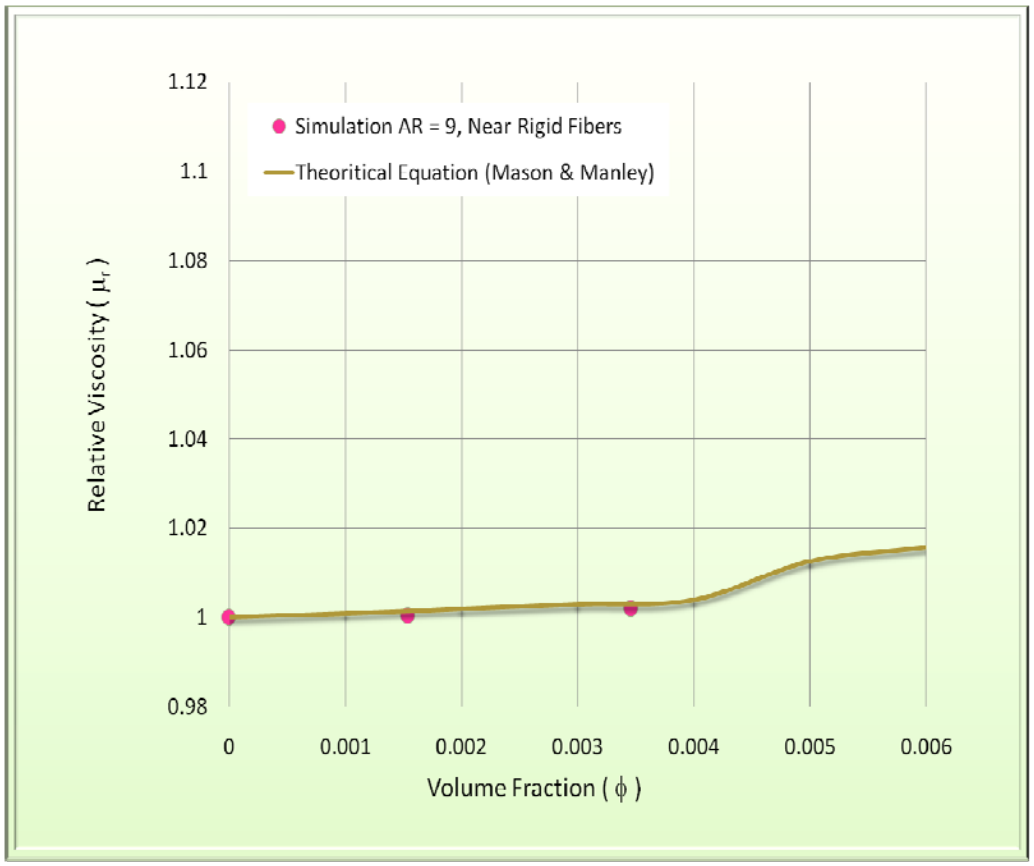

Figure 4.8: Relative viscosity for near rigid fiber suspension simulations with an aspect ratio of 9:1 for dilute and semi-dilute fiber suspension. The results are compared to theoretical results (Mason & Manley).

High concentration suspensions

The study of higher volume concentration for fiber aspect ratio 9:1 is continued for different fiber flexibilities. Figure 4.9 shows the fiber suspensions for near rigid fiber (denoted by red asterisks, ✳) and flexible fibers (denoted by black solid circles, ●). The simulation results show the increase of relative viscosity of fiber suspension as the volume fraction is raised for near rigid and flexible fibers, however, the relative viscosities for flexible fibers are somewhat similar to relative viscosities for near rigid fibers. This effect is because of low Reynolds numbers are applied for flexible fibers,

showing that the Reynolds numbers have influence in addition to the relative viscosity values. Increasing Reynolds numbers will raise the relative viscosity of fiber suspension.

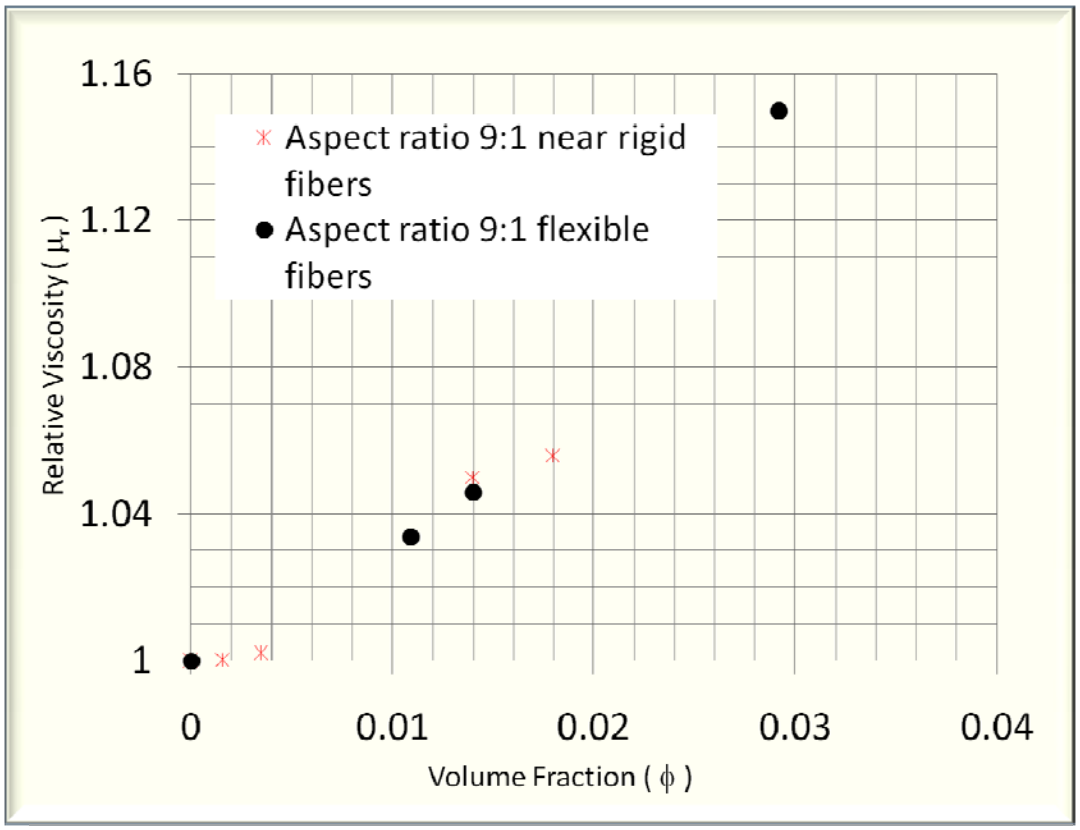

Figure 4.9: Relative viscosity for near rigid and flexible fiber suspensions simulation with an aspect ratio of 9:1.

Application to paper manufacturing

Paper consists of a network of fibers, where the most commonly used fibers in manufacturing are cellulose fibers from wood. To produce paper a fiber suspension (a mixture of water and cellulose fibers) with a mass fraction of fibers less than 1% enters the part of the paper machine often referred to as a headbox. The main assignment of the headbox is to transform a pipe flow, with a diameter of about 800 mm, to a uniform jet around 10 mm thick and up to 10 m wide. The modern headbox typically consists of three parts: the flow distributor or manifold, the tube bank and the nozzle (see figure 4.10).

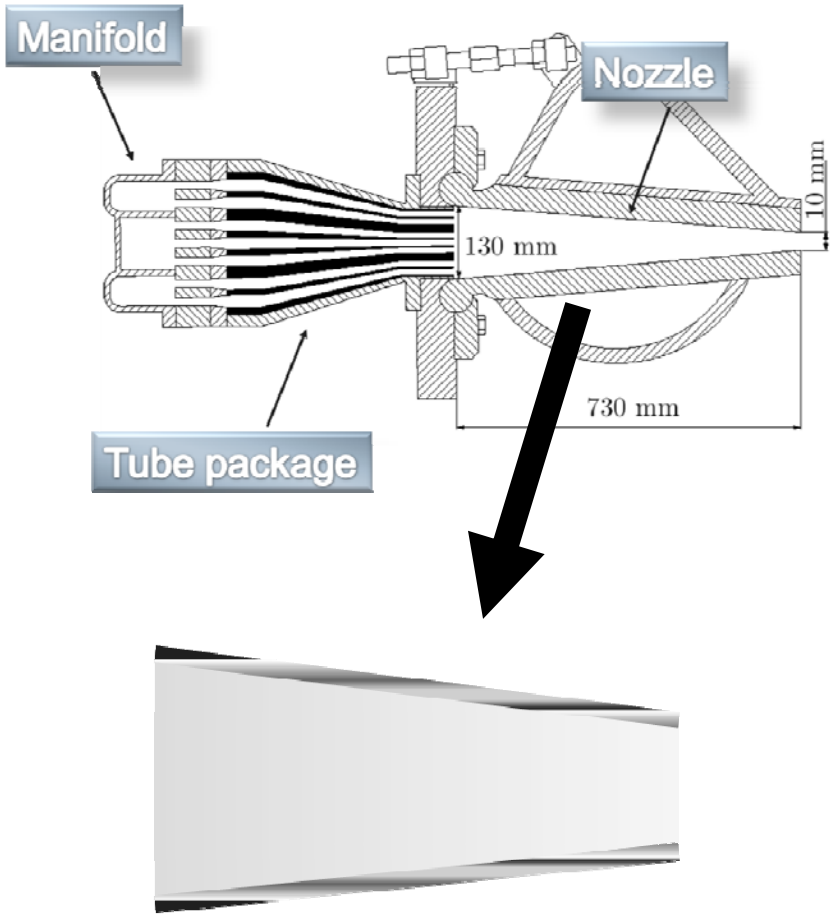

Figure 4.10: Schematic of modern hydrolic headbox (Smook, 1992)

The fiber suspension is usually fed to the headbox from a perpendicular direction to the nozzle and jet. Usually the flow distributor has a tapered geometry designed to give a constant static pressure across the machine width. This design ensures that the speed of the headbox jet is constant along the width of the paper machine. On exiting the manifold, the fiber suspension enters the tube bank through a system of holes, usually representing around 10% of the area. The main purpose of the tube bank is to produce a pressure drop to promote a more uniform flow profile across the full width of the papermaking machine. Each flow channel in the tube banks of modern headboxes feature a step-difuser design, which results in a defined separation of the flow, which provides a controlled and elevated pressure drop.

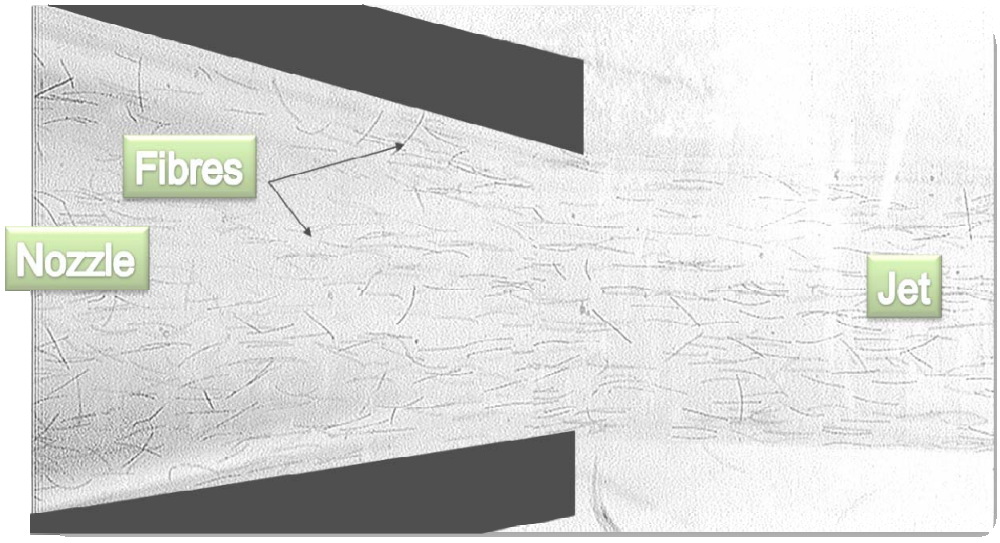

Figure 4.11: Image of fiber-fiber interaction inside headbox or diverging channel

A study of rheology of fiber suspensions has been done previously in shear fluid flow. Several factor such as fiber aspect ratio, fiber flexibility, volume fraction, and fiber orientation affect the rheology (relative viscosity) of a suspension. Flow of fiber suspension in headbox through uniform flow is involving interaction among fibers as seen in figure 4.11.

In this project, modifying the wall boundary conditions is needed to accomplish a domain similar to diverging channel or headbox (figure 4.12a). The top and bottom walls in simulation domain must be changed into inclined static top and bottom walls. To calculate these walls, a ratio $^{a}/_{b} = {}^{p}/_{q}$ is taken into account (schematic figure 4.12b), therefore y_{itop} and $y_{ibottom}$ become (detail calculations can be found in appendix)

$$y_{itop} = \frac{(ly - ½)\,(lx - ½) - (ly - ½)\;\; x_i + (h + ½(ly - 1)) + ½(h + ½(ly - 1))}{½ + (lx - ½)},$$

$$y_{ibottom} = \frac{(½(ly - 1) - h + ½)\;\; x_i - ½\,h + ½(½(ly - 1)) - ½(lx - ½)}{½ + (lx - ½)}, \tag{4.8}$$

where y_{itop} is the top wall of the diverging channel, $y_{ibottom}$ is the bottom wall of the diverging wall, ly is the domain height, lx is the domain length, x_i is the point of lattice-node in x direction, h is the height from the center wall to $y = ly - {}^{1}/_{2}$. The top and bottom walls proceed as no-slip non-moving boundary condition walls.

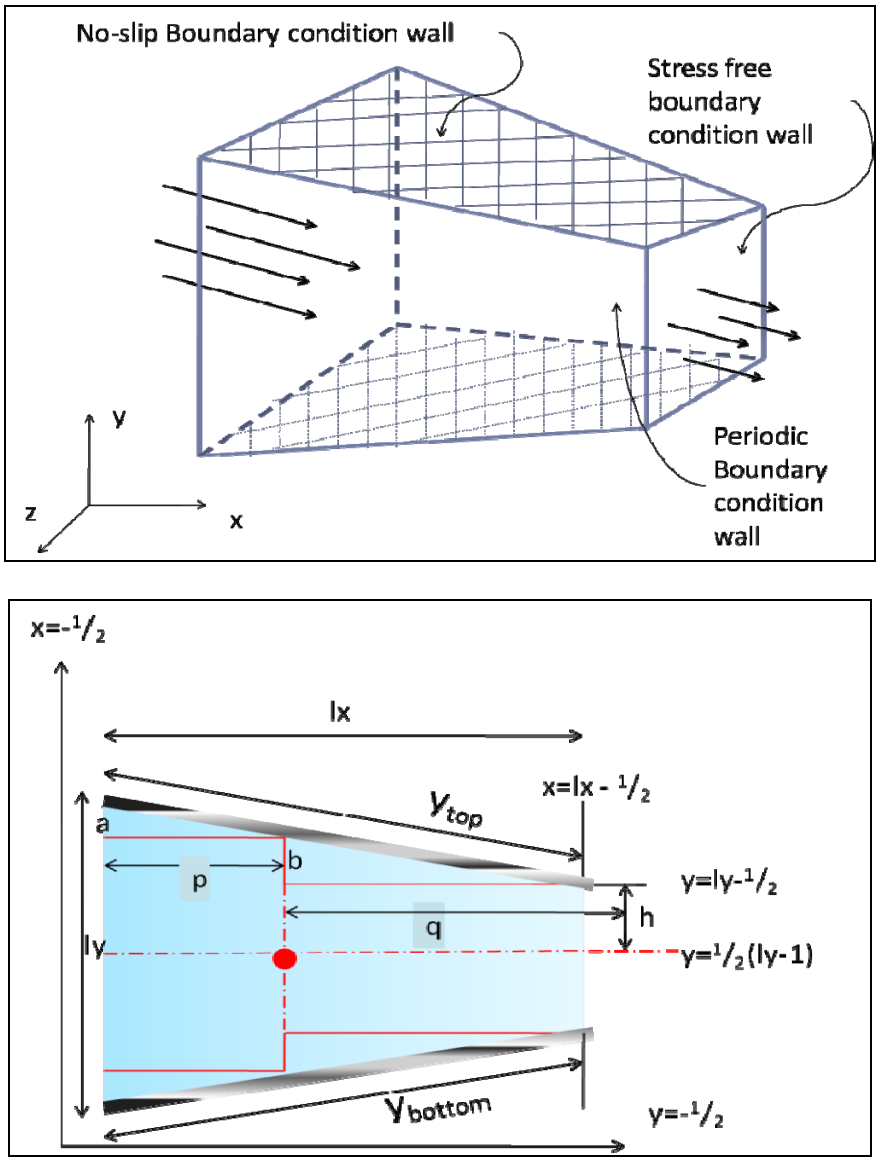

Figure 4.12: a) Schematic of diverging channel with boundary conditions applies for each wall direction (in three-dimensional view); b) Schematic of diverging channel in xy-plane for determining the top and bottom domain walls.

Modifying walls boundary conditions as illustrated in figures 12a and 12b is time consuming for the project; therefore, to simplify the domain simulation, the channel is adjusted as shown in figures 4.13a and 4.13b. The diverging channel is modeled as a rectangular channel with half cylinders on the top and bottom walls. The top and bottom

walls act as fixed walls with no-slip boundary conditions, while the other walls are periodic boundary conditions. The flow inlet is a uniform flow through the diverging channel.

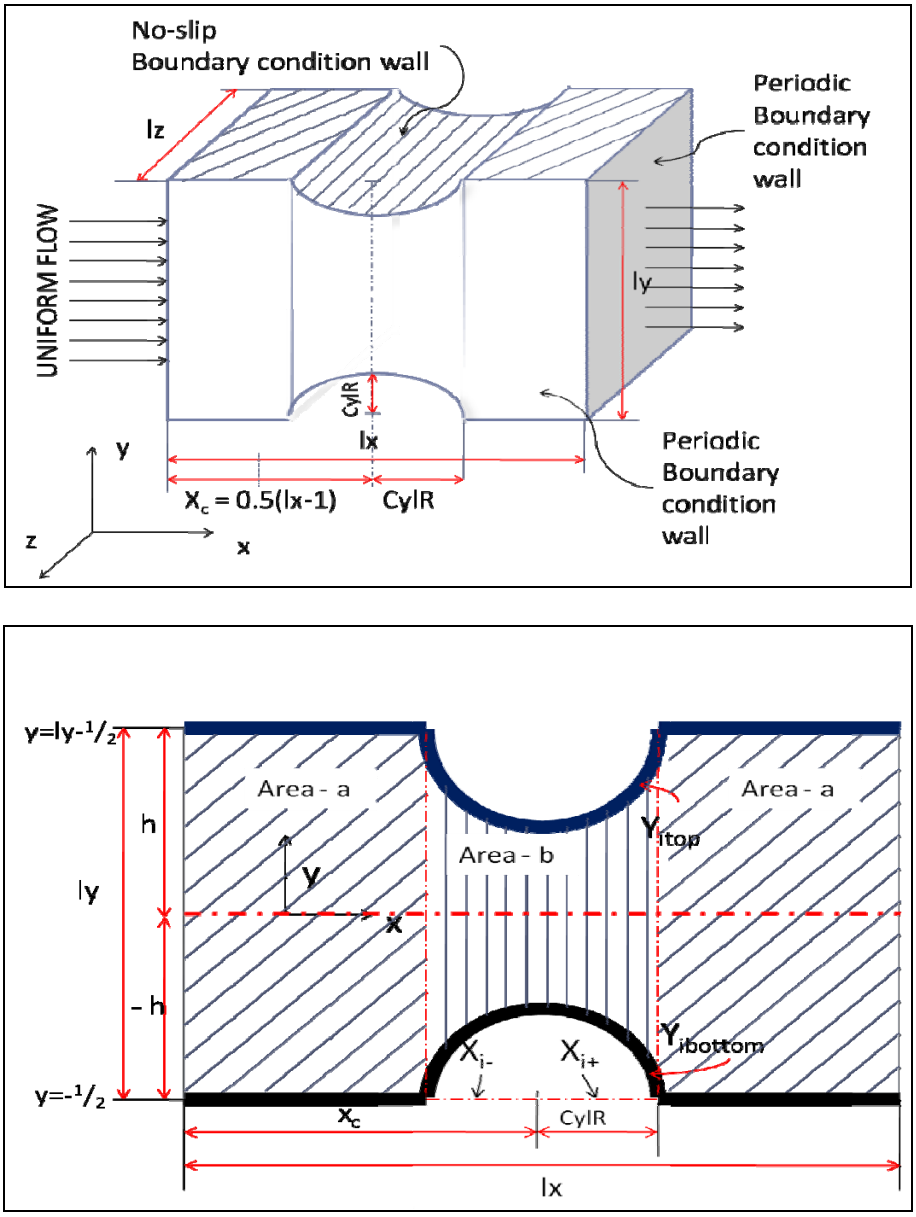

Figure 4.13: a) Schematic of simplified diverging channel with boundary conditions applied for each wall direction (in three-dimensional view); b) Schematic of simplified diverging channel in xy-plane for calculating the top and bottom domain walls.

Considering two different regions, the bounce-back walls are also treated in a different way. For flat region or area-a, the bounce back on the top and bottom walls are similar with the previous rectangular channel and for constricted region or area-b, the bounce back on the walls are adjusted to the curve wall. Figure 4.14 shows the fluid nodes (solid circle,) bounce back with collision (arrow line,) and streaming (blue strip arrow line,) phase occur through dummy nodes (empty circle,).

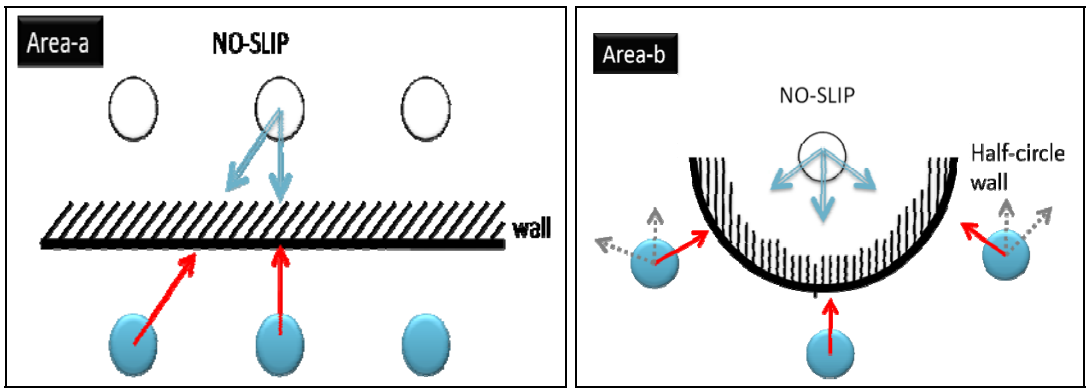

Figure 4.14: a) area-A: no slip boundary condition (apply to flat top and bottom domain walls) b) area-B: no slip boundary condition (apply to half-circle top and bottom domain walls)

For x direction and z direction, the periodic boundary conditions are applied. Figure 4.15 demonstrates the stage of collision (red arrow line,) and streaming (blue strip arrow line,) throughout the periodic boundary condition is performed. The lattice fluid node is denoted by an empty circle, , and the dummy node is denoted by the solid circle, .

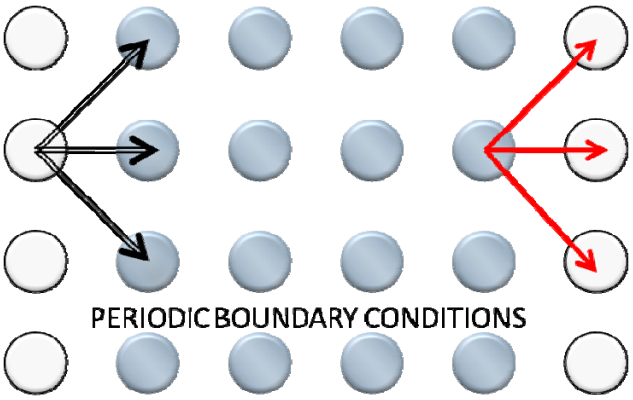

Figure 4.15: Periodic boundary conditions are apply to the x and z direction walls

The velocity distribution for uniform flow through rectangular channel is given

$$u(y) = \frac{1}{2\upsilon}\left(\frac{dp}{dx}\right)\left(h^2 - y^2\right), \tag{4.9}$$

where ν is the viscosity, $\left(\frac{dp}{dx}\right)$ is the pressure gradient, *h* is the height parameter calculated from the center of the domain to the top wall, and *u(y)* is the velocity profile in the y-direction.

The Reynolds number, Re is given by

$$\mathrm{Re} = \frac{u(y)D}{\upsilon}, \tag{4.10}$$

where D is the fiber diameter, ν is the viscosity (it is calculated from the lattice Boltzmann relaxation time, $\upsilon = \frac{2\tau - 1}{6}$. At the center y = 0, therefore

$u(y) = \frac{1}{2\upsilon}\left(\frac{dp}{dx}\right)\mathrm{h}^2$, and $\mathrm{h} = \frac{ly}{2}$, consequently the Reynolds number becomes

$$\mathrm{Re} = \frac{dp}{dx}\frac{ly^2 D}{8\upsilon}. \tag{4.11}$$

An example of fibers flowing through the simplified diverging channel can be seen in figure 4.18. Initially the fibers are located in random positions. Then after a number of time step, the fibers start to rotate and network among themselves, which demonstrates fiber-fiber interaction. Fibers with an aspect ratio of 9:1 are constructed with coarse and near rigid finite elements. The fiber diameter is 4.8 lattice units, fiber length is 43.2 lattice units, Reynolds number is 0.18, and volume fraction is 0.03. The results show the fiber-fiber interactions occur, and these interactions tend to create networks similar to flocculation in suspension flow. There is little detail to be reported for this case since it is a preliminary result for the simplified diverging channel; therefore, the simulation results are not verified to the experimental or theoretical results.

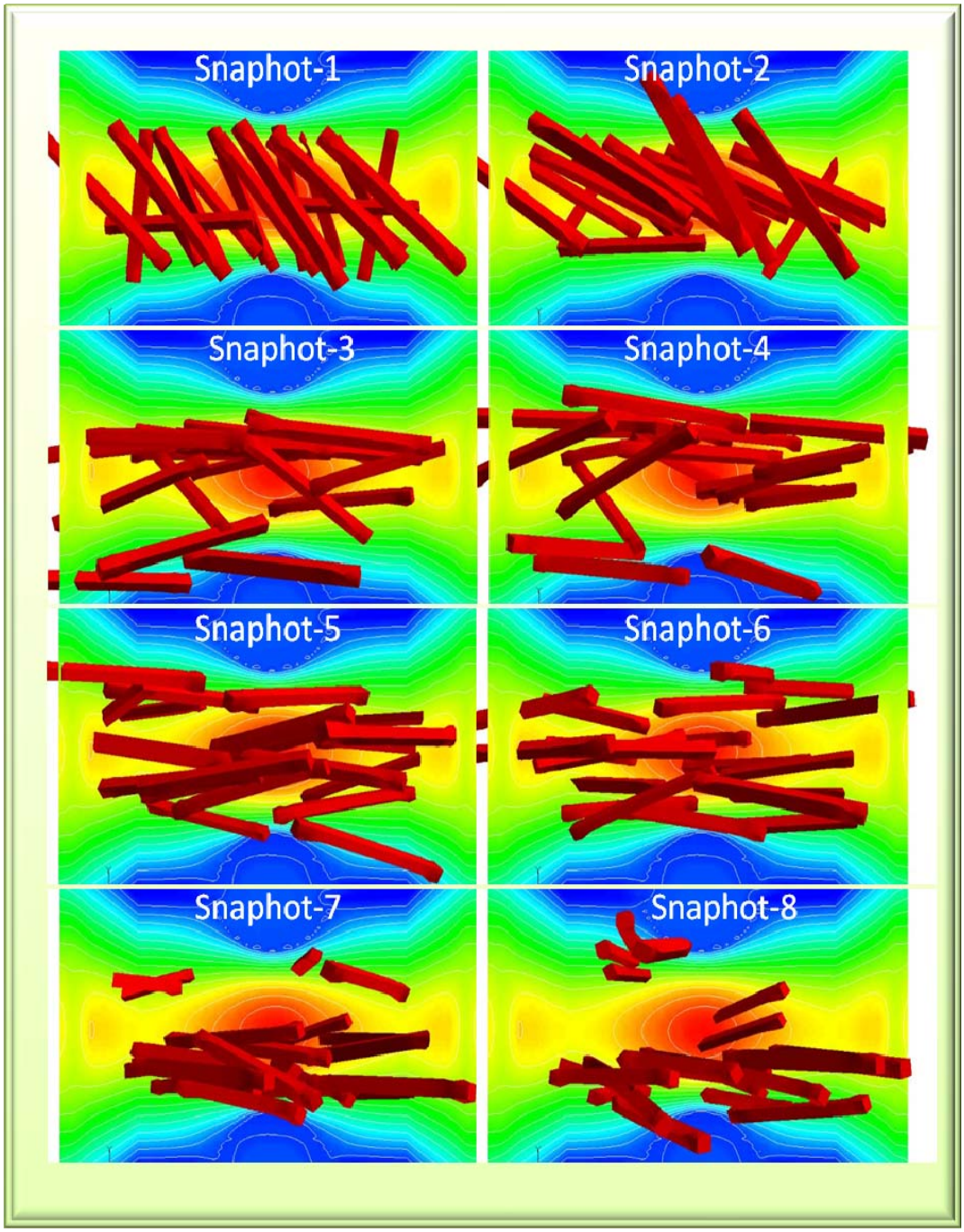

Figure 4.16: Snapshots of simulation results of 20 near rigid fibers through simplified diverging channel (uniform flow)

CHAPTER 5

CONCLUSION AND FUTURE STUDIES

A novel coupling method (combining the lattice Boltzmann and finite element methods) has been developed. This technique is applied to flexible fiber particle model to study the behavior of fibers in the papermaking process. Fibers are modeled as rod-like slender bodies comprised of linear-elastic solid finite elements. The applied continuum fiber model is more realistic for application in fiber suspensions compared to previous fiber models where the fibers are modeled as chain of rigid spheres or rod segments. In addition to that, it is a more realistic fiber model using a commercial finite element modeling software, where other models require some constraints to develop particle segments (i.e., connection rules between segments).

Hydrodynamic interactions in particle suspensions generally depend on shape, elastic properties and concentration. For spherical particle, the hydrodynamic interactions (i.e., lubrication forces) are sufficiently strong to prevent solid-body contacts (Aidun & Lu, 1998). In the case of slender fibers, it is observed that lubrication is not so strong to prevent actual physical contact between fibers (Sundararajakumar & Koch, 1997). The lubrication force resisting normal relative motion is related to the instantaneous minimum gap. Since the gap is much smaller than the surface roughness on the fibers, the actual physical contact must occur between the fibers. Therefore, this study neglects the short-range hydrodynamic interactions between fibers and takes into account the contact forces

only. The contact model comprised of the repulsive and attractive forces are considered in a general formulation to capture the surface charges on the fibers.

The lattice Boltzmann method is applied in this project, which is computationally efficient when compared to Navier-Stokes solvers. Moreover, the lattice Boltzmann method can be applied to fluid flows in complex geometries (Succi *et al.*, 1989).

The method developed in this project is a combination of the lattice Boltzmann and finite element methods. Finite element method is applied because it is a well-developed method and has been applied for numerous applications. The fibers are modeled using finite element method; therefore, the fibers can be deformed, and the behavior of the flexible fibers and near rigid fibers can be evaluated.

Two-dimensional work is presented (Rezak *et al*., 2005) for one particle in shear flow using a coupled static finite element and lattice Boltzmann method in Stokes flow. However, there is fluctuation of the particle surface nodes when the Young's modulus decreases, which is a limitation of this earlier work. In order to prevent this problem, damping factors are added to the dynamic finite element method in two- and three-dimensional cases. For three dimensional solid fibers, comparisons with Jeffery's orbit confirm the dilute-limit accuracy of this method.

Motion of a single fiber in shear flow is verified with Jeffery's theory by placing the fiber at the center between two parallel plates moving in opposite direction (Couette flow). The fiber is neutrally buoyant and Brownian motion is neglected. The simulation results of near rigid fibers with aspect ratios of 3:1 and 9:1 agree with Jeffery's theory with an error less than 2%. The end segment displacements are also obtained and compared to the rotation period between the simulation results and theoretical values.

Moreover, it is demonstrated that the fiber with lower stiffness deforms more during rotation. This shows that the period of a flexible fiber tends to decrease and rotate faster relative to a nearly rigid fiber. Forgac and Mason (1959) observe the deformation shape of rayon filaments in a simple shear flow. In this study, the deformation shape, such as the curved intermediate shape can be distinguished in higher aspect ratio flexible fiber rotation. The results show that the near rigid fibers rotate according to Jeffery's theory, and the flexible fibers show an increase in rotational velocity in agreement with numerical and experimental results.

The computational simulations in this project also cover dilute and semi-dilute fiber suspensions. The bulk properties of fiber suspensions for fiber aspect ratios 18:1 and 9:1 are obtained from the simulations. The results are then compared with data from experimental and theoretical studies (Blakeney, 1966; Einstein, 1926; Burger, 1938). The relative viscosities are measured for different concentrations and fiber flexibilities. The suspension relative viscosity agrees with Blakeney's experimental results. The flexible fibers produce higher relative viscosities than the near rigid fibers, which results from increasing fiber deformation and fiber-fiber interaction.

Future recommendations

The simulation cases presented in this project are performed in simple shear flow for comparison with experiments and theoretical analysis. The uniform flow with simple diverging channel is also presented as a more complex simulation domain. In conjunction with this work, extensions may be made to confirm the rheological behavior. A headbox or true diverging channel domain may be built to further study fiber suspensions in the papermaking process.

The versatile of finite element method can be extended to larger deformation by applying a non-linear dynamic response as the fiber model.

APPENDIX

CALCULATION WALLS DIVERGING CHANNEL

Calculation top and bottom wall for diverging channel (headbox)

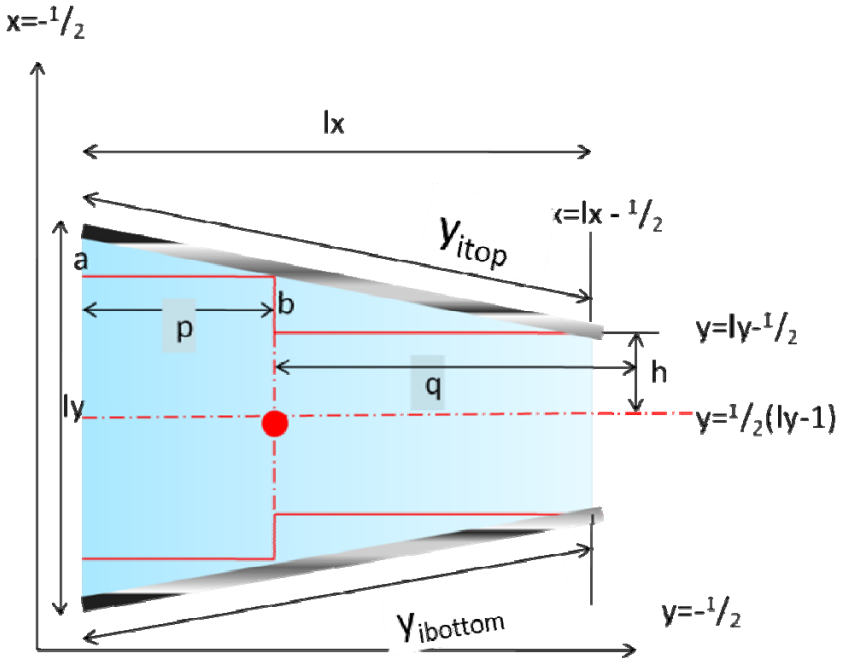

Figure A.1: Schematic diverging channel (headbox)

a, b, p, q = arbitrarily ratio parameters

y_{itop} = top wall diverging channel

$y_{ibottom}$ = bottom wall diverging channel

h = height parameter from centerline y = $^1/_2$ (ly – 1)

ly = height simulation domain

lx = length simulation domain

Top wall diverging channel

Domain ratio (see picture)

$$\frac{a}{b} = \frac{p}{q}$$

$$\frac{(ly - \tfrac{1}{2}) - y_{itop}}{y_{itop} - h - \tfrac{1}{2}(ly - 1)} = \frac{x_i + \tfrac{1}{2}}{(lx - \tfrac{1}{2}) - x_i}$$

$$((ly - \tfrac{1}{2}) - y_{itop})((lx - \tfrac{1}{2}) - x_i) = (y_{itop} - h - \tfrac{1}{2}(ly - 1))(x_i + \tfrac{1}{2})$$

$$(ly - \tfrac{1}{2})(lx - \tfrac{1}{2}) - y_{itop}(lx - \tfrac{1}{2}) - (ly - \tfrac{1}{2})x_i + y_{itop}\, x_i = (y_{itop} - (h + \tfrac{1}{2}(ly - 1)))(x_i + \tfrac{1}{2})$$

$$(ly - \tfrac{1}{2})(lx - \tfrac{1}{2}) - y_{itop}(lx - \tfrac{1}{2}) - (ly - \tfrac{1}{2})x_i + y_{itop}\, x_i = y_{itop}\, x_i - x_i(h + \tfrac{1}{2}(ly - 1)) - \tfrac{1}{2}(h + \tfrac{1}{2}(ly - 1)) + \tfrac{1}{2} y_{itop}$$

$$(ly - \tfrac{1}{2})(lx - \tfrac{1}{2}) - y_{itop}(lx - \tfrac{1}{2}) - (ly - \tfrac{1}{2})x_i = \tfrac{1}{2} y_{itop} - x_i(h + \tfrac{1}{2}(ly - 1)) - \tfrac{1}{2}(h + \tfrac{1}{2}(ly - 1))$$

$$\tfrac{1}{2} y_{itop} + (lx - \tfrac{1}{2}) y_{itop} = (ly - \tfrac{1}{2})(lx - \tfrac{1}{2}) - (ly - \tfrac{1}{2})x_i + x_i(h + \tfrac{1}{2}(ly - 1)) + \tfrac{1}{2}(h + \tfrac{1}{2}(ly - 1))$$

$$\boxed{y_{itop} = \frac{(ly - \tfrac{1}{2})(lx - \tfrac{1}{2}) - (ly - \tfrac{1}{2})\, x_i + (h + \tfrac{1}{2}(ly - 1)) + \tfrac{1}{2}(h + \tfrac{1}{2}(ly - 1))}{\tfrac{1}{2} + (lx - \tfrac{1}{2})}}$$

Bottom wall diverging channel

$$\frac{y_{ibottom} + \frac{1}{2}}{\frac{1}{2}(ly - 1) - h - y_{ibottom}} = \frac{x_i + \frac{1}{2}}{(lx - \frac{1}{2}) - x_i}$$

$$(y_{ibottom} + \frac{1}{2})((lx - \frac{1}{2}) - x_i) = (\frac{1}{2}(ly - 1) - (h + y_{ibottom}))(x_i + \frac{1}{2})$$

$$y_{ibottom}(lx - \frac{1}{2}) + \frac{1}{2}(lx - \frac{1}{2}) - \frac{1}{2}x_i - y_{ibottom}x_i =$$
$$\frac{1}{2}x_i(ly - 1) - x_i(h + y_{ibottom}) - \frac{1}{2}(h + y_{ibottom}) + \frac{1}{2}\frac{1}{2}(ly - 1)$$

$$y_{ibottom}(lx - \frac{1}{2}) + \frac{1}{2}(lx - \frac{1}{2}) - \frac{1}{2}x_i - y_{ibottom}x_i =$$
$$\frac{1}{2}x_i(ly - 1) - x_i h - y_{ibottom}x_i - \frac{1}{2}h - \frac{1}{2}y_{ibottom} + \frac{1}{4}(ly - 1)$$

$$y_{ibottom}(lx - \frac{1}{2}) + \frac{1}{2}(lx - \frac{1}{2}) - \frac{1}{2}x_i =$$
$$\frac{1}{2}x_i(ly - 1) - x_i h - \frac{1}{2}h - \frac{1}{2}y_{ibottom} + \frac{1}{4}(ly - 1)$$

$$y_{ibottom}((lx - \frac{1}{2}) + \frac{1}{2}) = \frac{1}{2}x_i(ly - 1) - x_i h - \frac{1}{2}h + \frac{1}{4}(ly - 1) +$$
$$\frac{1}{2}x_i - \frac{1}{2}(lx - \frac{1}{2})$$

$$\boxed{y_{ibottom} = \frac{(\frac{1}{2}(ly - 1) - h + \frac{1}{2})\ x_i - \frac{1}{2}h + \frac{1}{2}(\frac{1}{2}(ly - 1)) - \frac{1}{2}(lx - \frac{1}{2})}{\frac{1}{2} + (lx - \frac{1}{2})}}$$

REFERENCES

Aidun, C. K. & Lu, Y. (1995), Lattice Boltzmann Simulation of Solid Particles Suspended in Fluid, *Journal of Statistical Physics*, 81:49.

Aidun, C. K. & Lu, Y. (1995), A Method for Rheological Analysis of Suspension, *IPST Technical Paper Series Number 573*.

Aidun, C. K., Lu, Y., Ding, E-J. (1998), Direct Analysis of Particulate Suspensions with Inertia using the Discrete Boltzmann equation, *Journal of Fluid Mechanic*, 373: 287-311.

Aidun, C. K. & Qi, D. W. (1998), A New Method for Analysis of the Fluid Interaction with a Deformable Membrane, *Journal of Statistical Physics*, 90(1): 145-158.

Batchelor, G. K. (1970a), Slender-body Theory of Particles of Arbitrary Cross-section in Stokes Flow, *Journal of Fluid Mechanic*, 41:545-570.

Batchelor, G. K. (1970b), The Stress System in a Suspension of Force-Free Particles, *Journal of Fluid Mechanics*, 41: 545 – 570.

Batchelor, G. K. & Green, J. T. (1972), The determination of the Bulk Stress in a Suspension of Spherical Particles to order c^2", *Journal of Fluid Mechanics*, 56:401 – 427.

Bath, K-J. (1982), FINITE ELEMENT PROCEDURE IN ENGINEERING ANALYSIS, Prentice-Hall, Inc.

Bledzki, A. K., & Gassan, J. (1999), Composite Reinforced with Cellulose based Fibers, *Progress in Polymer Science*, 24:221 – 274.

Brady, J. F. & Bossis, G. (1988), Stokesian Dynamics, *Annual Review of Fluid Mechanics*, 20:111.

Bretherton, F. P. (1962), The motion of rigid particles in a shear flow at low Reynolds number*, Journal of Fluid Mechanics*, 14, 284 – 304.

Buxton, G. A, Verberg, R., Jasnow, D., Balazs, A. C. (2005), Newtonian Fluid meets an Elastic Solid: Coupling Lattice Boltzmann and Lattice-Spring Models, *Physical Review E*, 71:056707-1 – 056707-16.

Burger, J. M. (1938), On the motion of small particles elongated form suspended in a viscous liquid: 2nd report on viscosity and plasticity, North-Holland Publ., Amsterdam.

Blakeneley, W. R. (1966), The Viscosity of Straight, Rigid Rods, *Journal of Colloid and Interface Science*, 22, 324 – 330.

Claeys, I. L. & Brady, J. F. (1993a), Suspensions of Prolate Spheroids in Stokes flow. Part 1. Dynamics of a Finite Number of Particles in an Unbounded Fluid, *Journal of Fluid Mechanic*, 251:411 – 442.

Chen, H., Chen, S. & Matthaeus, W. H. (1992), Recovery of the Navier-Stokes equation using a Lattice-gas Boltzmann method, *Physical Review A*, 45:R5339.

Claeys, I. L. & Brady, J. F. (1993b), Suspensions of Prolate Spheroids in Stokes flow. Part 2. Statistically homogeneous Dispersions, *Journal of Fluid Mechanic*, 251:443 – 477.

Cox, R. G. (1971), The motion of long slender bodies in a viscous fluid, part 2 shear flow, *Journal of Fluid Mechanics*, 45, 625-657.

Ding, E-J. & Aidun, C. K. (2003), Extension of the Lattice Boltzmann Method for Direct Simulation of Suspended Particles Near Contact, *Journal of Statistical Physics*, 112(3/4):685 – 708.

Ding, E-J. & Aidun, C. K. (2004), A more Efficient Application of Lattice Boltzmann Method for Stokes Flow, *APS Presentation*.

Dewei Qi (2006), Direct Simulations of Flexible Cylindrical Fiber Suspensions in Finite Reynolds Number Flows, *The Journal of Chemical Physics* 125(11): 114901-1 – 114901-10.

Dewei Qi (2006), A new method for direct simulations of flexible filament suspensions in non-zero Reynolds number flow, *International Journal for Numerical methods in Fluids*.

Einstain, A. (1906) Eine neue Bestimmung der Molekuldimensionen, *Ann. Phys,* 19, 289 – 306.

Einstain, A (1936), A new determination of molecular dimensions, *In investigations on the theory of the Brownian Movement*, ed R. Furth, Dover, NewYork.

Eirich, F., Margaretha, H., Bunzul, M. (1936), *Kolloid-Z,* 75, 20.

Fan, X. J., Phan-Thien, N., Zheng, R. (1998), A direct simulation of fibre suspensions, *Journal of Non-Newtonian Fluid Mechanics*, 74: 113 – 135.

Feng, J. & Joseph, H. H. (1995), The unsteady motion of solid bodies in creeping flows, *Journal of Fluid Mechanic*, 303:83 – 102.

Forgacs, O. L. & Mason, S. G. (1959), Particle Motion in Sheared Suspension: X. Orbits of Flexible Threadlike Particles, *Journal of Colloid Science*, 14:473 – 491.

Forgacs, O. L. & Mason, S. G. (1959), Particle Motion in Sheared Suspension: XI. Spin and Deformation of Threadlike Particles, *Journal of Colloid Science*, 14:457 – 472.

Goto, S., Nagazono, Kato, H. (1986a), The flow behavior of fiber suspensions in Newtonian fluids and polymer solutions: I. mechanical Properties, *Rheology acta* 25:119.

Goto, S., Nagazono, Kato, H. (1986b), The flow behavior of fiber suspensions in Newtonian fluids and polymer solutions: I. Capillary flow, *Rheology acta* 25:246.

Hou, S., Zou, Q., Chen, S., Doolen, G., Cogley, A. C. (1995), Simulation of Cavity Flow by the Lattice Boltzmann Method, *Journal of Computational Physics*, 118: 329-347.

Jafari, A., Zamankhan, P., Mousavi, M. (2007), Computer simulation of flocs interactions: application in fiber suspension, *Colloid and surfaces: Physciochem. Eng.Aspects*, 292: 99-109.

Jeffery, G. B. (1922), The motion of ellipsoidal particles immersed in a viscous fluid, *Proc. R. Soc, Lond*, A 102: 161-179.

Joung, C. G., Phan-Thien, N., Fan, X. J. (2001), Direct Simulation of Flexible Fibers, *Journal of Non-Newtonian Fluid Mechanic*, 99:1 – 36.

Joung, C. G., Phan-Thien, N., Fan, X. J. (2002), Viscosity of curved fibers in suspension, *Journal of Non-Newtonian Fluid Mechanic*, 102:1 – 17.

He, X., Luo, L.-S. (1997), Theory of The Lattice Boltzmann: From the Boltzmann equation to The Lattice Boltzmann Equation, *Physical Review E*, 56(6):6811-6817.

Hu, H, Joseph, D., Crochet, M. J. (1992), Direct Simulation of Fluid Particle Motions, *Theoretical Computational Fluid Dynamics*, 3:285.

Kerekes, R. J., Soszynski, R. M. & TamDoo, P. A. (1985), The flocculation of the pulp fibers, In V, Punton, editor, Papermaking Raw Materials, Transacions of the Eight Fundamental Research Symposium Held at Oxford, 265 – 310, Mechanical Engineering Publications Limited.

Kerekes, R. & Schell, C. (1992), *Journal of Pulp and Paper Science*, 18(1):32.

Kerekes, R. J. (1995), Perspectives on Fibre Flocculation in Papermaking, *Preceedings of the International Paper Physics Conference*, 23:31.

Koch, D. L. (1995), A model for orientational diffusion in fiber suspension, *Phys Fluids*, 7:2086 – 2088.

Koch, D. L. & Shaqfeh, E. S. G. (1990), The average rotation rate of a fiber in the linear flow of a semidilute suspension, *Phys Fluids A*, 2:2093 – 2102.

Kitano, T., Kataoka, T., Shirota, T. (1981), An empirical equation of the relative viscosity of polymer melts filled with various inorganic fillers, *Rheology acta* 20:207.

Luo, L.-S.(1998), Unified Theory of Lattice Boltzmann Models for Non-ideal Gases, *Physical Review Letters*, 81(8):1618-1621.

Ladd, A. J. C. (1994a), Numerical Simulations of Particulate Suspensions via a Discretized Boltzmann Equation. Part 1. Theoretical Foundation, *Journal of Fluid Mechanic*, 271:285 – 309.

Ladd, A. J. C. (1994b), Numerical Simulations of Particulate Suspensions via a Discretized Boltzmann Equation. Part 2. Numerical Results, Journal *of Fluid Mechanic*, 271:311 - 339.

Ladd, A. J. C. & Verberg, R. (2001), Lattice Boltzmann Simulations of Particle-Fluid Suspensions, *Journal of Statistical Physics*, 104:1191 – 1251.

Lindstorm, L. B., & Uesaka, T. (2007), Simulation of The Motion of Flexible Fibers in Viscous flow, *Physics of Fluids*, 19:113307-1 – 113307-16.

Lindstorm, L. B., & Uesaka, T. (2008), Particle-level Simulation of Forming of The Fiber Network in Papermaking, *International Journal of Engineering Science.*

Lindstorm, L. B., & Uesaka, T. (2008), Simulation of Semidilute Suspensions of non-Brownian Fibers in shear flow, *The Journal of Chemical Physics,* 128:024901-1 – 024901-14.

Logan, D. L. (1986), A First Course in the Finite Element Method*,* PWS Publishing, Boston.

Luo, L.-S. (2000), Theory of the Lattice Boltzmann method: Lattice Boltzmann models for Non-ideal Gases, *Physical Review E*, 62(4):4982-4996.

Mackaplow & Shaqfeh (1996), A numerical study of the Rheological properties of suspensions of rigid, non-brownians fibers, *Journal of Fluid Mechanics*, 329: 155 – 186.

Mackaplow & Shaqfeh (1998), A numerical study of the sedimentation of fibre suspensions, *J. Fluid Mechanics* **376** (-), 149 – 182.

MacMeccan, R. & Clausen, J. (2006), Multiparticle Simulations of Deformable Red Blood Cells using Lattice Boltzmann Method, *APS Presentation*.

Mason S. G. (1950), The flocculation of pulp suspension and the formation of paper, *Tappi*, 33:440-444.

Mason, S. G. & Manley, R. S. J. (1957), Particle Motion in Sheared Suspensions: Orientations and Interactions of Rigid Rods, *Proc. Roy. Soc. London*, A238:117 – 131.

McNamara, G. R. & Zanetti, G. (1988), Use of the Boltzmann equation to Simulate Lattice-gas Automata, *J. Chem Phys,* 103:1852.

Mei, R., Shyy, W., Yu, D., Luo, L-S. (2000), Lattice Boltzmann Method for 3-D Flows with Curved Boundary, *Journal of Computational Physics*, 161:680 – 699.

Myers, W. T., (1962), The rheology of synthetic fiber suspension, Doctor's Disertation, The Institute of Paper Chemistry, Appleton, Wisonsin.

Nawab, M. A., Mason, S. G. (1958), *Journal of Phisical Chemistry*, 62:1248.

Parker, J. (1972), The Sheet-Forming Process, *TAPPI STAP*, 9.

Petrie, C. J. S. (1999), The Rheology of Fiber Suspension, *Journal of Non-Newtonian Fluid Mechanic*, 87:369 – 402.

Petrich, M. P., & Koch. D. L. (1998), Interaction between contacting fibers, *Physics of Fluids*, 10:2111 – 2113.

Petrich, M. P., Koch D. L., Cohen, C. (2000), An experimental determination of the Stress-microstructure Relationship in Semi-Concentrated Fiber Suspension, *Journal of Non-Newtonian Fluid Mechanic*, 95:101 – 103.

Phan-Tien, N. & Kim, S. (1994), Microstructure in elastic media: Principles and Computational methods, Oxford University Press, New York.

Rezak, S. & MacMeccan, R. (2005), Simulation of a Deformable Particle using Lattice Boltzmann Method, *APS Presentation*.

Rockey, K. C., Evans, H. R., Griffiths, D. W., Nethercot, D. A. (1975), The Finite Element Method, A Halsted Press Book, John Wiley & Sons, New York.

Rojiani, K. B. (1996), Programming in C with Numerical Methods for Engineers, Prentice Hall, New Jersey.

Ross, R. F. & Klingenberg, D. J. (1997), Dynamic Simulation of Flexible Fibers Composed of Linked Rigid Bodies, *J. Chem. Phys.*, 106(7): 2949-2960.

Schmid, C. F., Switzer, L. H., Klingenberg, D.J. (2000), Simulations of Fiber Flocculations: Effects of Fiber Properties and Interfiber Friction, *Journal of Rheology*, 44(4):781 – 809.

Shaqfeh, E. S. G. & Koch, D. L. (1988), The effect of of hydrodynamic interactions on the orientation of axisymmetric particles flowing through a fixed bed of spheres or fibers, *Phys. Fluids*, 31, 728.

Smook, G, 1992, Handbook for pulp and paper technologists, Angus Wilde Publications, Vancouver.

Skjetne, P., Ross, R. F., Klingenberg, D. J. (1997), Simulation of Single Fiber Dynamics, *J. Chem. Phys*, 107(6): 2108-2121.

Stockie, J. M. & Green, S. I. (1998), Simulating the Motion of Flexible Pulp Fibres Using the Immersed Boundary Method, *Journal of Computational Physics***,** 147: 147-165.

Stockie, J. M. (2002), Simulating the Dynamics of Flexible Wood Pulp Fibres in Suspension, *16th Annual International Symposium on High Performance Computing Systems and Applications*, p.154.

Succi, S., Foti, E., Higuera, F., "Three-dimensional flows in complex geometries with lattice Boltzmann method", *Europhysics Letters*, 10(5): 433-438, (1989).

Sundararajakumar, R. R. & Koch, D. L. (1997), Structure and Properties of Sheared Fiber Suspensions with Mechanical Contacts, *Journal of Non-newtonian Fluid Mechanic*, 73:205 – 239.

Switzer III, L. H. & Klingenberg, D. J. (2003), Rheology of Sheared Flexible Fiber Suspensions via Fiber-Level Simulations, *Journal of Rheology*, 47(3):759 – 778.

Thorp, B. A., Kocurek, M. J. (1998), Pulp and Paper Manufacture, *Vol.7 Paper Machine Operations*, Canadian Pulp and Paper Association, Canada.

Tornberg, A-K. & Shelley, M. J. (2004), Simulating the Dynamics and Interactions of Flexible Fibers in Stokes Flow, *Journal of Computational Physics*, 196:8 – 40.

Travelyan, B. J. & Mason, S. G. (1951), Particle Motion in Sheared Suspensions Part 1 rotations, *Journal of Colloidal Science*, 6:354 – 367.

Yammane, Y., Kaned, Y., Doi, M. (1995), The effect of interaction of rodlike particle in semi-dilute suspension under shear flow, *Journal of Phys Soc Jpn*, 64:3265 – 3274.

Yamamoto, S. & Matsuoka, T. (1993), A Method for Dynamic Simulation of Rigid and Flexible Fibres in a Flow Field, *J. Chem. Phys*, 98:644 – 650.

Yamamoto, S. & Matsuoka, T. (1994), Viscosity of Dilute Suspensions of Rod-like Particles, *J. Chem. Phys*, 100:3317 – 3324.

Yu, D., Mei, R., Luo, L-S., Shyy, W. (2003), Viscous Flow Computations with the Method of Lattice Boltzmann Equation, *Progress in Aerospace Science*, 39: 329 – 367.

Wolffe, G., Oleszkiewicz, J., Cherba, D., Qi, D. (2002), Parallelizing Solid Particles in Lattice Boltzmann Fluid Dynamics, *Int. Conf. on Parallel and Distributed Processing Techniques and Applications,* Las Vegas.

Zienkiewicz, O. C., Taylor, R. L. (2000), THE FINITE ELEMENT METHOD VOLUME 2: SOLID MECHANICS, Butterworth-Heinemann

VITA

SHEILA REZAK

Sheila Rezak was born on September 29, 1975 in Palembang, South Sumatra-Indonesia to Mohamad Rezak and Erly Erawati. She attended Sekolah Menengah Negeri (SMA) 1 in Palembang, received a Batchelor of Science in 1996 at the Sriwijaya University, Palembang. After graduating, she worked for Beloit Corp. as a Process Engineer in Mojokerto, East Java. Sheila has enthusiasm to have knowledge of papermaking process and furthermore she decided to study paper science engineering at Institute of Paper Science and Engineering at Georgia Institute of Technology and received a Master degree in 2002. Shortly after starting her doctoral studies at Georgia Institute of Technology, Sheila married Edison Manurung on January 3, 2003. The two delightfully welcomed their son Elijah Maximus Manurung into their family on May 15, 2005. In the Summer of 2008, she was awarded a Doctorate of Philosophy in Mechanical Engineering.